Search for the decays of stopped exotic long-lived particles produced in P-P collisions at 13 TeV at CMS

Dissertation

Presented in Partial Fulfillment of the Requirements for the Degree Doctor of Philosophy in the Graduate School of The Ohio State University

By

Weifeng Ji, M.S., B.S.

Graduate Program in Physics

The Ohio State University

2018

Dissertation Committee:

Professor Christopher Hill, Advisor

Professor Stanley Durkin

Professor Stuart Raby

Professor Douglass Schumacher

Abstract

In this dissertation, I present the searches looking for decays of stopped massive long-lived exotic particles, which are pair produced in the proton-proton collisions at 13 TeV and come to rest afterwards in the CMS detector at the CERN LHC. The decays are most likely to be observed when there are no collisions. Two specific decay scenarios are studied: a long-lived particle (LLP) decaying hadronically or semi-leptonically in the calorimeter, and a LLP decaying semi-leptonically or leptonically to a pair of muons in the muon detector. The calorimeter-based search is performed using 2.7 fb^{-1} of 13 TeV collision run data collected in 2015 and 35.9 fb^{-1} of 13 TeV collision run data collected in 2016, corresponding to a total trigger livetime of 721 hours. The muon search is performed using 2.8 fb^{-1} of 13 TeV collision run data collected in 2015 and 36.2 fb^{-1} of 13 TeV collision run data collected in 2016, corresponding to a total trigger livetime of 744 hours. Search results are interpreted in a couple of simplified models. The limits on the production cross sections and masses of LLPs are calculated as a function of particle lifetimes, which vary from 100 ns to 10 days, assuming the corresponding decaying branching fractions to be 100%. The results are the most stringent ones on the stopped LLPs so far.

This is dedicated to my parents and my wife.

Acknowledgments

First of all, I would like to express my sincere gratitude to my advisor Prof. Chris Hill for the continuous support of my Ph.D study and independent research. He guided me with patience, immense knowledge in the past four years time of research and writing of this thesis.

Besides my advisor, I would like to thank the rest of my thesis committee: Prof. Stan Durkin, Prof. Stuart Raby, and Prof. Douglass Schumacher, for their insightful comments, also for the past and upcoming hard questions which incented me to widen my research from various perspectives.

My sincere thanks also goes to my fellow labmates, Andrew Hart, and Bingxuan Liu, for their help in my study and research. Andrew's expertise on software development and physics analysis, Bing's passion for physics and sports, are all encouragement to me. I have also learned a lot from the two postdocs I worked with, Wells Wulsin and Juliette Alimena. Their expertise, responsiveness, and knowledge have a great impact on me. In particular, I am grateful to Marissa Rodenburg for enlightening me the first glance of research. Also I would like to thank Darren Puigh for proofreading and offering great comments on my candidacy paper. It is my honor to meet these friends at OSU.

I would also like to thank Stefanos Leontsinis, Felice Pantaleo, Mikhail Ignatenko and Jingyu Luo for the useful guidance and discussions to expand my knowledge when I'm based at CERN. I am grateful to my friend and college mate Zhaoxu Xi for accommodating me when I first arrived at CERN.

Last but not the least, I would like to thank my parents Gengfa Ji and Kouhua Qiu, as well as my wife Dan Gao for supporting me spiritually throughout writing this thesis and my life in general.

Vita

2013 . . . . B.S. Physics & Computer Science, Shanghai Jiao Tong University

2013-2015 . . . . Teaching Assistant, The Ohio State University

2015 . . . . M.S. Physics, The Ohio State University

2015-present . . . . Research Assistant, The Ohio State University

Publications

Research Publications

CMS Collaboration "Search for decays of stopped exotic long-lived particles produced in proton-proton collisions at $\sqrt{s} = 13$ TeV". *arXiv:1801.00359*

Fields of Study

Major Field: Physics

Table of Contents

Page

List of Tables

Table **Page**

List of Figures

Chapter 1: Introduction

Particle physicists ask themselves what are the properties of subatomic particles that constitute matter and radiation. Modern particle physics started with the discovery of electrons in 1897, and afterward many fundamental particles were discovered and their interactions were studied. Stable fundamental particles constituting matter include electrons, up quarks, and down quarks, which are all spin half fermions. Their heavier counterparts are short-lived fermions and can only be observed in radiation or collisions. These fermions interact with each other via the four fundamental interactions: gravitational, electromagnetic, strong, and weak interactions. Three (electromagnetic, strong and weak) out of the four interactions are known to be best described by a quantum field theory named the standard model (SM).

In the SM, electrons belong to the first generation of a spin-half fermion group called leptons, which consist of six different particles that are paired into three generations. The up quarks and down quarks, since they carry color charges and as their names suggest, belong to the first generation of another fermion group called quarks, which also consist of three generations of paired fermions. In both cases, particles in the second and third generations contain heavier partners with similar physical properties as those of their first generation counterparts. These particles are unstable and will decay to lighter fermions. Fermions interact with each other by exchanging mediating vector bosons. There is also one special type of neutral scalar particle in the SM, called Higgs boson, which gives mass to all fermions and vector bosons it interacts with.

Fundamental particles are searched for with high energy colliders, of which the most recent one is the Large Hadron Collider (LHC) at CERN where protons are accelerated to 6.5 TeV and then collide with each other in opposite directions in the detectors. There are two general purpose detectors at CERN, the Compact Muon Solenoid (CMS) and A Toroidal LHC ApparatuS (ATLAS), which record the final products of p-p collisions. All fundamental particles incorporated in the SM have been observed, with the most recent discovery being the observation of a scalar particle with a mass around 125 GeV in both CMS[1] and ATLAS[2] detector in 2012. The measurements of the scalar particle suggest that it is the Higgs boson of the SM.

The SM, although highly consistent with most precision measurements, has its limitations. The hierarchy problem is one of these. It derives from the huge difference between the weak scale (10^3 GeV) and the Plank scale (10^{19} GeV). Other limitations in the SM are the fact that there is no dark matter candidate and the fact that the three gauge coupling constants do not converge in the high energy regimes.

Supersymmetry[3] (SUSY) is one idea to cope with these problems. By assigning each SM particles a supersymmetric partners, the hierarchy problem could be solved because the radiative corrections of the Higgs mass due to SM particles and the SUSY particles cancel each other. Moreover, SUSY is able to unify the gauge coupling constants, and the lightest stable supersymmetric particle is a reasonable dark matter candidate. Split supersymmetry (split-SUSY)[4, 5, 6], which was first proposed in 2003, is a specific realization of SUSY that neglects the hierarchy problem but still preserves gauge coupling unification and has a dark matter candidate. Gluinos in split-SUSY could be long-lived and last for seconds before they decay, giving rise to special signatures in the detectors. The stopped particles searches, discussed in this dissertation, look for these special signatures to see if there is any evidence of beyond the standard model (BSM) particles.

The dissertation is organized as follows. In Chapter 2, I will talk about the theory of the SM and beyond as well as the motivation for the stopped particles search. Then the CMS detector will be introduced in Chapter 3. Finally Chapter 4 and Chapter 5 discuss the search for stopped particles with different final decay products in details.

Chapter 2: Theory

The standard model of particle physics (SM) is a physical theory describing the properties of all known fundamental particles and their non-gravitational interactions. It has successfully predicted the existence of the W and Z bosons, top quark, the tau neutrino, and the Higgs boson, and it is also consistent with nearly all precision measurements. However, the SM has its limitations and leaves some unresolved problems, including the hierarchy problem, no gauge coupling unification, and the missing dark matter candidate. These are the main motivation for the developments of various BSM theories. In this chapter, I will introduce the building blocks of the standard model, and then I will discuss what the SM naturalness problem is. After that, I will discuss SUSY, which is the most popular candidate to solve the naturalness problem. Finally, I discuss split-SUSY, a specific scenario in which the SUSY particles are long-lived.

2.1 The Standard Model

2.1.1 Particles and Their Interactions

Figure 2.1 and figure 2.2 give schematic views of the fundamental properties of particles in the SM, whose spins are either 0, $\frac{1}{2}$ or 1, as well as their interactions. Leptons and quarks are spin-$\frac{1}{2}$ fermions that fall into three generations. In each

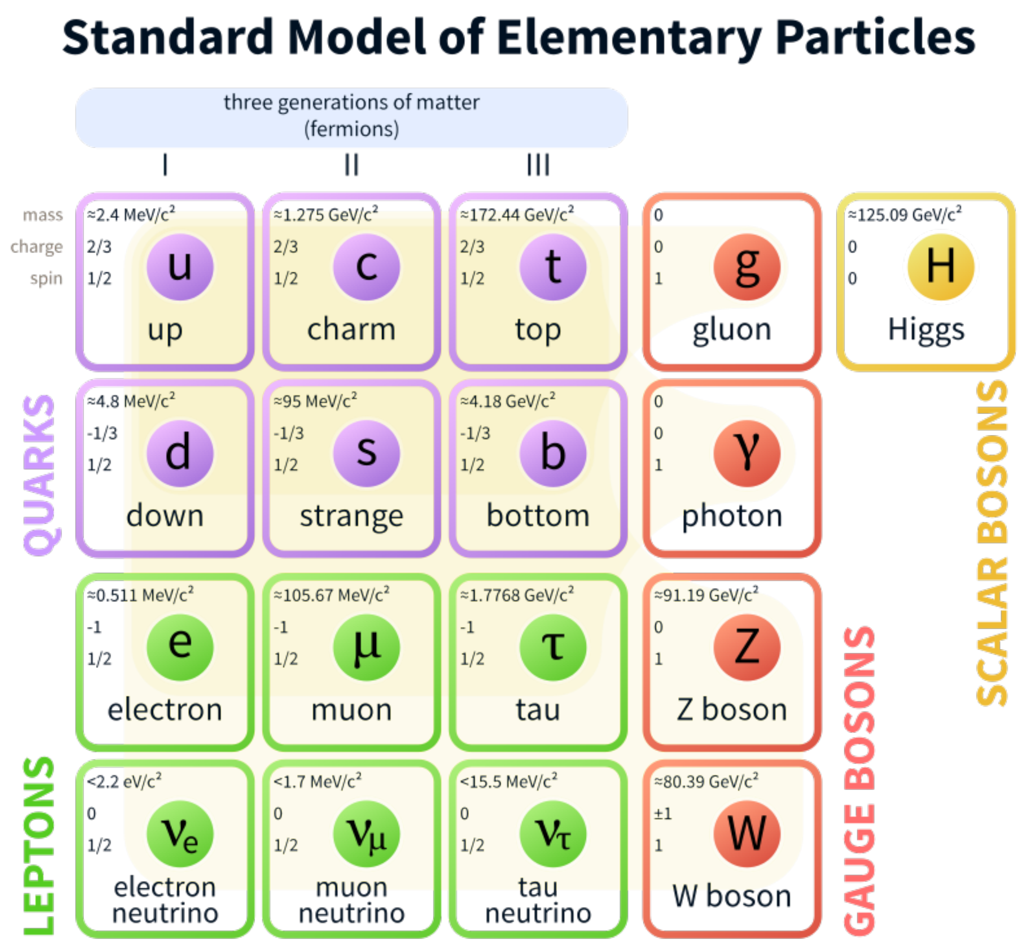

Figure 2.1: Particles in the Standard Model.

generation of leptons, there is a particle carrying electric charge -1 e, such as electron (e), and its corresponding electrically neutral neutrino, such as electron neutrino (ν_e). Quarks carry one more quantum number called color charge, which could be red, blue, or green. Each generation has a quark of electric charge $+\frac{2}{3}$ e, such as the up quark (u) and a quark of electric charge $-\frac{1}{3}$ e, such as the down quark (d). These fermions interact with each other via electromagnetic, weak, or strong interactions, which are mediated by the corresponding vector bosons. All fermions participate in the weak interaction, which is mediated by the weak vector bosons. All charged particles, including charged leptons, quarks, as well as W bosons, participate in the electromagnetic interaction, which is mediated by the photons. Moreover, strong interaction, which is mediated by gluons, involves all color-carrying particles, such as the quarks and the gluons. There is only one scalar boson in the SM, the Higgs boson, which gives rise to the massiveness of all particles it interacts with.

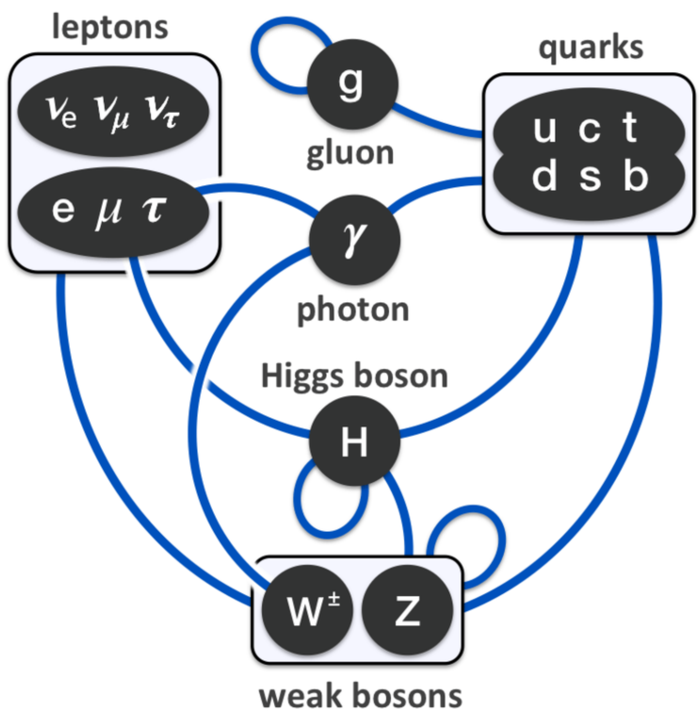

Figure 2.2: Particles in the SM and their interactions.

In the SM, the strong interaction is described by quantum chromodynamics (QCD), which involve color-carrying quarks and color and anticolor-carrying gluons. Since three colors exhibit an SU(3) symmetry, there are eight gluons in total, which correspond to eight generators, required by the local gauge invariance of SU(3). These eight gluons form a color octet and thus are all color charged. QCD assumes color confinement, which means no color charged particles can be isolated and travel freely, and that is why a free quark or gluon has never been observed. Color confinement also implies that the strong interaction is very short-ranged, since a massless but color-charged gluon cannot move as freely as a photon does, at it interacts electromagnetically. Another interesting feature of QCD is asymptotic freedom, which illustrates that the strong interaction is weak at high energy scales, thus making perturbative calculations viable. At low energy, the interaction becomes significantly higher, leading to, for example the confinement of quarks and gluons in the proton.

The theory of weak interactions was first proposed by Fermi in 1933 to explain beta decay via a four-fermion interaction. However, the cross section of a four-fermion interaction breaks unitarity as the center of mass energy increases. To deal with this, charged massive vector boson mediators were added to the theory to make the force non-contact and short ranged. In 1961, the electroweak theory was proposed by Glashow[7] to unify the weak and electromagnetic interactions. The theory requires the existence of charged and neutral weak vector bosons, which were later discovered at UA1[8] and UA2[9] in 1983. The electroweak gauge group of the SM assumes a symmetry of $SU(2)_I \times U(1)_Y$, where I corresponds to the weak isospin and Y corresponds to the weak hypercharge. There are three vector bosons (W1, W2, W3) corresponding to the generators of SU(2) and one vector boson (B) corresponding to the generator of U(1). However, local gauge invariance doesn't allow any mass terms of these gauge fields. Thus in order to incorporate the massiveness of the weak vector bosons, the $\mathrm{SU(2)_I \times U(1)_Y}$ symmetry must be spontaneously broken to $\mathrm{U(1)_Q}$, as the electric charge is still conserved after the symmetry breaking. As we will see, after the Higgs mechanism, which is the spontaneous symmetry breaking of a local gauge invariance followed by a gauge fixing procedure, the three mass eigenstates ($W^{\pm}, Z$) of the four electroweak vector bosons acquire masses, while the remaining one is massless, which corresponds to the photon.

2.1.2 The Spontaneous Symmetry Breaking and the Higgs Mechanism

Spontaneous symmetry breaking breaks the symmetry of the ground state but keeps the symmetry of the Lagrangian intact. This could be illustrated via an example of the spontaneous symmetry breaking of the global U(1) symmetry. Consider the Lagrangian for a theory of a complex scalar field:

$$\mathcal{L} = (\partial_\mu \phi)^\dagger (\partial^\mu \phi) - V(\phi^\dagger \phi), V(\phi^\dagger \phi) = \mu^2 \phi^\dagger \phi + \frac{\lambda}{2}(\phi^\dagger \phi)^2 \tag{2.1}$$

The parameter λ needs to be non-negative so that the potential has a lower bound. If μ^2 is non-negative as well, the potential has a bowl shape with a global minimum at the center. And the vacuum expectation value (VEV) $< \phi >$ of the field, corresponding to the point where V is at its minimum, is 0. When μ^2 is negative, the potential becomes a 'Mexican hat' shape, as shown in Fig. 2.3. In this case, the potential has an infinite number of global minima that could be the ground state of the system, corresponding to points along the circle $\phi = ve^{i\theta}$, where v is $\frac{\mu^2}{\lambda}$. The Lagrangian still has a rotational symmetry, yet the ground states are not symmetric anymore. The ground state of the system then corresponds to a random state of VEV $\frac{\mu^2}{\lambda}$ on the circle. Whatever the ground state is, we can shift the field corresponding to the radial degree of freedom so that new fields are expanded around the ground state to make perturbative calculations viable. The field redefinition generates a positive mass term for the field of the radial degree of freedom, making it massive. At the same time, the field of the tangential degree of freedom is massless, and it corresponds to the Goldstone boson.

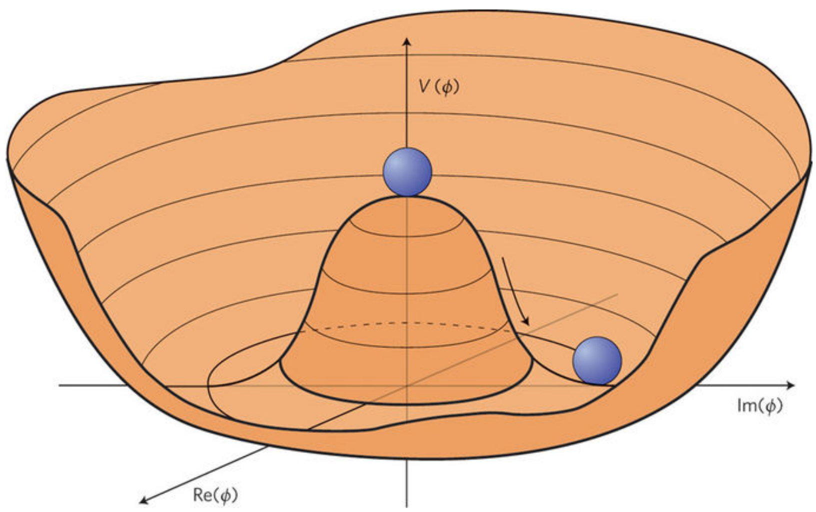

Figure 2.3: Higgs potential.

We now promote the global U(1) symmetry to a local U(1) symmetry by introducing a massless gauge field to the theory. If we follow the steps we have done just before, the gauge field would acquire a mass term thus becoming massive, and at the same time, we will also have one massive scalar boson and one undesirable massless Goldstone boson. However, we also have in the Lagrangian a bilinear term that consists of two different fields, which implies that fundamental particles are not identified correctly. By appropriately fixing the gauge, we can eliminate the unphysical bilinear term, and at the same time, the undesirable massless Goldstone field also disappears miraculously. As a result, the degree of freedom corresponding to the Goldstone boson has been incorporated into the massless gauge field, making the latter one massive. This whole process is referred to as the Higgs mechanism[10, 11, 12].

In the SM, the Higgs field can be written as two complex scalar fields, $\mathrm{H} = (\phi^+, \phi^0)$. Applying the Higgs mechanism to the spontaneous symmetry breaking of local gauge invariance of $\mathrm{SU}(2)_\mathrm{I} \times \mathrm{U}(1)_\mathrm{Y}$, three out of four degrees of freedom of the Higgs field will be incorporated into the SM weak vector bosons, making them massive. The remaining one degree of freedom, which has nonzero VEV, is the SM Higgs boson. The fermions in the SM acquire masses via their interactions with the Higgs boson through Yukawa couplings. On 4th July 2012, a scalar particle with a mass around 125 GeV was observed in both the CMS[1] and the ATLAS[2] detector at the CERN LHC, and its properties agree with those of the Higgs boson.

2.2 Beyond the Standard Model

2.2.1 Hierarchy Problem of the Higgs Mass

One of the problems in the SM is the hierarchy problem, which asks why there's a huge difference between the observed Higgs mass and its enormous radiative corrections to the bare mass in the quantum field theory.

In the SM, the mass corrections to a scalar particle are quadratically divergent. The main contributions in the radiative component corresponding to the Higgs mass come from the top quark, the weak gauge bosons, and the Higgs self-interactions, as shown in Fig. 2.4.

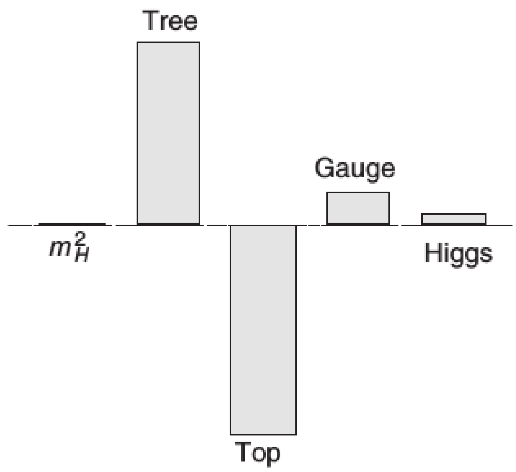

Figure 2.4: Illustration of fine-tuning, in which large corrections end up with a small Higgs mass.

$$m_h^2 = m_{tree}^2 - \frac{3}{8\pi^2} y_t^2 \Lambda_{UV}^2 + \frac{1}{16\pi^2} g^2 \Lambda_{UV}^2 + \frac{1}{16\pi^2} \lambda^2 \Lambda_{UV}^2 \tag{2.2}$$

If we assume the cutoff energy Λ_{UV} to be the Plank scale (10^{19} GeV), then nature needs to be extremely fine-tuned to cancel quantities at the order of 10^{34} GeV so that the physics mass of the Higgs boson remains at around 125 GeV. This cancellation seems unnatural and unlikely.

This quadratic divergence doesn't exist in the case of fermions and vector bosons, as their masses are protected by chiral symmetry and gauge invariance.

One can argue that the hierarchy problem is not even a problem by invoking the anthropic principle, which states that we must observe a universe that is consistent with our existence.

Nevertheless, efforts have been made to save the theory from unnaturalness. From the equation 2.2, there are basically two ways to make the cancellation natural. The first way is to decrease the cutoff energy. For example, Large Extra Dimension[13, 14], a theory in which the gravity becomes non-negligible at a much larger length scale, favors this idea.

The second idea is to introduce new terms to the quantum corrections. SUSY[15, 16] is a leading candidate among these solutions, which we will introduce in the next section.

2.2.2 Supersymmetry

SUSY introduces a systematic way to cancel the tremendous contributions to the mass corrections of the Higgs boson by assigning each fermion in the SM supersymmetric bosonic partners, and similarly assigning to each boson in the SM a supersymmetric fermionic partner.

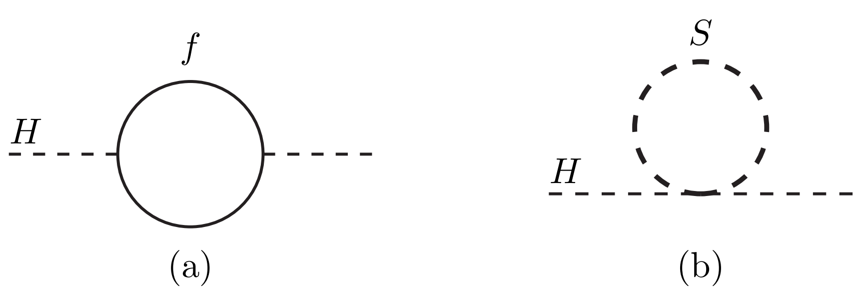

Figure 2.5: One loop diagram of higgs mass corrections due to (a) a Dirac fermion, (b) a scalar.

Then, ideally, the radiative corrections from the SM model particles will be canceled out by their supersymmetric partners. For example, the quantum correction term of the Higgs mass due to a fermion in the SM, as shown in the left plot of Fig. 2.5, is:

$$\Delta m_h^2 = -\frac{|\lambda_f|^2}{8\pi^2}\Lambda_{UV}^2 + ... \tag{2.3}$$

If we introduce a supersymmetric scalar particle to the fermion we discussed above, it will yield a quantum correction term, as shown in the right plot of Fig. 2.5:

$$\Delta m_h^2 = -\frac{\lambda_s}{16\pi^2}\Lambda_{UV}^2 + ... \tag{2.4}$$

If each fermion in the SM has two corresponding supersymmetric complex scalars, and the relation $\lambda_s = y_f^2$ holds, then the quadratic term in the quantum corrections will be canceled out. The remaining terms are only logarithmic, thus they are far less sensitive to the high energy scale. If SUSY is an exact symmetry, SUSY particles will have the same mass as their SM partners, and the cancellation would extend to all orders of the perturbations. However, due to the fact that we haven't observed any SUSY particles so far, SUSY must be a broken symmetry where SUSY particles are heavier than their SM partners.

Even though the exact symmetry is broken, the natural cancellation is still possible as long as the mass splitting between SM particles and their SUSY partners is not too large. Usually, the lightest superparticles are expected to have a mass not much greater than 1 TeV. This makes the LHC an ideal place to hunt for SUSY, as protons currently collide with each other at a center of mass energy of 13 TeV.

The nomenclature of bosons in SUSY is to add an "s" at the beginning of names of their SM fermionic counterparts, like stop ($\tilde{t}$) or stau ($\tilde{\tau}$). In case of SUSY fermions, we add “ino” to the end of the name of the corresponding SM bosons, like gluinos ($\tilde{g}$), winos ($\tilde{W}^+, \tilde{W}^0, \tilde{W}^-$), bino ($\tilde{B}^0$) and higgsinos ($\tilde{H}$). These gauginos and higgsinos mix with each other and form mass eigenstates that are charginos ($\tilde{\chi}^{\pm}$, which are electrically charged) or neutralinos ($\tilde{\chi}^0$, which are electrically neutral). Neutralinos are potential dark matter candidate, as long as they are the lightest SUSY particles and R-parity is conserved, which means that SUSY particles cannot decay only to SM particles.

2.2.3 Split-supersymmetry

Split-SUSY[4, 5, 6] is a supersymmetric theory that does not require naturalness, but still provides the gauge coupling unification and has a dark matter candidate. This theory features a large mass splitting between gauginos and supersymmetric scalars, and the mass of gauginos could be $\sim$ TeV due to chiral symmetry. One important phenomenology of split-SUSY is that the lifetime of the gluino can be very long-lived since it can only decay via a virtual squark whose on-shell mass is much heavier. The decay rate of gluino can be roughly estimated as $\frac{m_g^5}{m_{sq}^4}$, where m_g is the gluino rest mass and m_{sq} the squark rest mass. In the split-SUSY theory, the lifetime of the gluino is restricted to be less than 100 s since the supersymmetry breaking scale above 10^9 GeV will incur the violation of Big Bang Neucleosynthesis[17], altering the abundance of D and Li^6.

The gluino will form an R-hadron if it doesn’t decay promptly, and the R-hadron can leave the detector without leaving too much energy if the lifetime of the gluino is larger than tens of nanoseconds. These long-lived massive R-hadrons, if charged, have the signatures of long time-of-flight (TOF) and high energy loss (dE/dx). These properties have been searched for by both ATLAS[18] and CMS[19]. Another interesting scenario is that if the initial kinetic energy of the R-hadron is sufficiently low, it is possible for it to lose all of its kinetic energy and come to rest[20] in the detector via electromagnetic and nuclear interactions. The detection of the decay of these stopped particles would provide us with a direct observation of massive long-lived particles and a unique chance of measuring their lifetime.

2.3 Long-lived particles in the Standard Model and beyond

Since the stopped particle searches are looking for BSM particles with long lifetimes, it is good to understand what makes a particle long-lived. Both SM and BSM theories predict particles with long lifetime. There are a couple of mechanisms that could make a particle long-lived, such as conserved quantum numbers, squeezed phase space, virtual intermediate particles with massive on-shell mass, as well as interactions with small coupling constant.

In SM, the baryon number (B), lepton number (L_e, L_μ and L_τ) and charge (Q) are conserved. Thus protons and electrons are stable particles, since the proton is the lightest baryon and the electron is the lightest charged particle. In some SUSY models, R-parity is assumed to be conserved to avoid the fast decay of protons, whose lifetime is observed to be between 10^{33} and 10^{34} years. In this case, the lightest supersymmetric particle (LSP) is stable because the only kinematically feasible decay is decaying to SM particles, which is forbidden by the conservation of R-parity.

The neutrons and muons are long-lived in the Standard Model because their decays involve weak interactions and the phase space of the decays are suppressed due to the small mass difference between initial and final decay products. This can also be realized in BSM theories, such as Anomaly Mediated Supersymmetry Breaking (AMSB), which predicts a spectrum in which the mass splitting between the lightest chargino and the lightest neutralino is very small, typically between 140-200 MeV. This makes the lightest chargino long-lived.

Without assuming the conservation of R-parity, as we do in many SUSY scenarios, gauge invariance does allow some extra terms in the super potential:

$$W_{RPV} = \mu_i H_u L_i + \frac{1}{2}\lambda_{ijk} L_i L_j E_k^c + \lambda_{ijk}^{'} L_i Q_j D_k^c + \frac{1}{2}\lambda_{ijk}^{"} U_i^c D_j^c D_k^c \tag{2.5}$$

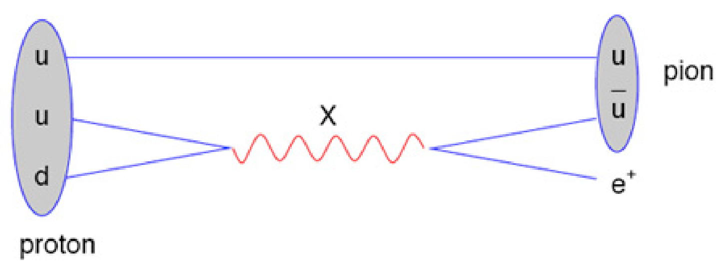

Figure 2.6: The Feynman diagram of the proton decay, which include both baryon number violating interaction and lepton number violating interaction. The decay can be suppressed if we require at least one of the coupling to be zero.

where the interaction corresponding to coupling $\lambda^{"}$ violates baryon number conservation and the interactions corresponding to coupling λ and $\lambda^{'}$ violate the lepton number conservation. In this case, the proton decay can also be suppressed if either lepton number or baryon number is conserved. The LSP will decay very slowly if the coupling is sufficiently small. For example, in the lepton number violating R-parity violating supersymmetry (RPV SUSY), it's possible to have an LSP stop that decays to a bottom quark and a lepton: $\tilde{t} \rightarrow bl$.

Moreover, in the gauge-mediated supersymmetry breaking (GMSB) scenario, the strength of the coupling of the gravitino with matter is proportional to F^{-1}, where F is the scale of the SUSY breaking. Then depending on the value of F, the decay length of the particle could be several hundreds of micrometers to meters. For example, a Bino-like neutralino will decay to a photon and a gravitino with a decay length of[21]:

$$c\tau \sim 130(\frac{100\ \mathrm{GeV}}{\tilde{m}})^5(\frac{\sqrt{F}}{100\ \mathrm{TeV}})^4\ \mu m \tag{2.6}$$

where $\tilde{m}$ is the mass of the neutralino.

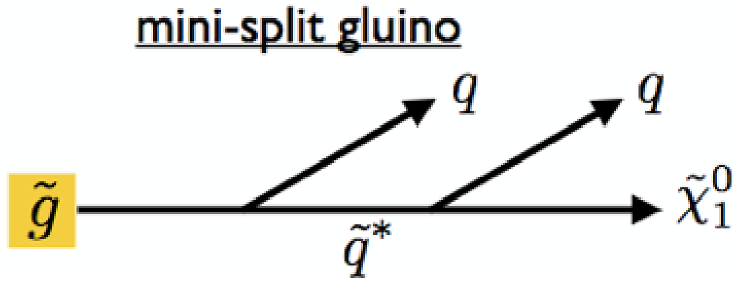

Figure 2.7: The Feynman diagram of the gluino decay in the split-SUSY.

In SM, although the weak coupling constant is stronger than that of the electromagnetic coupling constant, the cross section of the weak interaction is generally smaller than that of the electromagnetic interaction, due to the massiveness of the intermediate vector bosons. In split-SUSY, where the gluino decays to a quark, an anti-quark and a neutralino via a virtual squark with huge on-shell mass, as shown in Figure 2.7. Then the lifetime of the gluino can be written as:

$$c\tau \sim 10^{-5}m(\frac{m_{\tilde{q}}}{\mathrm{PeV}})^4(\frac{\mathrm{TeV}}{m_{\tilde{g}}})^5 \tag{2.7}$$

$m_{\tilde{g}}$ and $m_{\tilde{q}}$ represent the mass of the gluino and the squark.

Chapter 3: LHC and CMS Detector

3.1 The Large Hadron Collider

The Large Hadron Collider (LHC), the largest particle collider in the world, was built by CERN between 1998 and 2008. It is a superconducting circular particle collider located in a tunnel with a circumference of 27 km, which is 175 meters beneath the border between France and Switzerland near Geneva. Both the clockwise beam and the counterclockwise beam of particles are accelerated to almost the speed of light within the collider and collide with each other at the crossing points at a center of mass energy of 13 TeV, helping scientists probe the energy frontier at TeV scale.

The LHC mainly operates in proton-proton (pp) mode, although it sometimes also operates in proton-lead ($p-Pb$), lead-lead (Pb-Pb), or xenon-xenon (Xe-Xe) mode for relativistic heavy-ion physics. Before the particle beams are finally injected into the LHC, a series of injection and acceleration stages is performed to maintain focused and stable bunches. A few previous colliders built at CERN are used to achieve this goal. Figure 3.1 shows the full complex for the beam injection and acceleration. Protons are produced from hydrogen gas. The beam of bare protons is then accelerated up to 750 keV in the Radio-Frequency Quadrapole (RFQ). Then the protons are accelerated up to 50 MeV by the linear collider LINAC2. Protons are then injected into the Proton

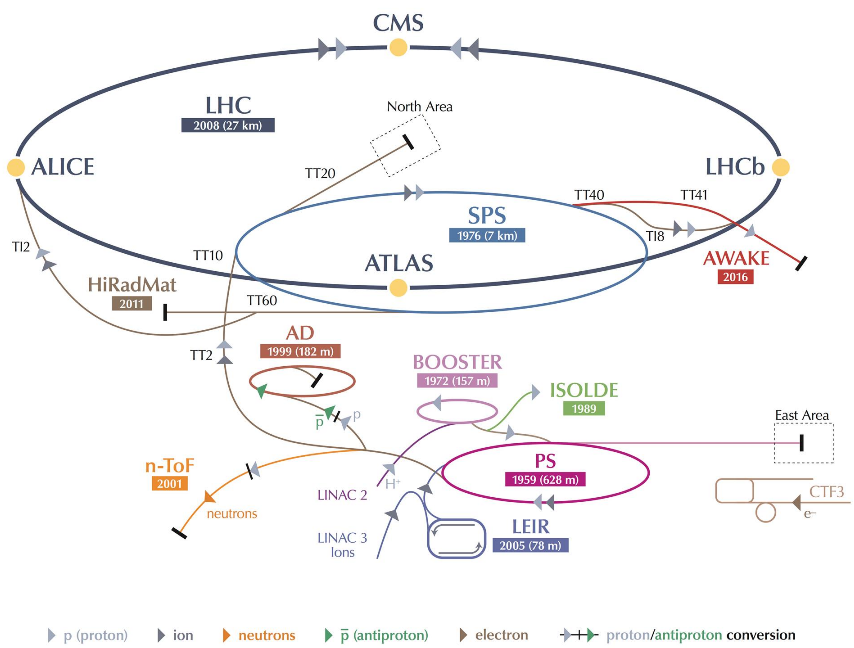

Figure 3.1: The schematic layout of the accelerator complex at CERN.

Synchrotron Booster (PSB), in which four superimposed rings accelerate the protons further to 1.4 GeV. They are then transported into the Proton Synchrotron (PS), in which the energy of protons reaches 25 GeV. Proton bunches also form trains where each bunch of approximately 1.15×10^{11} protons are separated by 25 ns. Three or four bunch trains are then injected into the Super Proton Synchrotron (SPS), which accelerates the protons to 450 GeV and then injects them into both rings of the LHC. Finally, the protons are accelerated up to the maximum speed by 16 radio-frequency (RF) cavities. In Run II (2015 and 2016), the proton beams are accelerated to 6.5 TeV in each ring of the LHC so that the protons traveling at opposite directions collide with each other at collision points at a center of mass energy of 13 TeV.

There are four crossing points around the LHC rings, as shown in Fig. 3.1, and each of them is instrumented with a major experiment. Two general-purpose experiments, ATLAS and CMS, are designed to target a broad spectrum of physics with a high integrated luminosity of proton-proton collisions. A third experiment, LHCb (The Large Hadron Collider Beauty Experiment), performs precision studies of b physics by collecting a relatively lower luminosity. A fourth experiment, ALICE (A Large Ion Collider Experiment), detects heavy-ion collisions to study the phenomenology of the physics of strongly interacting matter.

3.1.1 Luminosity

The cross section quantifies the likelihood of an interaction between two initial particles that produce specific final products. The cross sections of the new physics that are searched for at the LHC are usually very small. The interaction rate and the total number of interactions are then given by:

$$\frac{dN}{dt} = \sigma \times \mathcal{L} \quad N = \sigma \times \int \mathcal{L} dt = \sigma \times L \tag{3.1}$$

where σ is the cross section, $\mathcal{L}$ is the instantaneous luminosity, which is a measurement of the pp flux at each bunch crossing and is an important characterization of the performance of the LHC, and L is the accumulated luminosity over time, which is proportional to the number of signal events that can be observed by the searches. Assuming that the beam spatial distribution is Gaussian, the instantaneous luminosity can be expressed as:

$$\mathcal{L} = \frac{N_b^2 n_b f_{rev} \gamma_r}{4\pi \epsilon_n \beta^*} F \tag{3.2}$$

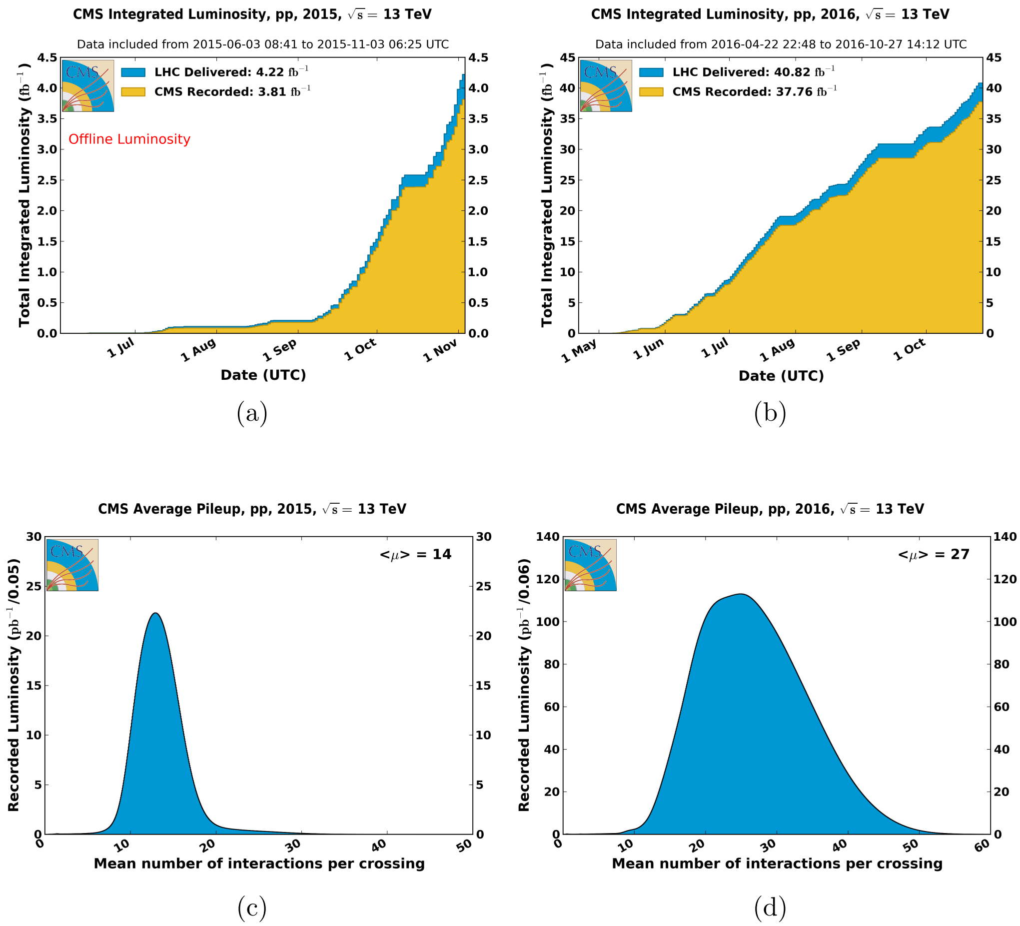

Figure 3.2: (a) Average number of interactions per bunch crossing in the CMS detector in 2015; (b) same as (a) but for 2016; (c) the integrated luminosity delivered by LHC and recorded by CMS in 2015; (d) same as (c) but for 2016.

where N_b is the number of particles per bunch, n_b is the number of bunches per beam, and β^* is a factor that is related to the horizontal and vertical beam size at the interaction point. The integrated luminosity is proportional to the amount of data collected by the detector and is often reported in units of fb^{-1}, as shown in Fig. 3.2. There is another important quantity related to the beam interaction, which is the average number of inelastic pp interactions per bunch crossing. This quantity is often referred to as the pile-up parameter (μ). The high instantaneous luminosity directly leads to a higher frequency of proton-proton interactions at each bunch crossing, which is known as in-time pile-up. Moreover, the high frequency of proton bunches (up to 40 MHz) and the unavoidable hardware latency in the detector causes further out-of-time pile-up situations. The pile-up events are not correlated with the elastic (hard) scattering process, and can be approximated as a background of soft energy deposits that can be taken care of in the jet reconstruction.

3.1.2 LHC Filling Schemes

The LHC beam consists of proton bunches, which contain 10^{11} protons each, has an interaction region with a longitudinal length of 30 cm, transverse dimensions of the order of a mm. In the 2015 and 2016 data taking periods, proton bunches are spaced by integer multiples of a 25 ns time interval. That means, in a complete LHC orbit (89 μs), there should be 3564 bunch positions that are either empty or filled with a proton bunch when the beam is first formed[22]. These nominal 25 ns intervals are defined as BX in the stopped particles search.

A filling scheme defines how these 3564 BXs are filled with proton bunches. An example is given in Fig. 3.3. The filling scheme remains the same during one LHC fill,

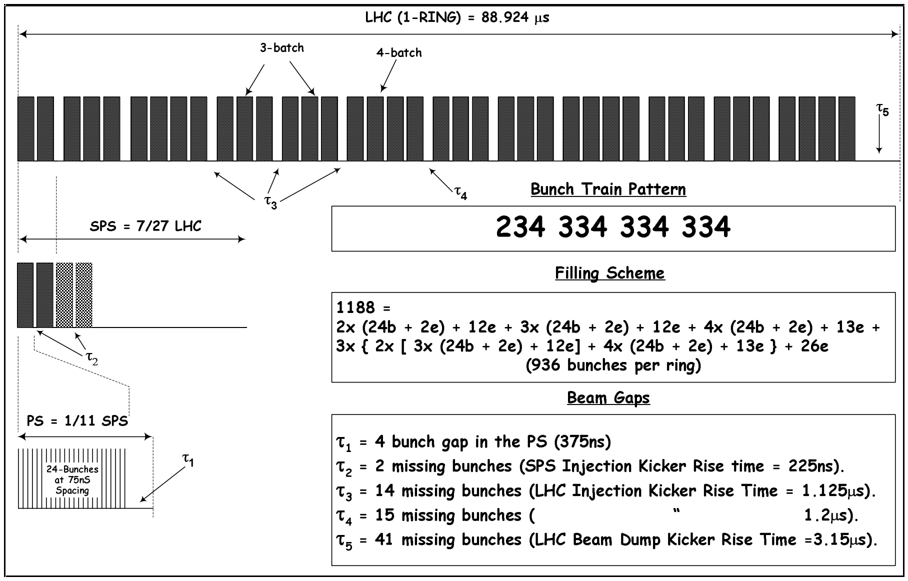

Figure 3.3: An example LHC bunch structure.

but could be different in different fills. The nominal filling scheme for high luminosity operation consists of ∼2800 proton bunches, in which empty BXs are used for beam injection and dump. The configurations of different filling schemes in the stopped particle searches can be retrieved from an LHC database. These filling scheme files help us to calculate some important quantities in the searches, such as the trigger livetimes and the effective luminosities.

3.2 The Compact Muon Solenoid

CMS is a general purpose detector with a length of 21.6 m, a diameter of 14.6 m and a weight of 13800 tons. As shown in Fig. 3.4, the detector is hermetic and is composed of different subdetectors in its central barrel and endcap regions. In this section, I will introduce different subdetectors from innermost to outermost. A more detailed description can be found in [23].

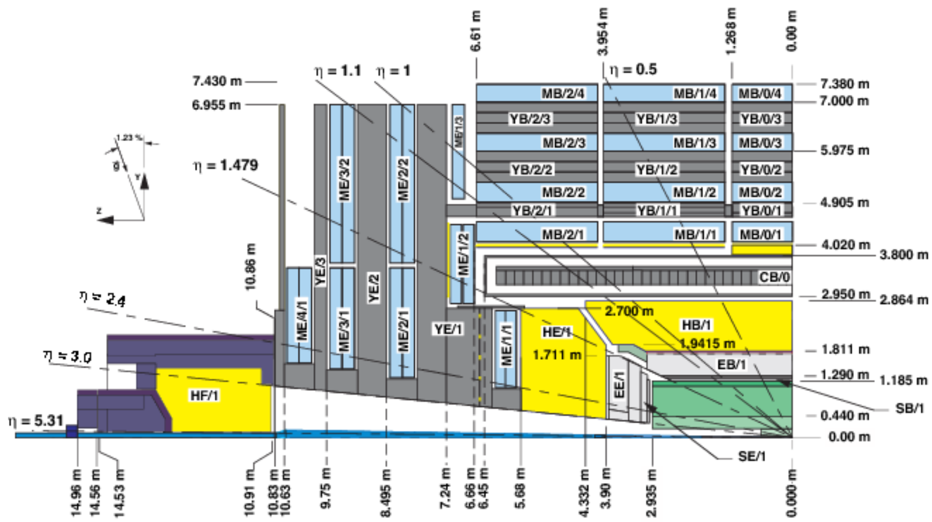

Figure 3.4: A longitudinal view of CMS detector.

3.2.1 Tracker System

The tracking system, which is based on silicon tracking technology, measures the trajectories and vertices of charged particles coming from the interaction point. The momenta of particles are obtained from the measurement of their curvatures in the magnetic field. The tracker uses p-n junctions to detect charged particles, which will release charge carriers when they pass through the depletion zone. The charge carriers will then drift to the electrodes and form an ionization current that is proportional to the ionization energy loss of the particles. The current is then read out by electronics.

The tracker system consists of the inner pixel detectors and the outer strip trackers. The pixel detectors have three barrel layers at $r = 4.4$, 7.3 and 10.2 cm, and two endcap layers at $z = \pm 34.5$ and $z = \pm 46.5$ cm. It covers a pseudorapidity range of $-2.5 < \eta < 2.5$. Outside the pixel detectors, the strip tracker is composed of 10 barrel layers and 9 endcap disks on each side. The thicknesses of the layers are minimized so that the trajectories of particles are not affected much. The whole tracker system has a radius of 113.5 cm and extends to $z = \pm 282$ cm, incorporating around 1400 pixel modules and 15000 strip modules in the tracker.

During the winter of 2016/2017[24], the pixel detector was upgraded due to radiation damage and high occupancy in the readout chip. The upgraded pixel detector has four barrel layers and three endcap disks. Its readout chip is now able to sustain higher rates and the new pixel detector can work efficiently with peak luminosity up to 2×10^{34} cm^{-2}s^{-1}.

3.2.2 ECAL

The electromagnetic calorimeter (ECAL) is a homogeneous calorimeter that consists of 75,000 lead-tungstate ($PbWO_4$) crystals and is shown in Fig. 3.5. The ECAL barrel (EB) covers the region with pseudorapidity $|\eta| < 1.48$ and the ECAL endcaps (EE) on both sides cover $1.48 < |\eta| < 3.0$. The ECAL is designed to measure the energy of electrons and photons. When an energetic electron or photon passes through the ECAL, it will induce an electromagnetic shower via bremsstrahlung or pair production.

The lead-tungstate crystal has a short radiation length (0.89 cm), a small Moliere radius (2.2 cm), and it is a fast scintillator so that around 80% of the scintillation light is emitted in an LHC bunch crossing time (25 ns). Twenty-six radiation lengths of the lead-tungstate crystal are used to limit the shower leakage. The blue-green

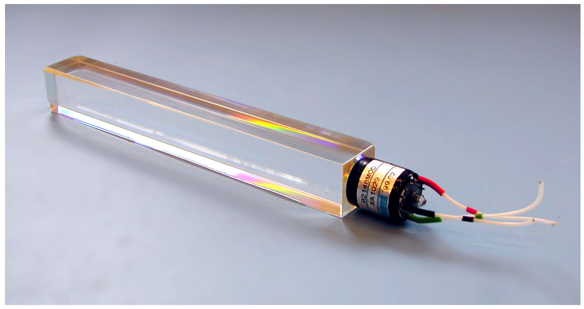

Figure 3.5: $PbWO_4$ crytal with the photodetector attached on its back

scintillation light induced by the electromagnetic showers is collected by photodetectors at the back of the crystals. Avalanche photodiodes (APDs) are used in the EB and vacuum phototriodes (VPTs) are used in the EE, since APD is able to provide gain in a high transverse magnetic field while the VPT can survive a higher radiation dose and neutron fluence.

3.2.3 HCAL

The hadronic calorimeter (HCAL) is divided into four subdetectors, in which the HCAL barrel (HB) and the HCAL endcap (HE) are the major parts that surround the ECAL. Each of them covers the whole azimuthal angle ϕ range. The HB covers $|\eta| < 1.4$, while the HE covers the range of $1.3 < |\eta| < 3.0$. At the far ends of both sides, the HCAL forward (HF) detectors extend the $|\eta|$ coverage up to 5.0. And the HCAL outer barrel (HO) is placed outside the iron yoke to further increase the effective HCAL thickness.

The HB and HE detectors are sampling calorimeters with brass/stainless steel absorbers and plastic scintillators, as shown in Fig. 3.6. Brass and stainless steel

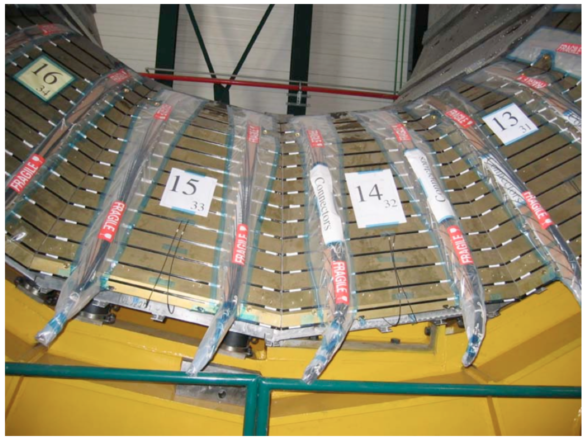

Figure 3.6: Several wedges of the HB detector, where several layers of dense absorbers can be seen, and scintillators are placed between them.

have large nuclear interaction lengths due to their density. In the detector nine interaction lengths of brass were stacked together to absorb 99% of the energy. These two subdetectors are segmented into cells that span of 0.087×0.087 in $\eta - \phi$ space in the barrel and are more coarsely granulated in η in the regions where $|\eta| > 1.74$. The HB provides the most important measurement of the energy of hadrons for the stopped particles calorimeter search.

When a strongly interacting particle strikes the absorbers, it will produce a shower of a bunch of secondary particles. A typical hadronic shower is shown in Fig. 3.7. If these particles leave deposits in the scintillators between the absorbers, the blue-violet scintillation light is then read out by the external electronics.

The scintillation light of hadronic showers from 18 channels at the same ϕ is collected by one hybrid photodiode (HPD). The HPD signals are digitized by seven-bit analog-to-digital converters for readout. The signals of 4 HPDs are digitized in a single read-out box (RBX) that has 72 channels.

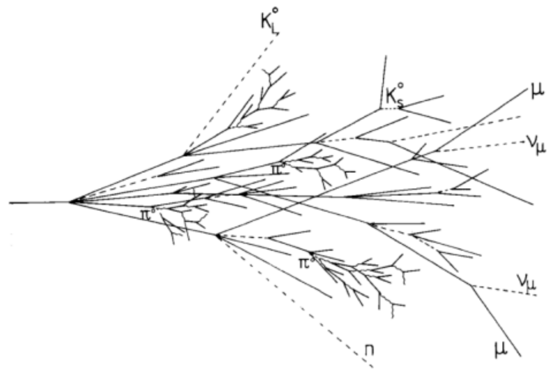

Figure 3.7: An illustration of a typical hadronic shower.

A number of channels in the HCAL detector show temporary or permanent problems that produce signals in the absence of showering particles. These abnormal HCAL noises signals include ion feedback, HPD noise, and RBX noise[25].

Ion feedback is when a thermally emitted electron ionizes the gas. The ion ends up emitting more electrons after being accelerated and hitting the cathode. Ion feedback normally produces fake signals in one or two HPD channels. HPD noise is produced when the misalignment between the electric field in the HPD and the solenoid field lowers the flashover voltage, producing significant energy deposits in a large number of HPD channels due to electron avalanches. RBX noise features energy deposits usually in more than half of the channels in an RBX. The mechanism of the RBX noise is not well understood, but its unique characteristics make it easy to recognize.

3.2.4 Muon System

The muon system, which is the outermost part of the CMS detector, is responsible for muon identification and reconstruction, which are very important to CMS since muons are among the final products of many interesting processes. The muon system consists of three gaseous subdetectors in the barrel and endcap regions outside of the solenoid coils, and the system covers the pseudorapidity range of $|\eta| < 2.4$, as shown in Fig. 3.8. As the muon passes through the muon system, we can measure its momentum based on the position and timing measurements of its curved trajectory.

The three subdetectors operate in a similar way: An energetic muon ionizes the gas atoms when passing through the detector. The free electrons are then accelerated in the electric field and ionize more atoms. The resulting avalanche of electrons is then recorded by the readout.

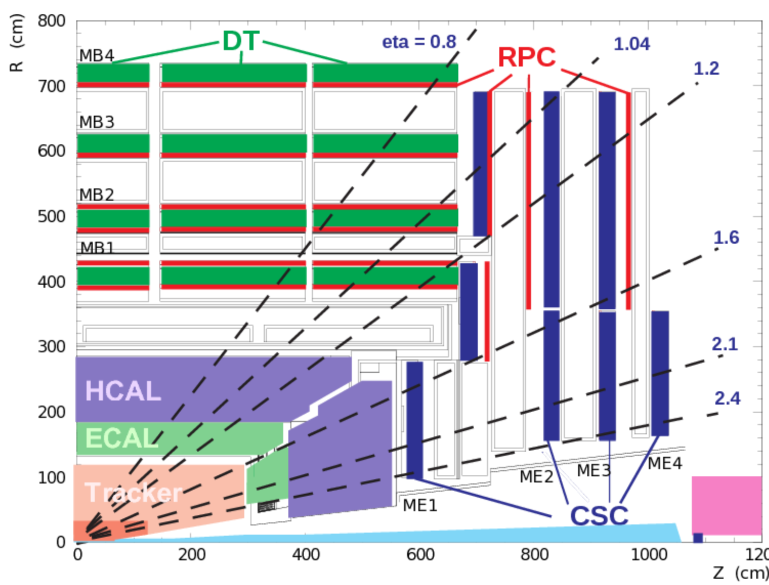

Figure 3.8: A longitudinal view of the CMS detector, where the three different components of the muon system are highlighted.

In the barrel region, since the muon rate is relatively low and the magnetic field is uniform, drift tube (DTs) chambers are used and cover a pseudorapidity region of $|\eta| < 1.2$. In the endcaps where the muon rate is high and the magnetic field is changing, cathode strip chambers (CSCs) are used for precision muon measurements within $0.9 < |\eta| < 2.4$. Meanwhile, resistive plate chambers (RPCs) are used in both the barrel and the endcaps to provide good time resolution and a redundant trigger system for the identification of bunch crossing and fast preliminary measurement of muon p_T.

3.2.5 Particle Identification and Measurement

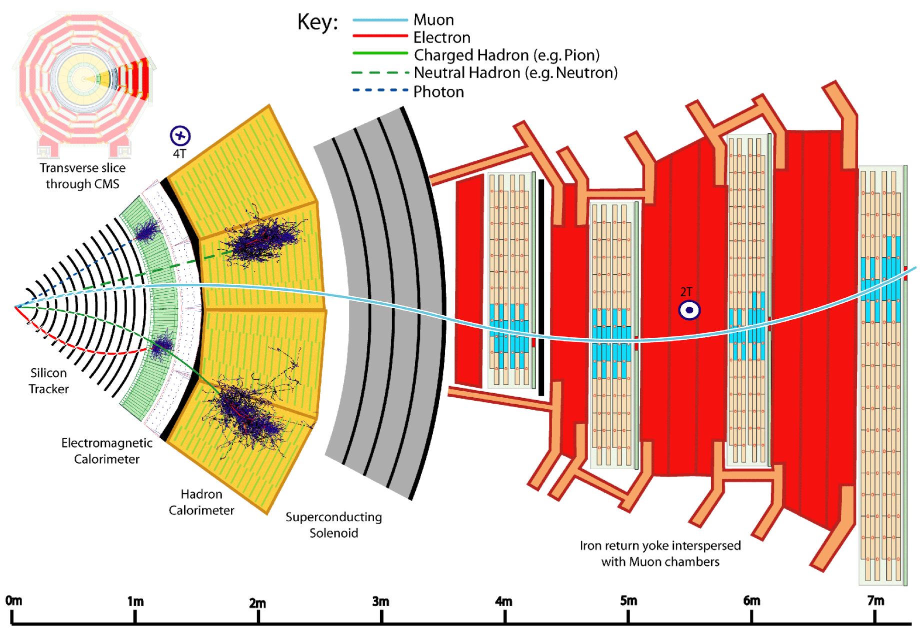

Figure 3.9: A cross sectional view of the CMS detector and how the particles interact with it.

Figure 3.9 shows how particles interact in a cross-sectional view of the CMS detector . Charged leptons and hadrons will be bent by the magnetic field and leave hits in the tracker system when passing through, which could later be reconstructed as tracks, giving the p_t information of the particles. Outside the tracker, charged particles, as well as photons, will leave energy deposits when they shower in the ECAL. However, only electrons and photons would lose all of their energy due to their small masses. In the HCAL, hadrons like π, K, which are strongly interacting, shower and the energy of the resulting jets can be measured. Due to their relatively large mass and since they only interact electromagnetically, muons will pass through the detector and interact with the trackers and muon chambers. The hits in the trackers and the muon chambers could help identify the muons and help to measure their momenta more precisely. Neutrinos only interact weakly and will not leave any hits in the detector. However, they can be observed indirectly by measuring the missing transverse energy.

3.2.6 Trigger and Data Processing in CMS

As the integrated luminosity increases, the number of hard interactions increases as well. However, due to the limitation of the storage and the fact that not all hard scattering events are interesting for the probing of new physics, only those interesting events (Higgs decay, for example) are recorded. To achieve this, CMS is designed with a 2-level online trigger system: the Level-1 (L1) trigger and the high level trigger (HLT). The trigger system helps to reduce the recorded events rate down to 1000 Hz, which is within the storage capacity of the disk hardware.

Level-1 Trigger

Every pp collision event is analyzed by the level-1 (L1) trigger, which is integrated into the hardware. Due to the large event rate (40 MHz), the L1 system needs to make the decision on whether to accept the event within 3.2 μs. Event rates are reduced down to 100 KHz by the L1 trigger, and these events are then transferred to the HLT computer farm for further processing. The L1 trigger includes a muon trigger, which uses information from the muon systems, and a calorimeter trigger, which uses the information from the calorimeters. The measurements from the tracker system, which is the closest detector to the beam pipe, are not exploitable by the current CMS L1 trigger, due to the fact that the particle flux is very high and the complicated algorithms need more time than is available in the L1 trigger to make a fast decision.

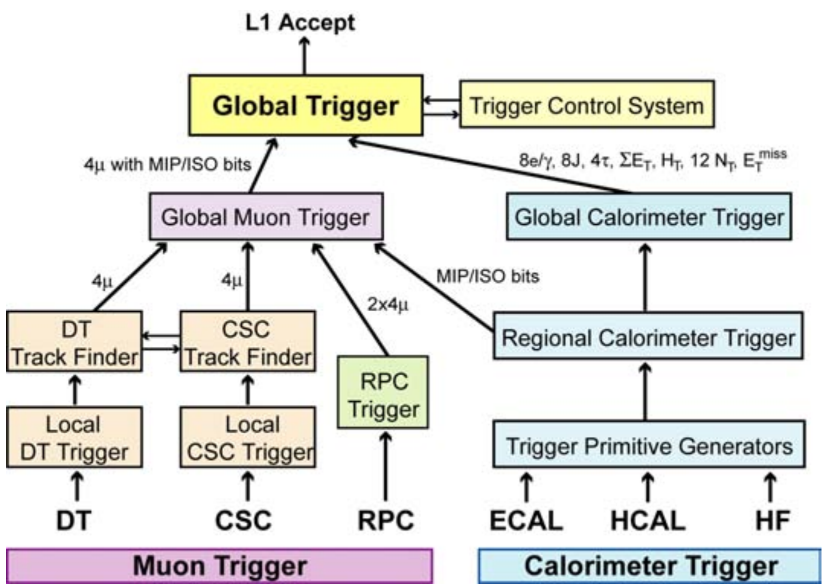

Figure 3.10: The configuration of L1 trigger.

As shown in Figure 3.10, the Global Muon Trigger receives muon candidates from local track finder electronics in the DTs and CSCs. The RPCs also provide a trigger for quick decision making. The Global Muon Trigger selects four best muon candidates and sends then to the Global Trigger. The Global Calorimeter Trigger receives the calorimeter information from the Regional Calorimeter Trigger, and provides good candidates such as electrons and jets to the Global Trigger. The Global Trigger includes a maximum of 128 bits, which correspond to different L1 decisions. The data is kept and sent to the HLT if any of these trigger bits returns a boolean true value.

High Level Trigger

The software based HLT system utilizes the digitized data from the subdetectors. Since the HLT is designed to recognize and store the events we are interested in, higher precision is needed. This means that we need more computation and storage resources to process and store the events. As a result, the rate of the HLT cannot be too high, and only about a thousand events per second are selected by the HLT.

Each physics analysis usually uses a few HLT algorithms, which are called HLT paths. The HLT paths consist of a series of modules that can be shared across different paths. These modules use similar but simplified algorithms comparing to the offline reconstruction. The events selected by the any of the paths will be transferred to the next step, which is data processing.

Data Processing in CMS

The selected events are further divided into multiple datasets, depending on the type of the HLT path. For example, the events used by the stopped particles searches are all stored in the NoBPTX dataset, since the corresponding HLT paths require the events to be at least 2 BX away from any collision event.

The events are first stored as RAW data, which contains electronics readout, the L1 decisions, and the trigger primitives. The offline reconstruction reconstructs the necessary higher level objects for physics analyses including muons, electrons, photons, and jets. The events containing these objects are then stored as RECO data. There are also some slimmed down versions of the RECO data, such as analysis object data (AOD) and miniAOD, that contains only the most relevant information for physics analyses to reduce the reading time for the analysis. In case of the stopped particles searches, we use RECO data since some key discriminating variables in our searches, such as HCAL timing variables, are not accessible in AOD or miniAOD data.

Chapter 4: Search for Stopped Particles Decaying to Jets

4.1 Introduction

Massive long-lived particles (LLP) are predicted in many extensions of the SM [21, 26, 27, 28, 29, 30, 5, 31]. At the CERN LHC, two general purpose detectors, CMS and ATLAS, have collected data from p-p collisions that are used for searches for BSM particles. Most traditional searches look for prompt decays of BSM particles and have limited sensitivity to particles that have lifetimes longer than a b quark. Dedicated searches for long-lived particles have been performed so that we don't miss the chance of discovering BSM particles with large lifetimes.

LLPs could exhibit different signatures in the detector depending on their lifetimes and how they decay. If their lifetimes are much shorter than the scale of the detector, LLPs could leave signatures of displaced objects, such as displaced jets [32, 33], displaced leptons [34, 35], displaced vertices [36, 37, 38], etc. Other unique signatures include disappearing tracks [39, 40] and kinked tracks [41].

Another interesting scenario is if the lifetime of the LLP is longer than the scale of the detector. In that case, a lot of the particles will leave the detector before decaying. If these LLPs interact strongly, such as the gluino or the stop do, they will form bound-states called R-hadrons, which are counterparts of hadrons in the SM.

These heavy (quasi)-stable particles (HSCPs) are predicted in theories such as split-SUSY. If the HSCP is charged, it appears like an energetic muon in the detector, except it has larger ionization energy loss (dE/dx) and it takes a longer time to reach the muon detector, since it is massive. The time a particle takes to reach a certain detector is called the time-of-flight (TOF). Both CMS[19] and ATLAS[18] have performed searches based on these two features of HSCPs.

While HSCP searches have good sensitivity to LLPs with lifetimes from tens of nanoseconds up to infinity, the searches are not able to measure the LLP lifetime directly. The stopped particles search serves a complement to the HSCP search by looking for decays of LLPs that are trapped in the detector, giving a chance to actually measure the lifetime of LLPs.

Due to their heaviness, R-hadrons acquire an initial velocity relatively smaller than SM particles after pair production. While traversing the detector, R-hadrons interact with the material via the electromagnetic interaction if they are electrically charged and/or strong interaction if they carry color. If their velocity is below a certain critical value (∼0.4 c), they could lose all their kinetic energy and stop in the densest parts of the detector, such as the HCAL or the iron yokes in the muon system [17]. The stopped LLPs would sit inside the detector for a while before they decay. This "stop-and-decay" procedure will be reconstructed into individual "stopping" and "decaying" events, as long as they are well separated by several BXs. Here we are interested in the subsequent "decaying" events.

The decaying procedure could be hadronic, semi-leptonic or leptonic, depending on the decaying mother particle and the decay channel. Here we are more interested in the decay process that involves the strong interaction due to its much larger cross-sections. We consider two decaying scenarios: LLPs decaying to jets and LLPs decaying to a pair of muons. In the former case, the calorimeter is the ideal place to observe the decay since the showering of decays in the iron yokes will be mostly absorbed by the un-instrumented material. In the latter case, no matter where the LLPs stop, it is always likely to observe the signal.

Also, if the decay happens when there are collisions in the detector, there's little chance we can observe the signal due to the dominant QCD and $W^{\pm}/Z$ SM backgrounds. Fortunately, in LHC beams, there are bunch positions that are left empty, as illustrated in the Chapter 3.1.2. These empty bunches provide us with a good opportunity to observe the signals. In these intervals, the detector will be quiet except when there are occasional non-SM backgrounds, such as cosmic ray muons, halo muons or HCAL instrumental noise.

In this chapter, I will explain the search for the stopped particles that decay to jets (calorimeter based search). The search for stopped particles that decay to a pair of muons (muon search) will be introduced in next chapter. The calorimeter search is performed over data by the CMS detector during the 2015 and 2016 data-taking periods, using 2015 data corresponding to 2.7 fb^{-1} and 2016 data corresponding 35.9 fb^{-1}. The results of earlier calorimeter searches have been reported by the D0 [42], CMS [43, 44, 45] and ATLAS Collaborations [46, 47].

4.2 Triggers

The 2015 data for this search are collected with a dedicated trigger, which requires the presence of at least one jet that does not coincide with any pp collisions. The Beam Pick-up Timing for eXperiments (BPTX) detectors are mounted on the beam pipe on both sides of the CMS at $z=\pm175$ m. They consist of LHC button electrodes that measure the position, timing, and intensity of the beams. The trigger accepts the event only if the BPTX determines that there is no beam in either direction in the BX in which the jet is observed. This is implemented by requiring that the trigger bit BptxOr must be false. To further reduce the number of background events, the trigger also requires that there are no beams in the ±1 BX with respect to the current BX; in other words, the BptxOr should be false in the current BX as well as ±1 BX. Thus the trigger is most likely to collect events that happen between the bunch trains and during the abort gap, which is shown in Fig. 3.3.

When a massive stopped LLP decays in the HCAL, its hadronic decay products will be reconstructed as highly energetic jets as long as the mass difference between the LLP and its daughter particles is large. On the other hand, the jet reconstructed in background events due to either showering or instrumental noise has much smaller energy, and this energy decreases exponentially. To reject a significant amount of background events while keeping as many signal events as we can, our trigger requires that the reconstructed energy of the jet must be at least 50 GeV. To reject beam halo events, the trigger requires that the L1_SingleMuBeamHalo trigger bit has fired and the $|\eta|$ of the reconstructed jet is smaller than 3.0.

There are two prescaled control triggers in 2015, HLT_JetE30_NoBPTX3BX_NoHalo_v1 and HLT_JetE30_NoBPTX_v1. Events that pass these control triggers are used to produce the trigger efficiency turn on curve, which is shown in Fig. 4.1. The trigger rate during 2015 is shown in Fig. 4.3. A safety trigger, HLT_JetE70_NoBPTX3BX_NoHalo_v2, was implemented but was not needed.

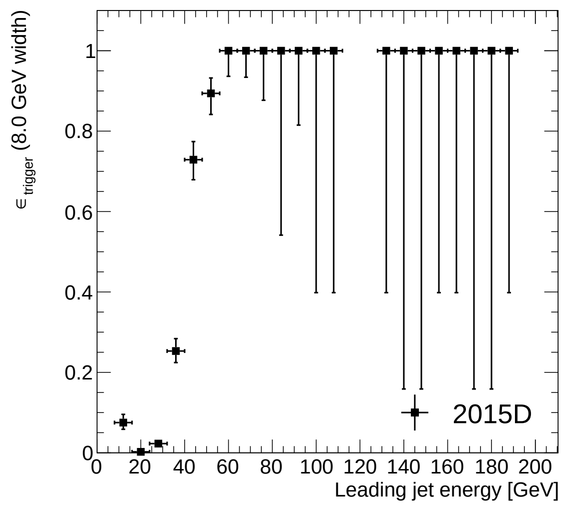

Figure 4.1: Trigger turn on in 2015.

In the 2016 search period, the names of our HLT paths and their L1 seeds are changed due to effects related to the upgraded L1 trigger. In particular, the HLT path names are changed because L1_SingleMuBeamHalo was no longer present in the 2016 L1 menu, which means that we can no longer veto this L1 bit. The upgraded L1 firmware could not easily support L1_SingleMuBeamHalo, and we determined that it did not save a lot of rates, so it was dropped from the menu. Furthermore, the L1 seed names are changed because the ± 1 BX veto was moved from the HLT to L1 since the upgraded L1 could handle this feature. In addition, the L1 jet energy threshold increased to 40 GeV by the end of the year in order to handle the increased rate. Table 4.3 summarizes the triggers we used in 2016, and the turn-on curve in 2016 search sample is shown in Fig. 4.2. The rate of the HLT signal path during 2016 search sample is shown in Fig. 4.4.

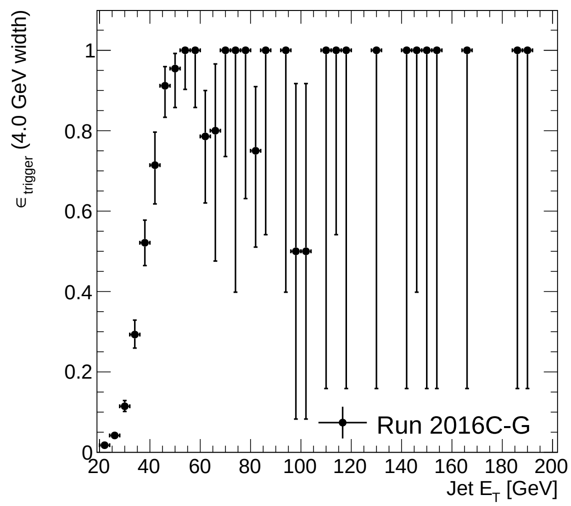

Figure 4.2: Trigger turn on in 2016.

4.3 Datasets

In both 2015 and 2016, we use data collected by our trigger during collision runs as the search samples, in which we are looking for the signal. More specifically, in 2015 we use 2.7 fb^{-1} of 13 TeV data taken during collision data taking periods, which are between August and November 2015. While in 2016, we analyze 35.9 fb^{-1} of 13 TeV data taken in collision data taking periods between May and October 2016. These data are certified to be good to use in physics analyses by the subdetector experts. The following official JSON files define the lumisections (23 s intervals during data taking) in which data are certified to be good.

`https://cms-service-dqm.web.cern.ch/cms-service-dqm/CAF/certification/Collisions15/13TeV/Reprocessing/Cert_13TeV_16Dec2015ReReco_Collisions15_25ns_JSON_Silver_v2.txt`

Table 4.1: Triggers designed for this analysis available in the 2015 pp collisions menu. Prescales are given for the end of the 2015 pp collisions run. The signal path is used to collect the data for this search.

Purpose	HLT path	L1 seed
Control	HLT_JetE30_NoBPTX_v2	L1_SingleJetC20_NotBptxOR
Control	HLT_JetE30_NoBPTX3BX_NoHalo_v2	L1_SingleJetC20_NotBptxOR
Signal	HLT_JetE50_NoBPTX3BX_NoHalo_v2	L1_SingleJetC32_NotBptxOR
Backup	HLT_JetE70_NoBPTX3BX_NoHalo_v2	L1_SingleJetC32_NotBptxOR

Table 4.2: Rates for Level 1 seeds and HLT paths in run 20627, the last run of the 2015D era that was certified for inclusion in the silver JSON file.

L1 seed / HLT path	Rate after prescale (Hz)
L1_SingleJetC20_NotBptxOR	328
L1_SingleJetC32_NotBptxOR	1533
HLT_JetE30_NoBPTX_v2	0.01
HLT_JetE30_NoBPTX3BX_NoHalo_v2	0.08
HLT_JetE50_NoBPTX3BX_NoHalo_v2	1.1
HLT_JetE70_NoBPTX3BX_NoHalo_v2	0.6

Table 4.3: Triggers designed for this analysis available in the 2016 pp collisions menu. Prescales are given for run 276384. The signal path is used to collect the data for this search.

Purpose	HLT path	L1 seed
Control	HLT_JetE30_NoBPTX_v3	L1_SingleJetC20_NotBptxOR
Control	HLT_JetE30_NoBPTX3BX_v3	L1_SingleJetC20_NotBptxOR_3BX
Signal	HLT_JetE50_NoBPTX3BX_v2	L1_SingleJetC40_NotBptxOR_3BX
Backup	HLT_JetE70_NoBPTX3BX_v2	L1_SingleJetC40_NotBptxOR_3BX

https://cms-service-dqm.web.cern.ch/cms-service-dqm/CAF/certification/

Collisions16/13TeV/ReReco/Final/

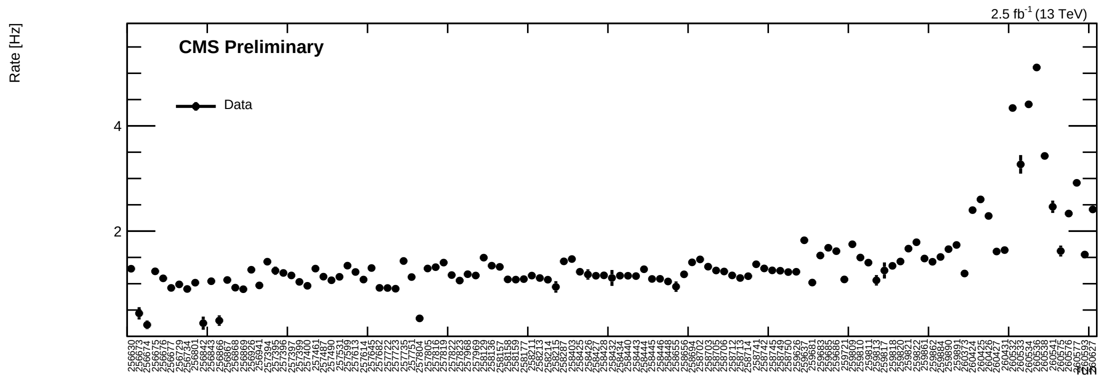

Figure 4.3: Trigger rate in 2015.

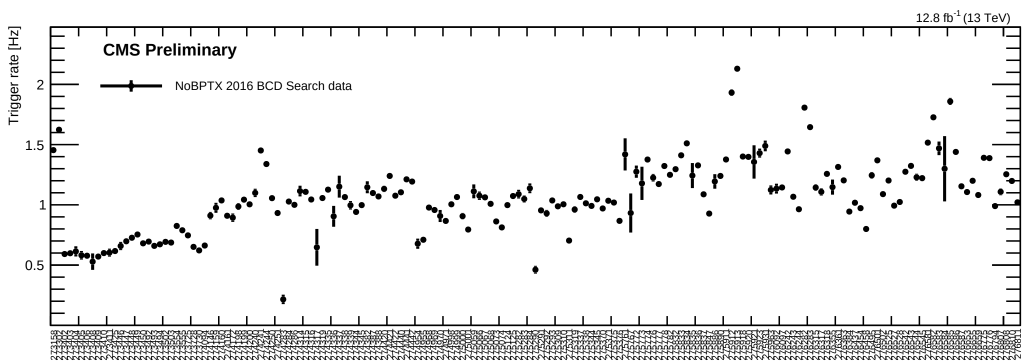

Figure 4.4: Trigger rate in 2016.

`Cert_271036-284044_13TeV_23Sep2016ReReco_Collisions16_JSON.txt`

The trigger livetime of a searching period is defined as the total amount of time during which the trigger is ready to capture the signal. Based on the acceptance criteria of our trigger, the livetime includes all BXs that have no beam in the current BX as well as their nearest neighbors (± 1 BX). The livetime helps us to calculate the background event rate, which is a necessary ingredient for the counting experiment, as we'll see in Chapter 4.9.1. Based on the filling schemes in 2015 and 2016, which are shown in Table 4.4 and Table 4.5, the trigger livetimes of the 2015 and 2016 search periods are calculated to be 135 hours and 586 hours respectively.

Table 4.4: The LHC filling schemes used for fills in the 2015 search dataset.

Name	$N_{collision}$/orbit	Livetime fraction
25ns8b4e_529b_517_279_444_112bpi8inj	517	80%
25ns_601b_589_540_552_144bpi7inj_sp	589	80%
25ns_601b_589_438_459_96bpi9inj_bcms	589	81%
25ns_893b_881_828_830_72bpi17inj	881	73%
25ns_1033b_1021_878_885_144bpi10inj	1021	69%
25ns_1177b_1165_1080_1110_144bpi11inj	1165	65%
25ns_1321b_1309_1105_1134_144bpi12inj	1309	60%
25ns_1464b_1452_1218_1248_144bpi12inj_sp	1452	56%
25ns_1465b_1453_1243_1278_144bpi13inj	1453	56%
25ns_1608b_1596_1356_1392_144bpi13inj_sp	1596	52%
25ns_1825b_1813_1495_1536_144bpi16inj_sp	1813	46%
25ns_2244b_2232_1731_1866_144bpi19inj_36	2232	32%

To estimate the instrumental noise in the search, we need a signal free, noise dominant sample which we can use to estimate the efficiency of our HCAL noise rejecting criteria. Cosmic ray data, which are taken between collision data taking periods, are the ideal candidates for this purpose, since the events collected in these runs are either cosmic ray events or HCAL noise events. We use events collected in 2015 and 2016 cosmic ray data taking periods as our control samples for the 2015 and 2016 analyses respectively. The HCAL conditions in these data are confirmed to be good.

Table 4.5: The LHC filling schemes used for fills in the 2016 search dataset.

Name	$N_{collision}$/orbit	Livetime fraction
25ns_601b_589_552_552_72bpi_11inj	589	81%
25ns_601b_589_552_552_72bpi_11inj_950ns	589	81%
25ns_601b_589_552_552_72bpi_11inj_alt	589	81%
25ns_602b_590_552_552_72bpi_12inj_950ns	590	81%
25ns_889b_877_810_828_72bpi_15inj_950ns	877	72%
25ns_1177b_1165_967_972_72bpi_19inj	1165	64%
25ns_1177b_1165_990_984_72bpi_19inj	1165	64%
25ns_1465b_1453_1122_1153_72bpi_23inj	1453	56%
25ns_1752b_1740_1470_1499_72bpi_26inj	1740	48%
25ns_1824b_1812_1539_1571_72bpi_27inj	1812	46%
25ns_2040b_2028_1697_1712_72bpi_30inj	2028	39%
25ns_2076b_2064_1692_1765_96bpi_23inj	2064	37%
25ns_2076b_2064_1717_1767_96bpi_23inj	2064	37%
Multi_55b_11_28_16_4bpi14inj	11	91%
Multi_56b-52b_32_16_8_4bpi14inj	32	93%

4.4 Monte Carlo Simulation

The Monte Carlo simulation signal samples used by this search are gluinos and stops that are pair produced and R-hadronized [48, 49]. In the gluino decay scenarios, $\tilde{g} \to g\tilde{\chi}^0$ and $\tilde{g} \to q\bar{q}\tilde{\chi}^0$ are simulated. These two processes correspond to the tree level and loop diagrams of gluino decays in the theory of split-SUSY. The decay channel of the stop in the simulation is assumed to be $\tilde{t} \to t\tilde{\chi}^0$. We consider gluino and stop masses between 100 GeV and 2600 GeV.

The signal generation is done in two individual stages, whose methodology is similar to that described in [45]. In the first stage, gluinos and stops are pair produced and then produce R-hadrons using PYTHIA8.205 [50] with PDF tune CUETP8M1. Their passage through the detector is simulated by Geant4 [51, 52]. A "cloud" [53, 54] model is used to describe the interaction between the R-hadrons and the detector material. The momenta of R-hadrons are monitored during this process so that when they become 0, the corresponding R-hadrons are regarded as being stopped and their positions, as well as their flavors, are recorded for later use. This stage of the simulation helps us understand how many R-hadrons would stop in the regions we are interested in.

In the second stage, static R-hadrons are generated with the recorded flavors and positions and decayed using PYTHIA 6 [55], and the detector response is simulated via another GEANT 4 step. This stage allows us to determine how much of the decaying signals would pass our offline selection criteria.

The same first stage samples are used in both the 2015 and 2016 searches, while the stage2 samples are re-reconstructed in 2016 due to the change of the central recipe.

4.4.1 Stopping Efficiency

The stage1 simulation helps us determine the probability for an R-hadron to stop within the instrumented region of the detector, which is defined as the stopping efficiency ($\varepsilon_{\text{stopping}}$). In the calorimeter search, although the R-hadrons are most likely to stop in the densest part of the detector, we are only interested in the those that stopped in the HB and EB, where the jets from the decays can be easily observed since backgrounds are relatively low. The number of R-hadrons that stop in the tracker is negligible according to the simulation.

Fig. 4.5 shows $\varepsilon_{\text{stopping}}$ as a function of $m_{\tilde{g}}$ and $m_{\tilde{t}}$ for a center-of-mass energy of 13 TeV, when we require that the stopped R-hadrons are in the HB and EB. The $\varepsilon_{\text{stopping}}$ is greater for $\tilde{g}$ R-hadrons than $\tilde{t}$ R-hadrons because $\tilde{g}$ R-hadrons are more likely to be doubly charged (see Fig. 4.6). Furthermore, the difference in the dependence on mass between the gluinos and stops is explained by the difference in the behavior of the tails of the p_T distributions (see Fig. 4.7). The stop p_T distribution has a longer tail than the gluino p_T distribution, and as the mass increases, the tail of the stop p_T distribution increases more than that of the gluino. As a result, less of the high mass stops have sufficiently low p_T for them to stop in the detector, and so the stopping efficiency plateaus. On the other hand, for the gluinos, the p_T distribution has less of a long tail as the mass increases, and so the stopping efficiency can increase.

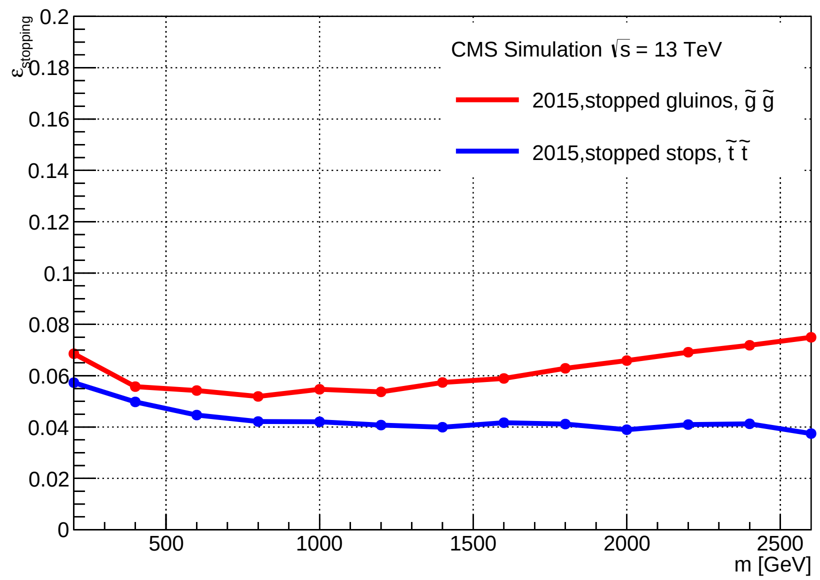

Figure 4.5: Stopping probability for $\tilde{g}$ and $\tilde{t}$ R-hadrons as a function of the mass of the decay daughter particle for the 2015/2016 MC simulation samples. The same GEN-SIM samples are used in both the 2015 and the 2016 analyses, so the stopping efficiency is exactly the same for both analyses. The $\varepsilon_{\text{stopping}}$ is greater for $\tilde{g}$ R-hadrons than $\tilde{t}$ R-hadrons because $\tilde{g}$ R-hadrons are more likely to be doubly charged.

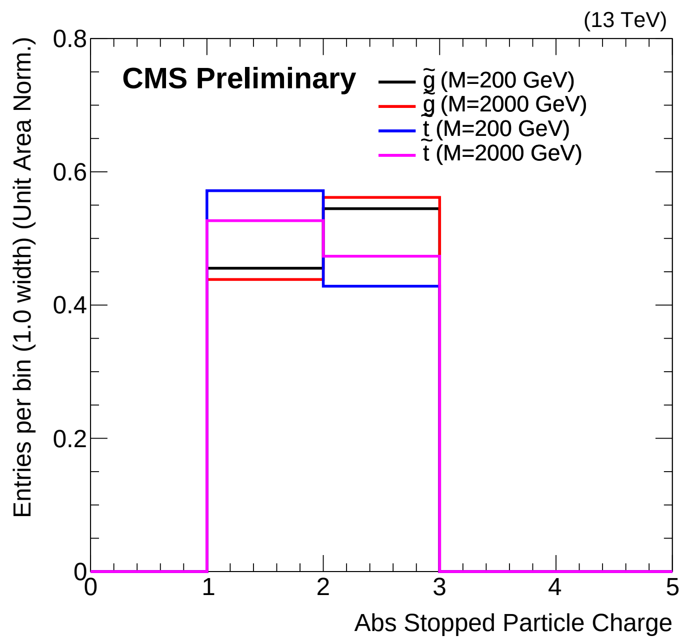

Figure 4.6: The absolute value of the charge of the stopped particle, for $\tilde{g}$ and $\tilde{t}$ R-hadrons at 13 TeV The $\tilde{g}$ R-hadrons are more likely to be doubly charged than the $\tilde{t}$ R-hadrons.

The overall stopping efficiencies at 13 TeV are lower than those at 8 TeV, for both gluinos and stops, due to the increase of their initial kinetic energy as the result of the collision energy boost.

Figure 4.8 shows the positions in CMS of the stopped gluinos from the stage 1 simulation.

4.4.2 Trigger efficiency

In the stage2 simulation, we estimate the $\varepsilon_{\text{reco}}$, which estimates the probability for the signals in the HB and HE passing our analysis selection criteria. Let's first

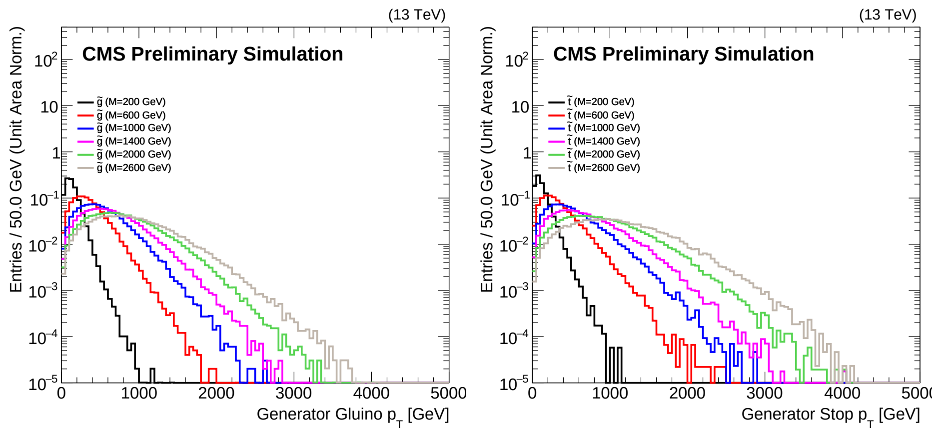

Figure 4.7: The generated p_T of the $\tilde{g}$ (left) and the $\tilde{t}$ (right) for several different masses, before hadronization.

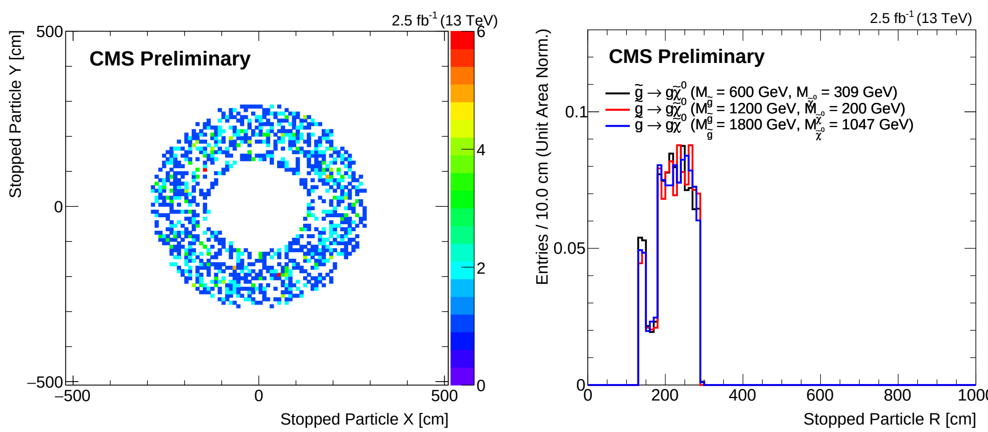

Figure 4.8: Stopping positions for $\tilde{g}$ R-hadrons, for those that come to rest within the EB and HB. The y position as a function of the x position for $m_{\tilde{g}} = 1200$ GeV and $m_{\tilde{\chi}^0} = 200$ GeV (left), and the radial position for $m_{\tilde{g}} = 600$ GeV and $m_{\tilde{\chi}^0} = 309$ GeV, $m_{\tilde{g}} = 1200$ GeV and $m_{\tilde{\chi}^0} = 200$ GeV, and $m_{\tilde{g}} = 1800$ GeV and $m_{\tilde{\chi}^0} = 1047$ GeV (right). For the left plot, the colors indicate the number of events in each bin.

consider the trigger efficiency, which is the probability for the signals in the HB and HE to pass our HLT path.

The trigger efficiency for gluino R-hadrons that come to rest in the CMS detector is shown in Fig. 4.9. The efficiency is $\sim 65\%$ for gluinos and stops that decay to a gluon with an energy of 100 GeV or a 180 GeV top, independent of the gluino or stop mass. The trigger efficiency in 2016 the simulation is slightly higher than that in 2015, which is due to the removal of the L1 beam halo filter in our 2016 trigger.

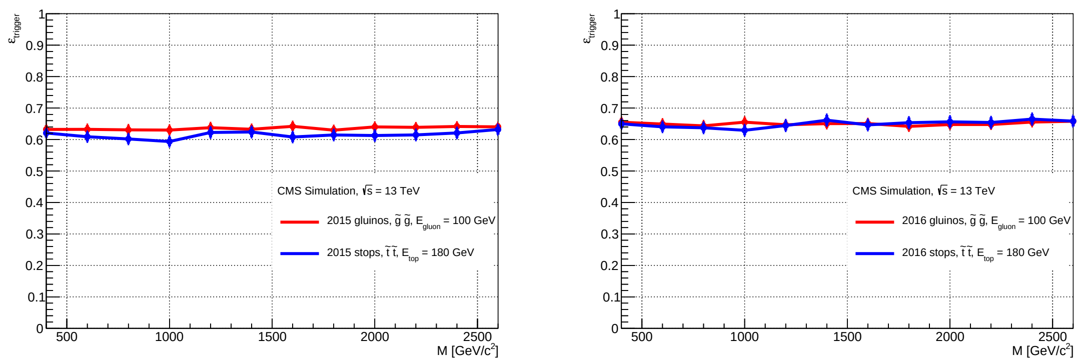

Figure 4.9: Trigger efficiency for $\tilde{g}$ R-hadrons that decay to a gluon with an energy of 100 GeV and $\tilde{t}$ R-hadrons that decay to a top quark with an energy of 180 GeV. As beam halo filter is removed in 2016 trigger, the trigger efficiency of 2016 simulation is slightly higher than that in 2015.

4.5 Event Selection

In this search, we are looking for hadronic decays of LLPs in the calorimeter that produce energy deposits that are reconstructed as one or more high-energy jets. We trigger on events including at least one jet with energy greater than 50 GeV and $|\eta| < 3$ that are at least two BXs away from any pp collisions.

The major backgrounds in this search are cosmic rays, beam halo, and HCAL noise. Cosmic ray and beam halo muons could emit a high energy photon via Bremsstrahlung radiation. The photon shower is then reconstructed as a jet and thus could be mistaken as a signal. The HCAL noise, on the other hand, does not come from any high energy particles. It's from the accidental ionization of gas in the accelerated region in the readout system of the HCAL. HCAL noise could occur in a single HPD or even the whole RBX. This noise could give rise to a large HCAL readout and thus the reconstruction of spurious high energy jets. The details of the HCAL noise have already been discussed in Chapter 3.2.3.

There are secondary backgrounds in the calorimeter search, such as jets from pp collisions of the remnant protons between proton bunches, and beam-gas interactions. We require that there are no reconstructed vertices in the events to ensure that the secondary backgrounds are negligible.

Since the rates of background events decrease exponentially as the jet energy increases, we require that the event should have at least one calorimeter based jet with energy greater than 70 GeV. Jets used in this search are reconstructed using the anti-kt algorithm [56, 57] with the $R = 0.4$. We also require that the $|\eta|$ of the leading jet is less than 1.0 to further improve the sensitivity, by excluding the majority of jets from the beam halo events. Besides these, specific selection criteria are developed to greatly reduce the background events while keeping as many signal events as we can.

4.5.1 Cosmic Ray Muon Rejecting Criteria

Cosmic ray events are the major background in this analysis. Usually, cosmic ray muons will leave hits in both the upper hemisphere and lower hemisphere of the detector, which could be reconstructed as muon tracks. But in rare cases when the cosmic ray muons pass through the uninstrumented regions in the detector, they will leave fewer hits, which are not enough to be reconstructed as a complete track. To maximize our capability of excluding these rare cosmic ray events, instead of requiring the events to have no muon tracks, we exploit the topology of DT and CSC chamber segments as well as RPC hits in the muon systems.

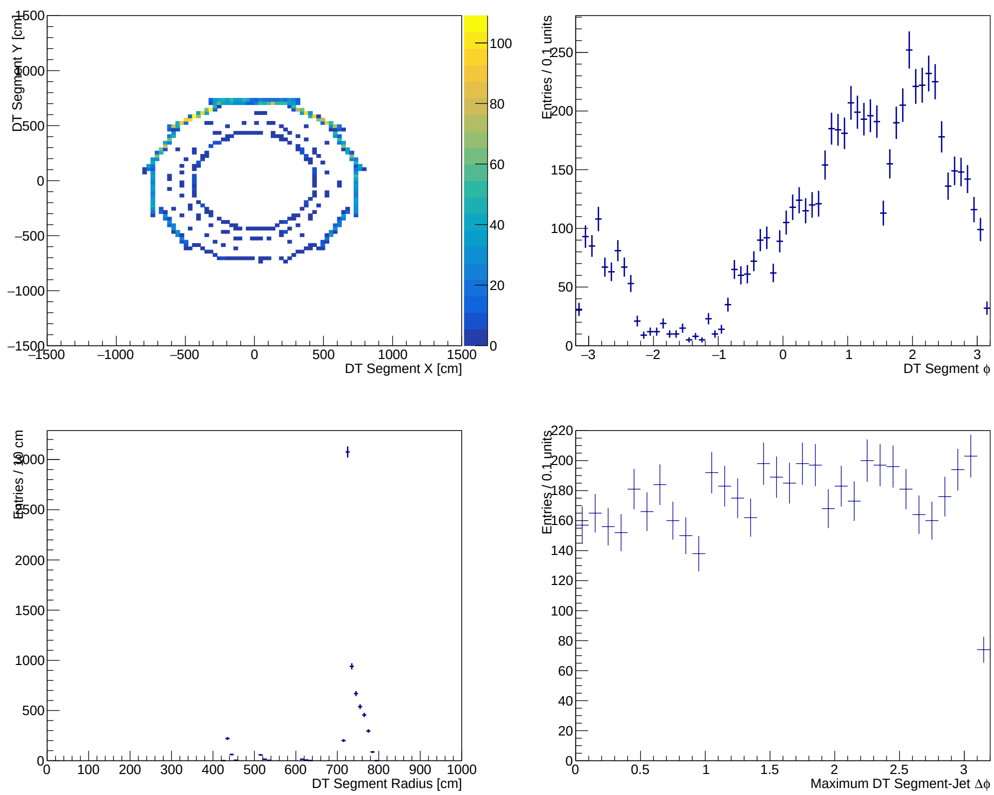

Figure 4.10: X-Y, R, ϕ and max$\Delta\phi$(DT, leading jet) of DT segments from HCAL noise events selected from 2016 collision run data. The even distribution in $\Delta\phi$ indicates that these HCAL deposits just come from HCAL noise and these noise events are accompanied by one or two DT segments from cosmic muons.

The most striking difference between the signal events and cosmic ray events is that the cosmic ray events have a large number of segments and hits throughout the muon systems, while the signal events don't. It's true that signal events might have jets that are energetic enough to punch through the solenoid coils, entering the muon chambers and leaving hits there. Those hits can only be found at the inner stations ($r < 560$ cm, where r is the transverse distance to the collision point) in one hemisphere, and the hits are more close to the jets. Thus we can largely reduce the number of cosmic ray events by rejecting:

1. events having at least two reconstructed DT segments in the outermost DT station (station 4)

2. events having any reconstructed DT segment in the second outermost DT station (station 3)

3. events that have two opposite DT segments ($|\Delta\phi| > \frac{\pi}{2}$)

4. events that have reconstructed DT segments in the inner three sations (station 1 - station 4) that are relatively far from the jet ($|\Delta\phi| > 1$)

5. events that have close RPC hits pairs from different stations ($\Delta R = \sqrt{(\Delta\phi)^2 + (\Delta\eta)^2} < 0.2$ and $\Delta r > 0.5$ m).

The capability of differentiating between signal events and cosmic ray muon events can be seen in Fig. 4.11.

The reason that we tolerate more DT segments in the outermost station (station 4), as we require that the accepted events should have less than 2 DT segments in station 4 but exactly 0 segments in the station 3, is that we have observed that

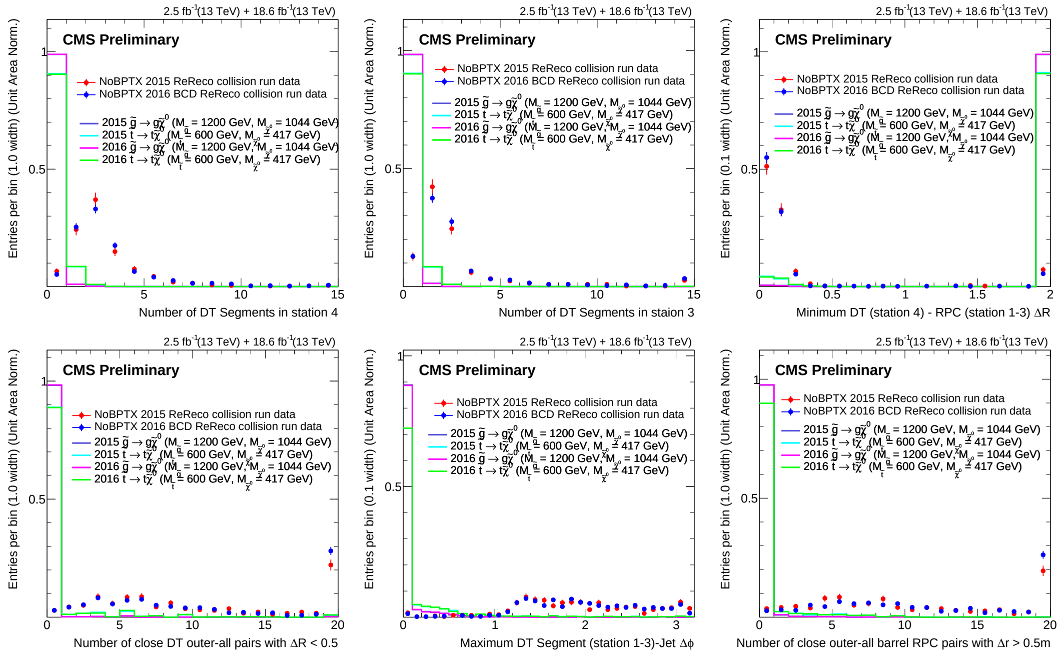

Figure 4.11: New and modified discriminating variables in the new cosmic veto for $m_{\tilde{g}} = 1200$ GeV and $m_{\tilde{\chi}^0} = 1044$ GeV; $m_{\tilde{t}} = 600$ GeV and $m_{\tilde{\chi}^0} = 417$ GeV; and 2015 and 2016 data (red and blue points) for events that pass all of the selection criteria except the cosmic veto. For MC simulation, the 2015 MC simulation was reconstructed in CMSSW_7_6_X, while the 2016 MC simulation was reconstructed in CMSSW_8_0_X. The histograms are normalized to unit area.

some of the non-cosmic events also tend to have one or two standalone DT segments. This effect could be seen in Fig. 4.10, where the RBX noise events are picked up for study. Since the positions of the DT segments does not depend on those of the jets, we confirm that the jets are from the HCAL noise and DT segments are just standalone objects that coincide the HCAL noise. The reason for these additional standalone DT segments is not very well understood, but thermal neutrons could be a possible explanation. Practically, when designing the selection criteria, we have to keep two things in mind, one is to loosen the constraint on the DTs from the outermost station so that we don't kill the signal, which could coincide with these additional DT segments. The second thing to keep in mind is, when calculating the signal efficiency, we should be aware of the possible scenario in which the signal could be rejected by the cosmic ray muon rejecting criteria in the presence of these additional DT segments, even though it would have been accepted without them. As we'll see in Chapter 4.6, we include additional terms in the signal efficiency due to this consideration.

To summarize, here are the selection criteria we use to reject the cosmic ray muon events:

1. $\mathrm{N_{DTSt4}} \leq 1$: we require that the number of DT segments in station 4 is less than 1

2. $\mathrm{N_{DTSt3}} = 0$: we require that the number of DT segments in station 3 is 0

3. $\mathrm{min\Delta R(DT_{St4}, RPC_{St1-3})} > 0.5$: we require that the minimum $\Delta\phi$ between DT pairs (one of them is in station 4, while the other is in station 1-3) is greater than 0.5

4. $\mathrm{N_{DTPair}} = 0$: we require that the number of opposite DT segment pairs is 0

5. $\mathrm{max\Delta\phi(DT_{St1-3}, leadingJet)} < 1$: we require that the maximal $\Delta\phi$ between the leading jet and DT segments from barrel station 1-3 to be less than 1.

6. $\mathrm{max\Delta\phi(DT_i, DT_j)} < \frac{\pi}{2}$: we require than the maximal $\Delta\phi$ between any two DT segments is less than $\frac{\pi}{2}$.

7. $\mathrm{N_{candidateOuter-AllBarrelRPCPair}} = 0$: we require that there is no RPC hits pairs from different stations ($\Delta R = \sqrt{(\Delta\phi)^2 + (\Delta\eta)^2} < 0.2$ and $\Delta r > 0.5$ m)

4.5.2 Halo Muon Rejecting Criteria

Beam halo muon travels close to the beam pipe, and it is likely to leave reconstructed CSC segments in the muon endcaps on both sides. Although CMS has implemented its own beam halo filter, we require even more strict criteria to achieve a better sensitivity by rejecting events based on the number of CSC segments. Since it's very rare for a signal to have reconstructed CSC segments, while most of the halo muons should induce at least one CSC segment, rejecting any events that have at least one CSC segment is a simple but highly effective criterion.

There is one more concern, which is based on a similar situation we have when designing the cosmic ray muon rejecting criteria. We have observed that some HCAL noise events tend to have standalone CSC segments, as shown in Fig. 4.12. These CSC segments usually have 3 or 4 hits close to the beam pipe, which suggests that they come from the slow thermal neutrons. Based on these features, we reject events with any reconstructed CSC segments having 5 hits or more.

As we did for the cosmic ray muon rejecting criteria, we introduce another term in the signal efficiency to account for the possibility that a good signal candidate could be killed by this rejecting criteria if it coincides with any CSC segments having 5 or more hits from a thermal neutron.

4.5.3 HCAL Noise Rejecting Criteria

The random electronic noise in the HCAL could give rise to spurious energy deposits that can be reconstructed as a jet that could be mistaken as the signal. However, there's a difference in the timing response in the HCAL readout between a physical jet and an HCAL noise jet. Analog signal pulses are read out over 10BXs

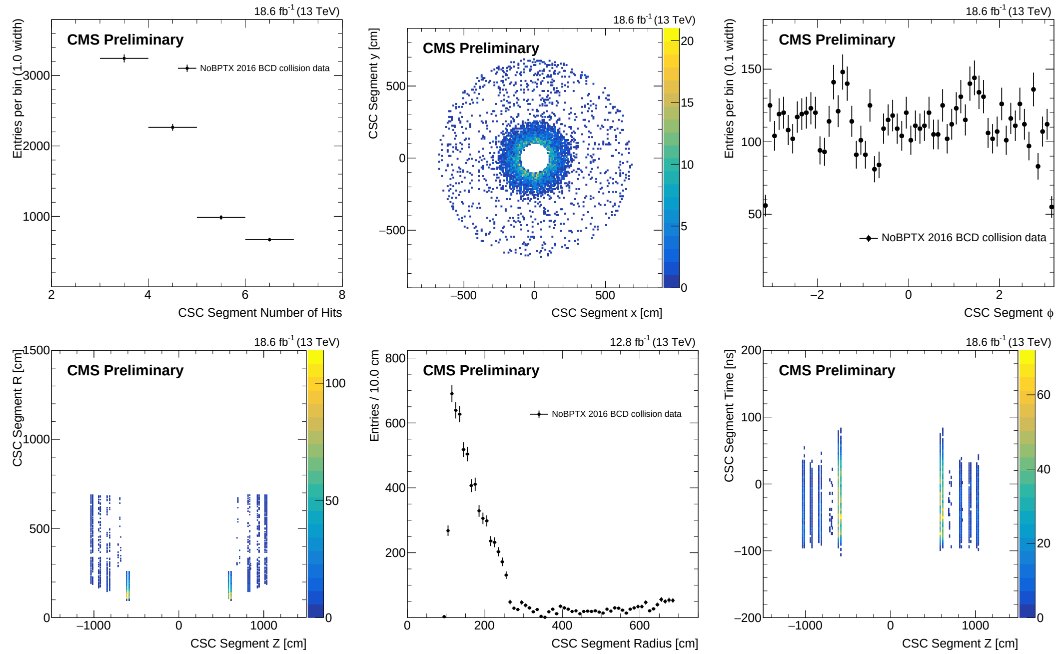

Figure 4.12: Distribution of CSC segments in NHits, X-Y, ϕ, Z-R, R, Z-T from events that pass the HLT, BX veto, vertex veto, jet Eta cut, have only one CSC segment and the CSC segment is not close to leading jet($\Delta\phi \geq 0.4$), have no DT segment.

and center at the maximum of the pulse shape. The timing pulse shape of a physical jet has a peak at the collision BX and exhibits an exponential decay over the subsequent BXs, while the pulse shape in an HCAL noise event is much more irregular: while some of them have readouts only in the peak BX, others may have readouts averagely distributed over 10 BXs. Another difference in the readout stems from the spatial distributions of the calo towers that are reconstructed from the HCAL hits. In case of the physical jets, the calo towers are clustered together. While this is also true for some of the HCAL noise, many of them show different topologies, such as having readouts only in ten or more contiguous HCAL towers at the same ϕ, or having readouts in almost all of the HCAL calo towers included in the same RBX.

To rejecting HCAL noise events, we apply the CMS HCAL noise filter at first, following by a series of dedicated criteria based on the spatial distribution of the HCAL towers and the timing pulse shape of the RBX readout.

To summarize, here are the HCAL noise rejecting criteria that we use in the 2015 search.

1. HCAL noise filter: We require that the events pass the standard CMS HBHE noise filter, which incorporates filters in the HPDs and a rechit R45 filter .

2. $n90_{jet} > 3$: We require that 90% of the leading jet energy is contained in more than three HCAL towers.

3. nTowiPhi < 5: We require that the jet consists of less than five HCAL towers at the same iPhi.

4. $E_{iphi}/E_{jet} < 0.95$: We require that less than 95% of the jet energy is deposited in HCAL towers at the same iPhi.

5. $R_1 > 0.15$, where $R_1 = E_{peak+1}/E_{peak}$: We require that the ratio (R_1) of the energy in one BX after the peak (E_{peak+1}) to the energy in the BX corresponding to the peak energy (E_{peak}) is greater than 0.15.

6. $R_2 > 0.1$, where $R_2 = E_{peak+2}/E_{peak+1}$: We require that the ratio (R_2) of the energy in two BXes after the peak (E_{peak+2}) to the energy in one BX after the peak (E_{peak+1}) is greater than 0.1.

7. $2 <$ Peak sample < 6, where peak sample is the BX where the energy is at its peak: We require that the peak BX is less than 6 and more than 2.

8. $0.3 < R_{peak} < 0.7$, where $R_{peak} = E_{peak}/E_{total}$: We require that the fraction of the energy in the peak BX (E_{peak}) out of the total energy (E_{total}) is between 0.3 and 0.7.

9. $R_{outer} < 0.3$, where $R_{outer} = 1 - [E_{peak-1} + E_{peak} + E_{peak+1} + E_{peak+2}]/E_{total}$: We require that the fraction of energy out of the four central BXes is less than 0.3.

The "nTowiPhi" selection criterion targets a particular variety of HCAL noise in which a particular HPD misfires on most or all 18 channels.

For the final five selection criteria, we consider the shape of the pulse in the HCAL electronics (more specifically, we look at the temporal distribution of big5Charge from the HPD with the maximum number of charge in the event).

The timing HCAL pulse shape of the signal is characterized by a relatively fast increase of the amplitude in the beginning, followed by an exponential decrease. While assuming BX_{peak} to be the BX that has the largest amplitude, we expect that there is still a significant amount of energy in the previous bunch crossing, which is defined as BX_{peak-1}. Also, BX_{peak+1} and BX_{peak+2} should contain a nontrivial amount of energy. We have designed a series of highly discriminating variables based on these pulses, which we expect to be correlated. The energy ratios, R_1 and R_2, are used to characterize the exponential decrease. R_{peak} represents the proportion of energy contained in the peak BX, and R_{outer} is the proportion of energy contained in the noncentral BXs, which is expected to be small.

In the 2016 analysis, we add a more strict selection criterion to exclude RBX noise in the HCAL. We require that maxiEtaDiffSameRbx, which represents the maximum difference in ieta between two reconstructed calo towers (hadEt > 0.2 GeV) in the same RBX where calo tower with largest hadEt is located, is smaller than

11. The distribution of this discriminating variable from different samples is shown in Fig 4.13.

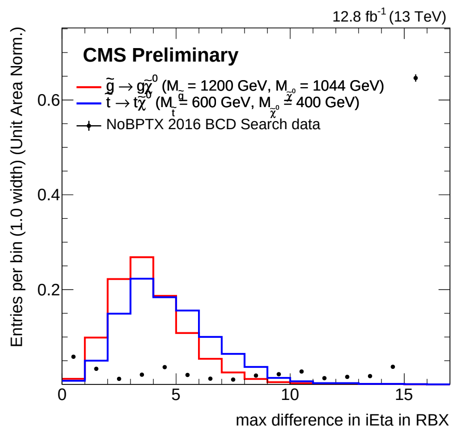

Figure 4.13: MaxiEtaDiffSameRbx for $m_{\tilde{g}} = 1200$ GeV and $m_{\tilde{\chi}^0} = 1044$ GeV; $m_{\tilde{t}} = 600$ GeV and $m_{\tilde{\chi}^0} = 400$ GeV; and 2016 data for events that pass all of the selection criteria except the noise veto and noise timing selection criteria. The signals are 2016 MC simulation that was reconstructed in CMSSW_8_0_X. The histograms are normalized to unit area.

In conclusion, in 2016 we add the following criterion to the noise rejection criteria we used in 2015:

1. maxiEtaDiffSameRBX < 11 : We require that maxiEtaDiffSameRbx, which represents the maximum difference in ieta between two reconstructed calo towers ($hadE_t > 0.2$ GeV) in the same RBX where the calo tower with largest hadEt is located, is smaller than 11.

Table 4.6: Summary of the values of $\varepsilon_{\text{stopping}}$, $\varepsilon_{\text{CSCveto}}$, $\varepsilon_{\text{DTveto}}$, and the plateau value of $\varepsilon_{\text{reco}}$ for different signals, for the 2016 calorimeter search. The efficiency $\varepsilon_{\text{stopping}}$ is constant for the range of signal masses considered. The efficiency $\varepsilon_{\text{reco}}$ is given on the E_g or E_t plateau for each signal.

	$\tilde{g} \to g\tilde{\chi}^0$	$\tilde{g} \to q\bar{q}\tilde{\chi}^0$	$\tilde{t} \to t\tilde{\chi}^0$
$\varepsilon_{\text{stopping}}$	0.054	0.054	0.045
$\varepsilon_{\text{reco}}$	0.533	0.566	0.399
$\varepsilon_{\text{CSCveto}}$	0.944	0.944	0.944
$\varepsilon_{\text{DTveto}}$	0.877	0.877	0.877
$\varepsilon_{\text{signal}}$	0.023	0.025	0.014

4.6 Signal Efficiency

In this search, we define the signal efficiency to be the probability of a signal passing all our selection criteria and being observed, after the R-hadrons are pair produced. More specifically, we define the $\varepsilon_{\text{signal}}$ to be the product of $\varepsilon_{\text{stopping}}$, $\varepsilon_{\text{reco}}$, $\varepsilon_{\text{CSCveto}}$ and $\varepsilon_{\text{DTveto}}$. The $\varepsilon_{\text{stopping}}$ has already been discussed in Chapter 4.4.1. In this section, we'll talk about the last three of these efficiencies. Here we assume that the decay always happens when our trigger is live and the branching fraction of the decay channel is 100%. Actually, this assumption is not true because our trigger will not be live if the decay coincides with any pp collisions. The probability that a decay takes place when the trigger is live is addressed in Chapter 4.9.1. The signal efficiencies used in the 2015 and 2016 searches are shown in Table 4.6 and Table 4.7.

4.6.1 ε_{reco}

The reconstruction efficiency is defined as the number of signal events that stop within the barrel region of the calorimeter and pass all our selection criteria (including

Table 4.7: Summary of the values of $\varepsilon_{\text{stopping}}$, $\varepsilon_{\text{CSCveto}}$, $\varepsilon_{\text{DTveto}}$, and the plateau value of $\varepsilon_{\text{reco}}$ for different signals, for the 2015 calorimeter search. The efficiency $\varepsilon_{\text{stopping}}$ is constant for the range of signal masses considered. The efficiency $\varepsilon_{\text{reco}}$ is given on the E_g or E_t plateau for each signal.

	$\tilde{g} \to g\tilde{\chi}^0$	$\tilde{g} \to q\bar{q}\tilde{\chi}^0$	$\tilde{t} \to t\tilde{\chi}^0$
$\varepsilon_{\text{stopping}}$	0.054	0.054	0.045
$\varepsilon_{\text{reco}}$	0.472	0.501	0.355
$\varepsilon_{\text{CSCveto}}$	0.980	0.980	0.980
$\varepsilon_{\text{DTveto}}$	0.977	0.977	0.977
$\varepsilon_{\text{signal}}$	0.024	0.026	0.015

the trigger requirement) divided by the number of signal events that stop within the calorimeter's barrel region. To the lowest order, ε_{reco} depends only on the energy of the visible daughter particles of the R-hadron decay, $E_g(E_t)$, or the mass difference between the gluino and the neutralino $(m_{\tilde{g}} - n_{\tilde{\chi}^0})$. We can measure the E_{reco} by applying our selection criteria (the trigger and offline selection criteria) on to Stage 2 signal MC simulation samples, which are produced with a range of $m_{\tilde{g}}(m_{\tilde{t}})$ and $m_{\tilde{\chi}^0}$.

Figure 4.14 shows ϵ_{reco} of the Stage 2 signal samples with the specified $m_{\tilde{g}}(m_{\tilde{t}})$ and $E_g(E_t)$ or $m_{\tilde{g}} - n_{\tilde{\chi}^0}$. It is also shown that above a gradual turn-on curve, ϵ_{reco} is approximately constant. This plot is used to determine the lowest allowed value of the daughter particle energy or the energy difference above which ϵ_{reco} becomes approximately constant, as well as the value of ϵ_{reco} above the lowest allowed value. These values are useful for the interpretation of the results from the counting experiment, as shown in Chapter 4.9. We are able to estimate them by fitting the ϵ_{reco} distribution to the error function $Erf(x)$.

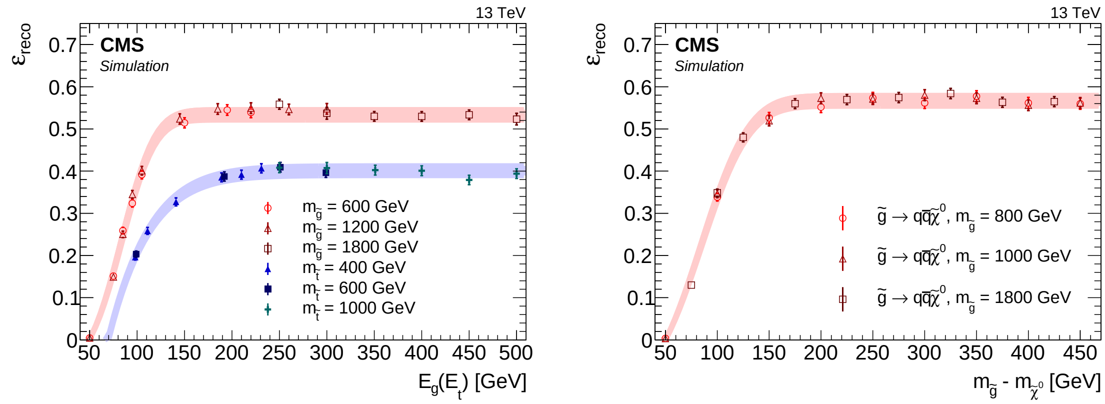

Figure 4.14: The $\varepsilon_{\text{reco}}$ values as a function of E_g or E_t (left), and $m_{\tilde{g}} - m_{\tilde{\chi}^0}$ (right), for $\tilde{g}$ and $\tilde{t}$ R-hadrons that stop in the EB or HB, in the MC simulation, for the calorimeter search. The $\varepsilon_{\text{reco}}$ values are plotted for the two-body gluino and top squark decays (left) and for the three-body gluino decay (right). The shaded bands correspond to the systematic uncertainties.

$$\text{erf}(x) = \frac{2}{\sqrt{\pi}} \int_0^x e^{-t^2} dt \tag{4.1}$$

A, B, C and D are the four parameters we are going to fit:

$$\epsilon_{reco}(E_g) = \text{A}\,\text{erf}(\text{B}E_g - \text{C}) + \text{D} \tag{4.2}$$

The central estimate of ϵ_{reco} is calculated as the fitted value on the plateau of the fitted curve.

The systematic uncertainty of ϵ_{reco} is calculated as:

$$\delta_{\epsilon_{reco}} = \text{Maximum}\left(\frac{\text{Abs}(\epsilon_{reco}(E_g)_i - \epsilon_{reco})}{\epsilon_{reco}}\right) \tag{4.3}$$

where i includes the E_{gluon} values on the plateau.

For the 2015 MC simulation, we have $\epsilon_{reco} = 47.2\%$ for gluinos and $\delta_{\epsilon_{reco}} = 7.7\%$ when $E_g > 130$ GeV. For three body gluino decays with $m_{\tilde{g}} - m_{\tilde{\chi}^0} \gtrsim 160$ GeV , the values are $\epsilon_{reco} = 50.1\%$ and $\delta_{\epsilon_{reco}} = 7.7\%$. And for stops with $E_t > 170$ GeV, the values are $\epsilon_{reco} = 35.5\%$ and $\delta_{\epsilon_{reco}} = 5.2\%$.

And for the 2016 MC simulation, we have $\epsilon_{reco} = 53.3\%$ for gluinos and $\delta_{\epsilon_{reco}} = 7.5\%$ when $E_g > 130$ GeV. For three body gluino decays with $m_{\tilde{g}} - m_{\tilde{\chi}^0} \gtrsim 160$ GeV , the values are $\epsilon_{reco} = 56.6\%$ and $\delta_{\epsilon_{reco}} = 7.5\%$. And for stops with $E_t > 170$ GeV, the values are $\epsilon_{reco} = 39.9\%$ and $\delta_{\epsilon_{reco}} = 5.2\%$. The difference between the 2015 and 2016 MC simulation reconstruction efficiency is due to the removal of the beam halo filter in our trigger in 2016.

4.6.2 $\varepsilon_{\mathrm{CSCveto}}$

The $\varepsilon_{\mathrm{CSCveto}}$ is defined as the probability that a stopped signal passing the full offline selection criteria could still pass the halo rejection criteria if the effect of thermal neutrons is considered, (The decay of thermal neutrons could lead to additional reconstructed CSC segments in the muon endcaps. These CSC segments are not modeled in the simulation and could make a potentially observed signal be rejected by the halo rejection criteria.). Since ideally there are no CSC segments in a noise event, noise events are good candidates to study the $\varepsilon_{\mathrm{CSCveto}}$, which can be determined by simply counting how many events in a noise sample fail the halo veto. As an example, Table 4.8 shows that out of 66700 noise events among the full 2016 collision run data, 63425 events pass the halo veto. Also considering that the second to last criterion already rejected events having CSC segments close to the leading jet, the last criterion only deals with CSC segments within an effective angle of 2π-0.8. Thus the full $\varepsilon_{\mathrm{CSCveto}}$ can be calculated as $1 - \frac{66700-63425}{66700} \times (\frac{2\pi}{2\pi-0.8}) \sim 94.4\%$.

The systematic uncertainty in $\varepsilon_{\mathrm{CSCveto}}$ can be calculated by applying another set of selection criteria to pick the noise events from the sample, and by recalculating the $\varepsilon_{\mathrm{CSCveto}}$. We then define the systematic uncertainty as the relative difference between this newly calculated $\varepsilon_{\mathrm{CSCveto}}$ and the value obtained previously. Table 4.9 shows the cutflow of calculating the new value of $\varepsilon_{\mathrm{CSCveto}}$. Following the same procedure, we calculate that the $\varepsilon_{\mathrm{CSCveto}}$ is 94.6%. Thus the systematic uncertainty in $\varepsilon_{\mathrm{CSCveto}}$ is just $\frac{0.946-0.944}{0.944} = 0.2\%$.

In terms of the 2015 search data, the $\varepsilon_{\mathrm{CSCveto}}$ is 98.0% if we apply the R2 and N90 cuts in our event selection. If we apply the R_{peak} and JetEFraction criteria, then $\varepsilon_{\mathrm{CSCveto}}$ is 97.9%. Thus the relative systematic uncertainty is just 0.1%.

Table 4.8: Event selections used to calculate $\varepsilon_{\mathrm{CSCveto}}$. The events before last cut are mostly noise events due to the R2 and N90 cuts applied. The last cut, new halo veto, is applied to calculate how much of noise events could escape it.

$L = 36.7\,\mathrm{fb}^{-1}$	Event yield
	NoBPTX 2016 full collision run data
total	3838714
trigger	3217983
BX veto	3047840
Vertex veto	3037376
$R_2 < 0.075$	675063
$\eta_{jet} < 1.0$	131755
$\mathrm{n90}_{jet} < 2$	67195
No CSC segments(nHits > 4) close to leading to jet($\Delta\phi < 0.4$)	66700
new halo veto	63425

Table 4.9: Event selections used to calculate the systematic uncertainty of $\varepsilon_{\mathrm{CSCveto}}$. The events before last cut are mostly noise events due to the R_{peak} and E_{iphi}/E_{jet} cuts applied. The last cut, new halo veto, is applied to calculate how much of noise events could escape it.

$\mathrm{L} = 36.7\,\mathrm{fb}^{-1}$	Event yield
	NoBPTX 2016 full collision run data
total	3838714
trigger	3217983
BX veto	3047840
Vertex veto	3037376
$R_{Peak} > 0.8$	815199
$\eta_{jet} < 1.0$	129146
$E_{iphi}/E_{jet} \geq 0.95$	120418
No CSC segments(nHits > 4) close to leading to jet($\Delta\phi < 0.4$)	119546
new halo veto	113862

4.6.3 $\varepsilon_{\mathrm{DTveto}}$

Similar to what we did in the $\varepsilon_{\mathrm{CSCveto}}$ case, we use $\varepsilon_{\mathrm{DTveto}}$ to quantify the probability that a signal event that should have passed the cosmic veto could still pass the veto, if potential accompanying DT segments are considered (such as those induced by thermal neutrons).

The strategy we used to calculate the $\varepsilon_{\mathrm{DTveto}}$ is exactly the same as we used when deriving $\varepsilon_{\mathrm{CSCveto}}$. We use the R2 and N90 criteria to pick up noise events and instead of applying the halo veto in the end, we apply the cosmic veto.

We also use the R_{peak} and E_{jet} fraction cut to study the systematic uncertainty in $\varepsilon_{\mathrm{CSCveto}}$, which turns out to be $\sim 0.1\%$.

4.7 Backgrounds

Here we describe the methodologies we used to estimate the three major backgrounds.

4.7.1 Cosmic Ray Muons

To estimate how likely a cosmic ray muon will traverse the detector yet escaping the cosmic ray muon rejection criteria, we produce a private Monte Carlo sample of 60 million cosmic ray muon events using CmsGen [58], which is based on the air shower program Corsika [59]. We further require the cosmic ray MC events to have a missing energy of 15 GeV and at least one barrel jet, as well as no reconstructed CSC segments in the event so that the event won't be rejected by the beam halo rejecting criteria. By applying these requirements, we are left with a sample of 54k events, which is large enough to get a valid statistical result. These 54k events are very similar to the real cosmic ray events we observe in the detector.

We are then interested in how many of cosmic ray events would escape the cosmic ray rejecting criteria. Using the 54k sample of MC cosmic ray muons, we are able to estimate this rate by counting how many cosmic ray muons are able to escape all our cosmic rejection criteria. Before actually doing the calculation, there is one thing worth checking: Since our cosmic ray muon rejecting criteria is based on DT segments and RPC hits, the inefficiency of the rejecting criteria is dependent on the actual number of DT segments and RPC hits in the events. Figure 4.15 shows the distribution of the number of segments and hits between cosmic events in the collision run data and the simulated cosmic events. The difference is small enough to validate our simulation, but the simulated events tend to have less DT segments and more RPC hits.

To account for this small difference, we bin the simulated cosmic ray muon events in terms of the number of DT segments and outer barrel RPC hits.

Then the inefficiency histogram is obtained by dividing the histogram only including cosmic MC events that escape the cosmic rejection criteria by the histogram containing all 54k simulated cosmic events. These histograms are shown in Fig. 4.16.

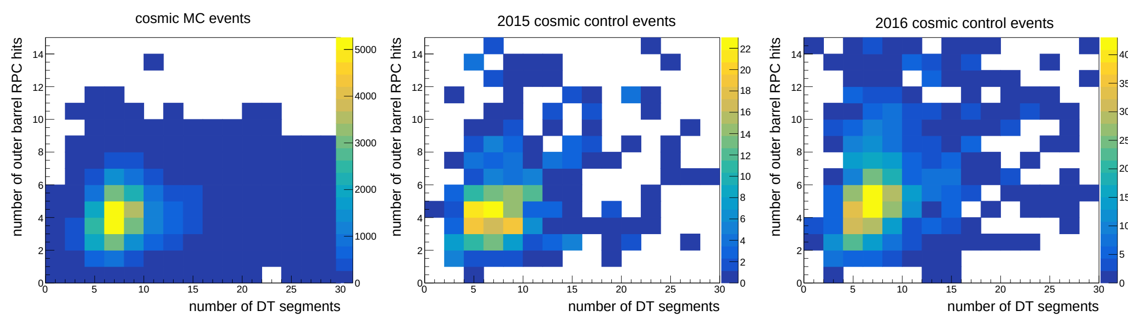

Figure 4.15: A comparison between cosmic MC simulation (left), cosmic control events from the 2015 dataset (middle), and cosmic control events from the 2016 dataset (right).

Another histogram necessary for the background estimate is the distribution of cosmic events selected from the data, binned in the number of DT and outer barrel RPC hits. These cosmic events are vetoed by cosmic rejection criteria but pass all other offline selection criteria, and they must also have at least one DT segment so that halo or noise events are not included. Due to low statistics and high veto inefficiency in the lower left bins with $n_{\mathrm{DT}} < 2$ and $n_{\mathrm{outerBarrelRPC}} < 6$, the numbers of cosmic events in those bins are extrapolated from neighboring bins with abundant

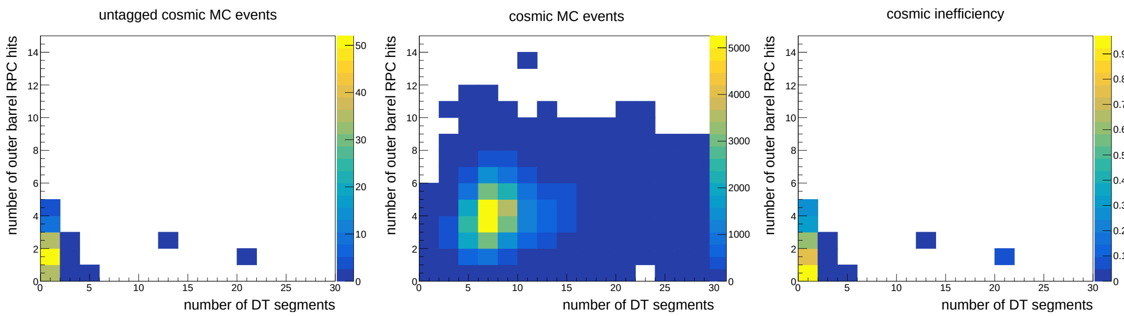

Figure 4.16: The calculation of cosmic inefficiency is done in each bin to account for the difference between the simulation and data

cosmic events($2 \leq \mathrm{n_{DT}} < 4$). The scaling factor can be derived from the cosmic MC sample, and the number of cosmic events in the bins with low statistics can be calculated using $\mathrm{N_{cosmicdata}} = \frac{\mathrm{N_{cosmicdataref}} \times \mathrm{N_{MC}}}{\mathrm{N_{MCref}}}$, where "ref" means the sum of numbers in bins with $2 \leq n_{DT} < 4$, and $\mathrm{N_{cosmicdata}}$ along with $\mathrm{N_{MC}}$ refer to the same bin within the region of low statistics. We then set the value of any empty bins as the average value of its left and right neighbors. The final smeared histogram is shown on the left plot of Fig. 4.17.

Finally, the cosmic background estimate is obtained by multiplying the inefficiency histogram by the histogram of cosmic data events, which pass all selection criteria except the cosmic rejection one, as shown in Fig. 4.17. We then sum up the bin values in the resulting histogram to get the cosmic background estimate of 2.6 ± 0.4 events for the 2015 analysis, and 8.8 ± 1.3 events for the 2016 analysis.

Cosmic events will pass the cosmic rejection criteria if the muon travels through holes in the CMS detector (such as gaps between the muon barrel wheels). In the background calculation, we use cosmic MC simulation to figure out the ratio of events that will pass these holes. However, there could be fluctuations in the proportion of the muons passing through holes in the real data. To calculate the fluctuation on the occupancy, we define our own fiducial regions in the detector (where there is actually active material) and count how many cosmic muons could leave DT segments in this hole in both MC simulation and data, and treat the difference as the source of systematic uncertainty. Considering the fact that the fluctuation might be different throughout the detector, we measure this occupancy in several different places, where some of them are very close to the gap. More specifically, we measure the occupancy in six evenly separated regions between z = -120 cm to z = +120 cm, where the sizes are comparable to the size of gaps between the muon chambers. Since the region is relatively small, the full 2016 data is used in the calculation so that we have enough statistics.

Table 4.10 shows the event selections we used to study the difference in the occupancy. The preselection criteria, which include all the selection criteria except the last one, is used to pick up cosmic events from the data. The last criterion requires the events to have at least one DT segment in the upper and lower part of the fiducial regions respectively.

Table 4.11 shows the comparison of the occupancy of cosmic events in different fiducial regions between data and MC. We can see that although the differences vary from 12% to 50%, the discrepancies don't seem abnormal in the region close to the gap. We thus take the average of these discrepancies and define the results as our relative systematic uncertainty, which is 32%. Thus the systematic uncertainty in the cosmic background estimate is 2.8 events (0.8 events) in the 2016 (2015) search.

Table 4.10: Event selections for estimating the systematic uncertainty of the cosmic background estimate. The cuts before the last one are used to select cosmic events from the sample. The last cut is applied so that the cosmic muon leaves tracks in both upper and lower region of the specific fiducial region

$\mathrm{L} = 36.7\,\mathrm{fb}^{-1}$		Event yield
$-80cm \leq z < -40cm$	CosmicMC	2016 fulll ReReco search data
total	54716	3838710
trigger	54716	3838710
BX veto	54716	3609580
Vertex veto	54716	3598290
new halo veto	54716	1788950
HCAL noise veto	47954	731726
$E_{jet} > 70$ GeV	7188	143874
$N_{DT} > 4$	6564	12456
have DT segments in the fiducial region	17	37

Fiducial regions(cm)	2016 Full ReReco data	MC	|data – MC|/MC
$-120 \leq z < -80$	0.15%	0.11%	36%
$-80 \leq z < -40$	0.20%	0.17%	18%
$-40 \leq z < 0$	0.77%	1.22%	37%
$0 \leq z < 40$	2.07%	1.38%	50%
$40 \leq z < 80$	0.16%	0.26%	38%
$80 \leq z < 120$	0.19%	0.17%	12%

Combining all these details above, we predict a cosmic background of 2.6 $\pm$ 0.4 (stat.) $\pm$ 0.8 (syst.) events for the 2015 analysis, and that of 8.8 $\pm$ 1.3 (stat.) $\pm$ 2.8 (syst.) for the 2016 analysis.

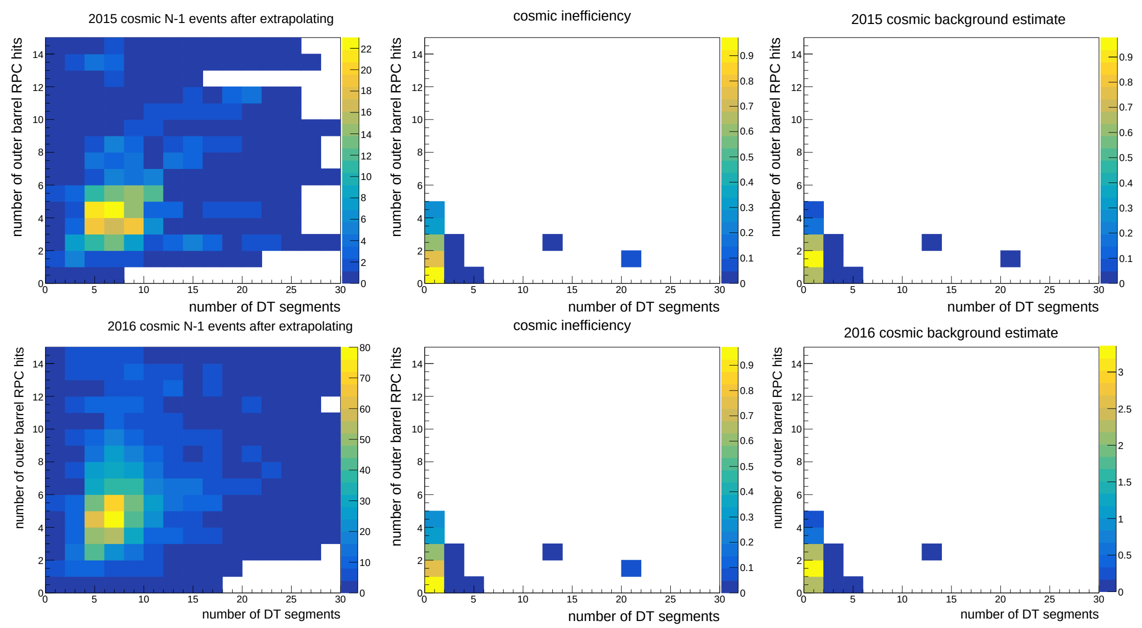

Figure 4.17: The cosmic background estimate (right) is determined by the cosmic ray events in the data (left), which pass all selection criteria except the cosmic rejection criteria, as well as the cosmic rejection inefficiency (middle)

4.7.2 Beam halo

Halo muons will escape the beam halo rejecting criteria if they pass through the uninstrumented area of the detector or the chambers that are powered off.

We estimate the beam halo background using a "tag-and-probe" method. This data-driven method assumes that the probability of beam halo muons escaping detection at one end of the muon endcap system is independent of its probability of escaping detection on the other end of the endcaps. For example, we can use the CSC segments on -z side of the muon endcaps to identify beam halo events, and then we can use these events to estimate how likely the beam halo misses the $+z$ side by dividing the number of events that have no CSC segments in the $+z$ endcap by the total number of events we tagged. Similarly, we can follow this method in a symmetric way to estimate the probability of a beam halo event escaping detection in the -z endcap. Since these two probabilities are independent of each other, the rate of the failure of the beam halo rejection criteria is just the product of these two probabilities.

Since we tag halo events based on the CSC segments and non-halo events could also have concurrent CSC segments due to the presence of thermal neutron, it would be good if we can differentiate between them. Figure 4.18 shows the difference in the distributions of CSC segments during collision data taking periods and cosmic data taking periods. It's obvious to see that CSC segments from halo muons are closer to the beam pipe with R $<$ 3.4 m and they are very close to the leading jet ($\Delta\phi < 0.4$). Thus in the estimation of beam halo background, we only consider CSC segments that satisfy the above two requirements. Also, the CSC segments should have at least 5 hits, as required in the beam halo rejecting criteria.

In our estimation, we required the tagged events to meet the following criteria:

1. Passes the signal trigger
2. Passes the BX and vertex veto
3. Has at least one reconstructed jet, $|\eta_{leadingjet}| < 1$
4. Has candidate CSC segments in at least two different CSC layers

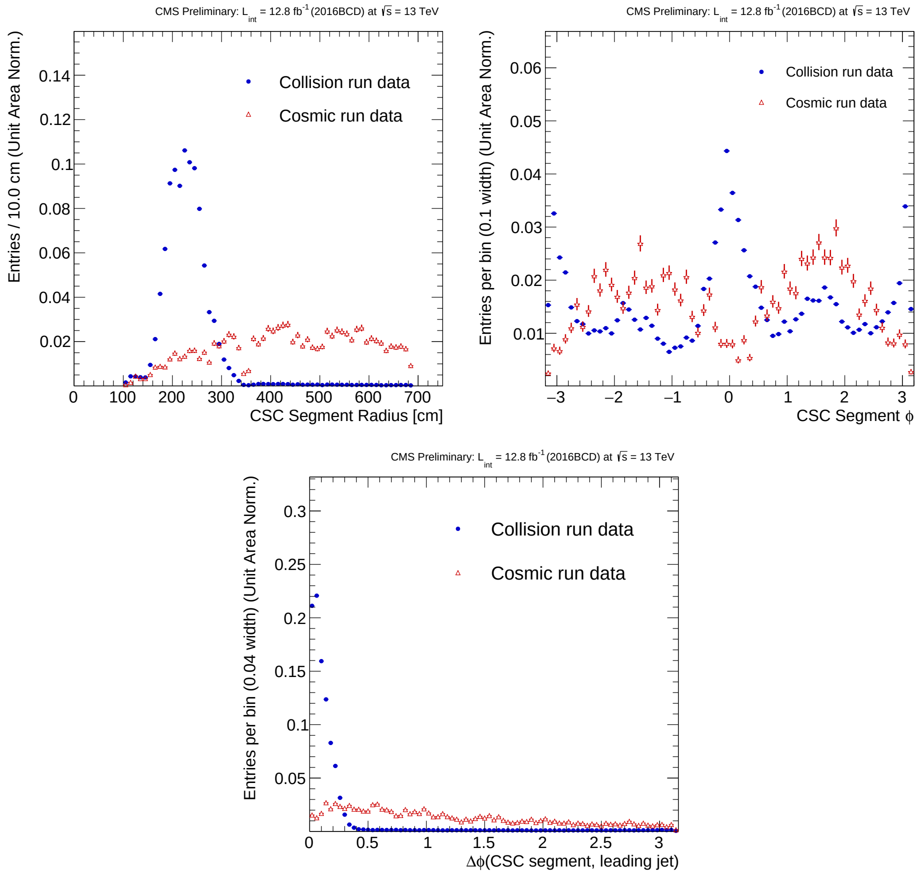

Figure 4.18: The comparison between collision run data and cosmic run data on the R, ϕ and $\Delta\phi(\text{leadingjet}, \text{CSCsegment})$ of CSC segments from events that pass HLT, BX veto, vertex veto, cosmic veto, noise veto and jet Eta cut. Most CSC segments are from beam halo, while the rest could be due to the cosmic muons or slow neutron radiation.

The traveling direction of the halo muons can be determined by the z-position and timing measurements. This allows us to separate halo events from each beam. Figure 4.19 shows distributions of the CSC segment position and time for halo muons in the 2016 data. There is much more halo in Beam 1 due to the physical properties of the LHC.

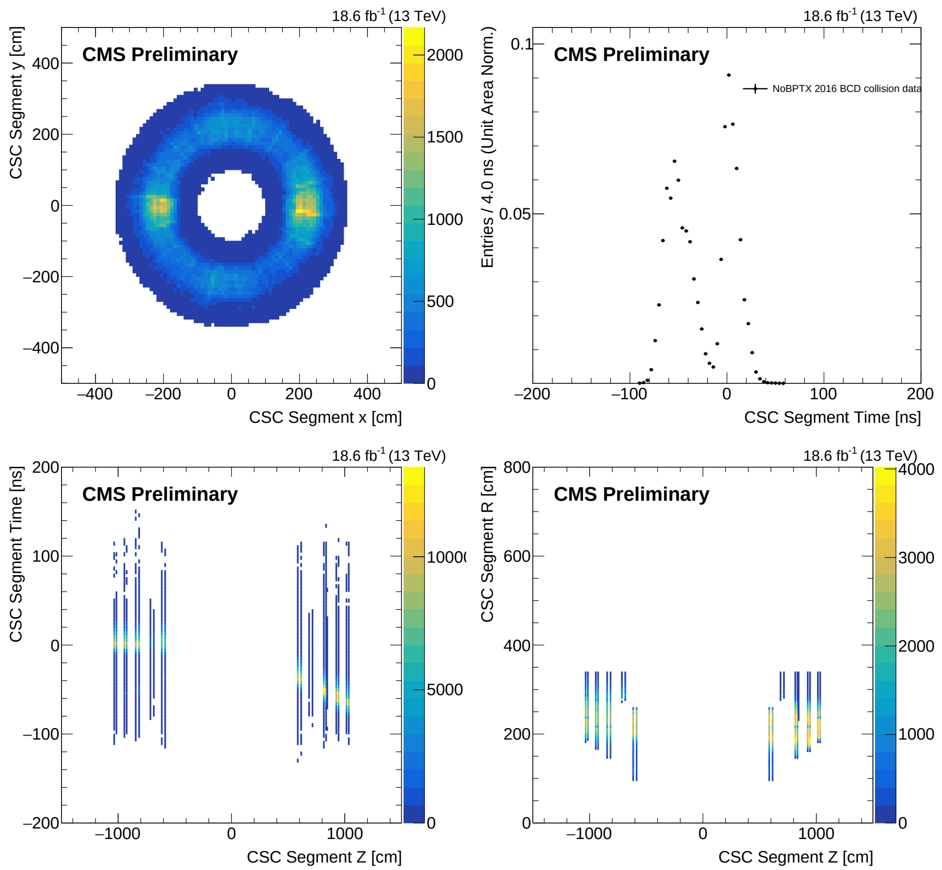

Figure 4.19: The scatter plot of the CSC segment y position as a function of the x position; the distribution of the CSC segment time; the scatter plot of the CSC segment time as a function of the z position; and the scatter plot of the CSC segment R as a function of the z position. Events should pass the signal trigger, BX veto, vertex veto, jet Eta cut, have one CSC segment close to leading jet($\Delta\phi < 0.4$) . The CSC segment time histogram is normalized to unit area, and the colors in the other two figures indicate the number of events in each bin.

For halo muons traveling in the same direction (Beam 1 or Beam 2), we further categorize the events into "IncomingOnly", "OutgoingOnly" and "Both", depending on whether the muon leaves tracks in one or both of the endcap muon detectors.

It may happens that a halo muon only has an incoming leg or outgoing leg or even has neither of them, due to the timing effect or that the muon traverses the inactive regions in the muon systems.

Our tag and probe method then implies that the probability of a muon not having an outgoing track is $\frac{\text{IncomingOnly}}{\text{IncomingOnly+Both}}$ and the probability of a muon not having an incoming track is $\frac{\text{OutgoingOnly}}{\text{OutgoingOnly+Both}}$. Then the probability of a muon to leave no segments is :

$$\frac{\text{IncomingOnly}}{\text{IncomingOnly+Both}} \times \frac{\text{OutgoingOnly}}{\text{OutgoingOnly+Both}} \sim \frac{\text{IncomingOnly} \times \text{OutgoingOnly}}{\text{Both} \times \text{All}} \tag{4.4}$$

In the next step, we histogram the events according to their categories, binning the events based on the average (x,y) position of all candidate CSC segments in the event. We can calculate the chance for a halo muon to pass by the detector without leaving incoming and outgoing tracks as $\frac{\text{IncomingOnly}\times\text{OutgoingOnly}}{\text{Both}\times\text{All}}$ for both Beam 1 and Beam 2 halo muons. (Since we have much fewer Beam2 halo muons than Beam 1 halo muons, we calculate the Beam 2 background directly without binning if we have very low statistics in a specific dataset.) Since the number of the halo muons that escape detection in both endcaps is expected to be extremely low, "All" is approximated by the sum of the other three categories. We then multiply this resulting histogram of inefficiency by the histogram including events that pass all other selection criteria and are positively identified as beam halo muons (see Fig. 4.20 and Fig. 4.21). By integrating over the resulting histogram and summing the results for Beam 1 and Beam 2, we get our final background estimate of 1.10 ± 0.09 events for the 2015 analysis and 2.6 ± 0.1 for the 2016 analysis.

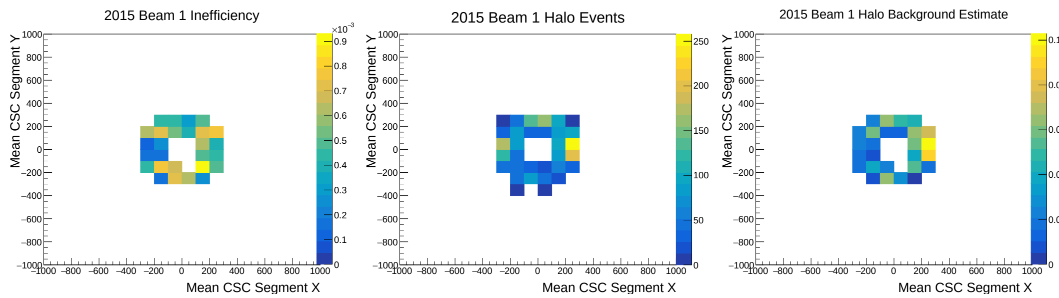

Figure 4.20: 2015 Halo background estimate: The scatter plot of the mean CSC segment y position as a function of the mean CSC segment x position for the data-driven estimate of the halo veto inefficiency (left), the halo events identified in the search sample that pass all other selection criteria except the halo rejection criteria (middle), and the resulting halo background estimate (right), separated by each beam. The colors indicate the number of events in each bin. Due to low statistics, halo background from beam 2 is calculated directly without binning

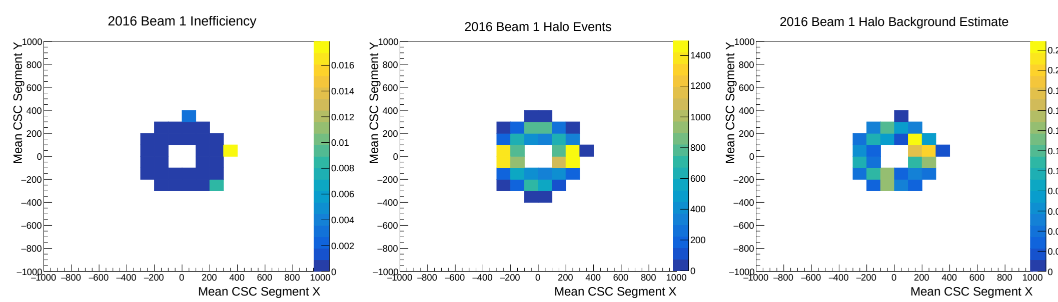

Figure 4.21: 2016 Halo background estimate: The scatter plot of the mean CSC segment y position as a function of the mean CSC segment x position for the data-driven estimate of the halo veto inefficiency (left), the halo events identified in the search sample that pass all other selection criteria except the halo rejection criteria (middle), and the resulting halo background estimate (right), separated by each beam. The colors indicate the number of events in each bin. Due to low statistics, halo background from beam 2 is calculated directly without binning

The systematic error could arise if the binning scheme is not properly consistent to the shape of the inactive material. To estimate this uncertainty, we repeat the same process as we previously did, but binning events in terms of the average (r, ϕ). The systematic uncertainty is the difference of the central values obtained from the two binning scenarios. The final estimate thus becomes 1.10 ± 0.09 (stat.) $\pm\, 0.06$ (syst.) for the 2015 analysis, and 2.6 ± 0.1 (stat.) $\pm\, 0.1$ (syst.) for the 2016 analysis.

4.7.3 HCAL noise

The background of instrumental noise is estimated by considering data taken during cosmic data taking periods in 2015 and 2016 (i.e., the control sample), which are believed to only include cosmic events and instrumental noise in the HCAL.

In 2015, we observe 2 events after applying the selection criteria on the control sample. Since the cosmic background estimate is 1.7 ± 0.6 events, we assume the central value of noise estimate is 0.3 events.

The statistical as well as the systematic error are calculated by performing a toy counting experiment using the number of observed events and the cosmic background estimate. Assuming that the cosmic background follows a Gaussian distribution centered at the background estimation, and the number of observed events follows a Poisson distribution whose mean value is the observed number of events, we can convolute these two distributions and get a 68% CL interval of the noise background estimate. Over 10000 samples, the toy counting experiment predicts an estimate of $0.3^{+2.4}_{-0.3}$ events at 68% CL level. This estimate is then scaled to the search data by assuming that the noise estimate is proportional to the number of noise events in the sample, resulting in an estimate of $0.4^{+2.9}_{-0.4}$ noise events in the 2015 search sample. The events in the noise control region are selected by applying the trigger, the BX veto, the vertex veto, the cosmic veto, the halo veto, jet energy and eta cut criteria, and the noise veto. The size of noise events in the 2015 search sample is 2314, while that in the control sample is 1901 events.

For noise events in the 2016 analysis, the distributions of the timing pulse shape discriminating variables such as R1 and R2 are different than we obtained in 2015, thus making 2016 cosmic runs a more appropriate noise control region. After applying some preselection criteria, the distributions in the 2016 control and search sample just mentioned agree with each other pretty well, as shown in Fig. 4.23. To decrease the amount of cosmic events in our control region, we designed a specific discriminating variable, nTowerDiffRbxDeltaR0p5, which counts the number of calo towers with hadEt > 0.2 GeV that are not only located within a distance of DeltaR $= 0.5$ from the calo tower with highest hadEt(leading calo tower), but also from an RBX other than the one containing the leading calo tower. A comparison in the distribution of nTowerDiffRbxDeltaR0p5 between noise events and cosmic events is shown in Fig 4.22. Thus a new criterion, nTowerDiffRbxDeltaR0p5 < 2, will help us reject many cosmic events while keeping most noise events. Since this variable only cares about the calo towers in RBXs adjacent to the leading tower, it is uncorrelated to the other noise discriminating variables, which are based on the information of the RBX containing the leading tower. So we can use the noise inefficiency we get in the control region directly in the search sample without applying this new criterion in the search sample.

We observed 2 events after applying the full analysis selection criteria as well as the nTowerDiffRbxDeltaR0p5 criterion, with a cosmic background estimate of 2.5 ± 0.9 events. A similar toy experiment is performed and results in a noise estimate of $0^{+2.2}_{-0}$ events. Considering that the size of noise control region in the 2016 cosmic

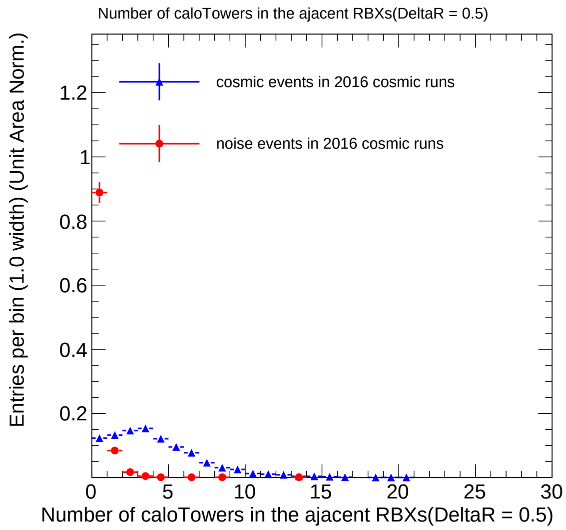

Figure 4.22: A comparison in distribution of nTowerDiffRbxDeltaR0p5 between cosmic and noise events. Both events should pass the trigger, the bx veto, the vertex veto, the halo veto, the jet energy cut, the jet eta cut. Moreover, the cosmic events should also pass jet N90 cut and have at least 4 reconstructed DT segments, while noise events should pass the cosmic veto and max ieta cut.

run data is 1725 events and that in the 2016 collision run data is 7676 events, we get a noise estimate of $0^{+9.8}_{-0}$ events by assuming that the noise inefficiency remains the same in both samples. The noise control region, in this case, contains events that pass the trigger, the BX veto, the vertex veto, the halo veto, the cosmic veto, the noise veto, the jet energy and ieta criteria and the maxiEtaDiffSameRBX criterion. The large noise uncertainty in the 2016 search sample is due to the limited number of noise events in the control sample.

The total background in 2015 and 2016 are shown in Table 4.15.

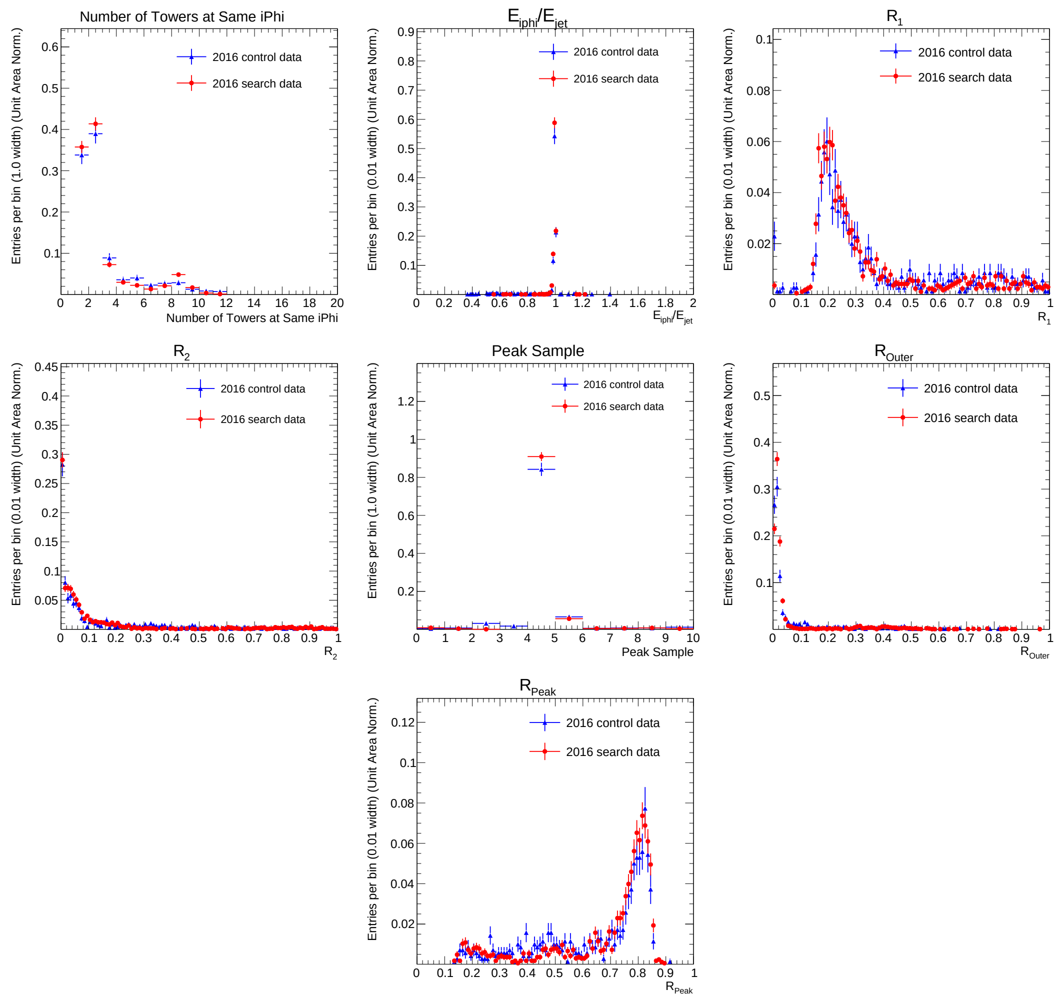

Figure 4.23: Comparison on noise events between 2016 search and 2016 control data, including events passing all cuts before jet N90.

4.8 Systematic Uncertainties

The systematic uncertainties in the signal yields are described here and summarized in Table 4.12.

The slight energy dependence in the reconstruction efficiency described in Chapter 4.6.1 results in a $\sim 7\%$ uncertainty.

We use two different sets of selection criteria to study the $\varepsilon_{CSCveto}$ and ε_{DTveto}, as shown in Chapter 4.6.2 and Chapter 4.6.3. The systematic uncertainties in both cases are within 0.2% and thus negligible.

The luminosity is estimated within 2.3% for the 2015 data [60] and within 2.5% for the 2016 data [61].

The Jet Energy Scale (JES) represents the difference between the true energy of the jets and their reconstructed energy. Although the JetMET group at CMS produces the estimates of the JES uncertainty, these estimates are calculated assuming that the origin of the jet is from the interaction point. This assumption does not hold in our search because the jets originate from decays of stopped particles, cosmic ray or beam halo muons, and thus cannot be aligned radially. It is not quite straightforward to determine the signal systematics related to the JES.

In the CMS Running At Four Tesla (CRAFT) era, the CMS HCAL group has performed a study in which they use cosmic ray events to validate the HB simulations in GEANT [62]. More specifically they have studied the absolute jet energy scale and the description of the material. This study provides us with useful information on how well the non-radial HCAL deposits are modeled in the simulation, as the cosmic ray muons in the study do not follow the radial direction as a typical collision jet or muon would. The study concludes that the difference in HCAL deposits left by muons with $p_T < 100$ GeV between simulation and the CRAFT data is within 2%. The study gives us an estimate of how accurate the HCAL simulation is for non-radial deposits.

Besides the CRAFT study, there is also a CMS note on the study of jet performance using di-jets and Z+jets events in 2012 [63]. Since the studied events contain the jets from the collisions, the result of the JES uncertainty does not apply directly to our search. However, we can still learn the relative difference between the MC simulation and data in terms of the absolute JES. The JES uncertainty is reported to be 1% for jets at $|\eta| < 1.0$. At $|\eta| < 2.8$, the uncertainty increases up to 5%. We can use these values to characterize the JES uncertainty of jets that strike the barrel calorimeter at various incident angles. The end of the HB corresponds to the maximum angle of incidence for a collision jet, which is 60 degrees from the normal. This study concludes that for the full η range corresponding to the HB, in which the angle of incidence varies from 0 to 60 degrees, the JES uncertainty is less than 2%. Thus, we assume that the uncertainty on JES is less than 3%. Although the value is somewhat conservative based on the results of this jets study, we do want to take into account the cases in which the jets from the signal, cosmic ray muons or beam halo muons strike the HB at extreme angles that are not available in these studies. By assuming the JES uncertainty to be 3%, we vary the jet energy in the simulation correspondingly to see the change of the signal efficiency. Our study shows that the signal efficiency varies by about 2 %.

Table 4.12: The systematic uncertainties in the 2015 and 2016 searches.

	2015 search data	2016 search data
Reconstruction Efficiency	7.7%	7.5%
Luminosity	2.3%	2.5%
JES	2.0%	2.0%

The systematic uncertainties on the background estimates were covered when each background estimate was described in Chapter 4.7. They are included in the uncertainties listed with the background estimates in Table 4.15.

4.9 Search Results

4.9.1 Toy Monte Carlo and Counting Experiments

Table 4.15 summarizes the backgrounds and observed events in the 2015 and 2016 searches. Detailed cutflow tables for the 2015 and 2016 search date and for different signals are shown in Table 4.13 and Table 4.14. Then, to interpret the search results for various small lifetime hypotheses, we perform a toy Monte Carlo simulations and counting experiments.

The rate of background events is approximately constant with time and the signal rate depends on the lifetime of the stopped LLPs. If the lifetime of LLPs is very small, it could happen that BXs far away from any collisions where signals have already decayed only include background events. To increase the sensitivity of our search, we perform counting experiments in equally spaced log time of gluino and stop lifetime hypotheses, from 10^{-7} to 10^{6} seconds. For each lifetime hypotheses, we pick a corresponding size of the search time window. For hypotheses of lifetime greater than one LHC orbit (89 μs), the search window sizes are all the same and fixed to be the total trigger livetime of the corresponding data taking period of the year, since it's likely to observe signal at any time. For hypotheses with lifetimes shorter than one LHC orbit, the search window is determined to be 1.3τ to maximize the sensitivity, since almost all of the signals have decayed beyond the search windows. Thus for these lifetimes, the background and the observed events are all dependent

Table 4.13: Cumulative number of events all selection criteria, for 2015 MC simulations of $m_{\tilde{g}} = 1200$ GeV and $m_{\tilde{\chi}^0} = 1044$ GeV, corresponding to $E_g = 145$ GeV, for $m_{\tilde{t}} = 600$ GeV and $m_{\tilde{\chi}^0} = 400$ GeV, corresponding to $E_t = 192$ GeV, for the 2015 search dataset.

$\mathrm{L} = 2.7\,\mathrm{fb}^{-1}$

	$\tilde{g} \rightarrow g\tilde{\chi}^0$ (2015 MC simulation) ($M_{\tilde{g}} = 1200$ GeV, $M_{\tilde{\chi}^0} = 1044$ GeV)	$\tilde{t} \rightarrow t\tilde{\chi}^0$ (2015 MC simulation) ($M_{\tilde{t}} = 600$ GeV, $M_{\tilde{\chi}^0} = 400$ GeV)	2015 search data
total	5317	4449	447891
trigger	3703	2796	425164
BX veto	3703	2796	389321
Vertex veto	3703	2796	385915
Halo veto	3671	2617	213310
N_{DT} in barrel station 3 = 0	3605	2249	200956
N_{DT} in barrel station 4 < 2	3605	2243	198436
max($\Delta\phi$(DT Segment$_i$, DT Segment$_j$)) < $\pi/2$	3605	2237	197826
max($\Delta\phi$(DT Segment$_i$(no st 4), Leading jet)) < 1	3597	2192	144193
Number of close DT outer all pairs	3595	2163	143934
$\min(\Delta \mathrm{R}(DT_{st4}, RPC_{st1-3})) > 0.5$	3595	2162	143014
Number of Close Outer Barrel RPC Pairs < 1	3555	2128	142155
HCAL noise veto	3348	2002	53179
$E_{jet} > 70$ GeV	3086	1841	30598
$\eta_{jet} < 1.0$	2672	1569	2314
$\mathrm{n90}_{jet} > 3$	2446	1515	127
nTowiPhi < 5	2431	1505	21
$E_{iphi}/E_{jet} < 0.95$	2429	1505	9
$R_1 > 0.15$	2429	1505	8
$R_2 > 0.1$	2428	1505	6
$0.3 < R_{Peak} < 0.7$	2427	1504	4
Peak sample < 7	2427	1504	4
$R_{Outer} < 0.3$	2427	1504	4

Table 4.14: Cumulative number of events all selection criteria, for 2016 MC simulations of $m_{\tilde{g}} = 1200$ GeV and $m_{\tilde{\chi}^0} = 1044$ GeV, corresponding to $E_{gluon} = 145$ GeV, for $m_{\tilde{t}} = 600$ GeV and $m_{\tilde{\chi}^0} = 400$ GeV, corresponding to $E_t = 192$ GeV, for the 2016 search dataset.

$\mathrm{L} = 35.9\,\mathrm{fb}^{-1}$

	$\tilde{g} \to g\tilde{\chi}^0$ (2016 MC simulation) ($M_{\tilde{g}} = 1200$ GeV, $M_{\tilde{\chi}^0} = 1044$ GeV)	$\tilde{t} \to t\tilde{\chi}^0$ (2016 MC simulation) ($M_{\tilde{t}} = 600$ GeV, $M_{\tilde{\chi}^0} = 400$ GeV)	2016 search data
total	5317	4449	3838714
trigger	3969	2951	3217983
BX veto	3969	2951	3047840
Vertex veto	3969	2951	3037376
Halo veto	3937	2771	1456258
N_{DT} in barrel station 3 = 0	3867	2394	1410319
N_{DT} in barrel station 4 < 2	3867	2389	1328184
$\max(\Delta\phi(\text{DT Segment}_i, \text{DT Segment}_j)) < \pi/2$	3867	2382	1322269
$\max(\Delta\phi(\text{DT Segment}_i(\text{no st 4}), \text{Leading jet})) < 1$	3860	2341	823614
Number of close DT outer all pairs	3857	2313	821675
$\min(\Delta\mathrm{R}(DT_{st4}, RPC_{st1-3})) > 0.5$	3857	2310	786811
Number of Close Outer Barrel RPC Pairs < 1	3803	2266	763531
HCAL noise veto	3801	2265	279098
$\max(\mathrm{abs}(\Delta ieta(\text{hcalTower}_i, \text{hcalTower}_j))) < 11$	3778	2242	252694
$E_{jet} > 70$ GeV	3576	2113	96774
$\eta_{jet} < 1.0$	3132	1821	7676
$\mathrm{n}90_{jet} > 3$	2816	1746	632
nTowiPhi < 5	2798	1731	40
$E_{iphi}/E_{jet} < 0.95$	2797	1731	14
$R_1 > 0.15$	2797	1731	14
$R_2 > 0.1$	2786	1724	14
$0.3 < R_{Peak} < 0.7$	2784	1723	13
2< Peak sample < 6	2784	1723	13
$R_{Outer} < 0.3$	2784	1723	13

Table 4.15: Summary of background predictions for the 2015/2016 search.

Period	Livetime (hrs)	Noise	Cosmics	Halo	Total	Observed
2015 control	-	$0.3^{+2.4}_{-0.3}$	1.7 ± 0.6	0	-	2
2015	135	$0.4^{+2.9}_{-0.4}$	2.6 ± 0.9	1.1 ± 0.1	$4.1^{+3.0}_{-1.0}$	4
2016 control	-	$0^{+2.2}_{-0}$	2.5 ± 0.9	0	-	2
2016	586	$0^{+9.8}_{-0}$	8.8 ± 3.1	2.6 ± 0.2	$11.4^{+10.3}_{-3.1}$	13

on the time window considered, which is a fraction of the total trigger livetime. Since the number of events will change discretely as the lifetime increases, we add more lifetime hypotheses to reveal this timing structure. For each event observed, we pick two corresponding lifetime hypotheses: the largest lifetime when the search window excludes the event, and the smallest lifetime the search window includes the event.

In Chapter 4.6, we mentioned that the signal is very likely to decay when there are collisions and thus not visible to our trigger. We take this into account by calculating effective luminosities via the toy Monte Carlo simulation. More specifically, in each lifetime hypothesis, we generate a thousand signal events in each lumisection of the search period, decay them, and calculate their probabilities of decaying when our trigger is live. We then sum up the integrated luminosities in each lumisection but weighted by the probabilities we just calculated, getting the result of the effective integrated luminosities.

After that, we perform counting experiments in which we count how many events we observed in each lifetime hypothesis. We also calculate the expected background in each case assuming that the cosmic ray and HCAL noise rate are constant with time, and we sample the beam halo events in terms of number of BXs after the collision and use that as a template to calculate the halo background in each search window, in which only halo events in the included BXs are considered. Table 4.16 and Table 4.17 show the results of the counting experiment.

Table 4.16: Results of the 2015 counting experiments for selected lifetime hypotheses.Under different lifetime hypotheses, the observed number indicated the events included in the corresponding time window, while the background depends also on the window. The trigger livetime increases and then remains at its peak value as the size of time window increases with the lifetime. The effective luminosity increases at first, due to the increase of the time window, but then drops since decay might take too long so it happens after the last run of our search sample data-taking period. The information of lifetime hypotheses between $100\mu s$ and 10^3 are not listed since they are in the middle of the lifetime plateau.

Lifetime	$L_{eff}(fb^{-1})$	Livetime (s)	Expected bkg	Observed
50 ns	0.02	7.5×10^3	$0.08^{+0.05}_{-0.01}$	0
75 ns	0.04	1.5×10^4	$0.16^{+0.10}_{-0.03}$	0
100 ns	0.08	2.9×10^4	$0.31^{+0.19}_{-0.06}$	0
1 μs	0.64	1.8×10^5	$1.7^{+1.2}_{-0.4}$	2
10 μs	1.22	4.6×10^5	$4.0^{+2.9}_{-1.0}$	3
100 μs	1.29	4.8×10^5	$4.1^{+3.0}_{-1.0}$	4
10^3 s	1.27	4.8×10^5	$4.1^{+3.0}_{-1.0}$	4
10^4 s	0.97	4.8×10^5	$4.1^{+3.0}_{-1.0}$	4
10^5 s	0.51	4.8×10^5	$4.1^{+3.0}_{-1.0}$	4
10^6 s	0.28	4.8×10^5	$4.1^{+3.0}_{-1.0}$	4

4.9.2 Limits on Gluino and Stop Production

In both the 2015 and 2016 searches, we did not observe an excess of observed events with respect to the backgrounds. In setting the 95% CL limit, instead of stacking the 2015 and 2016 data together, we treat them as separate channels and combine the likelihood together.

Table 4.17: Results of the 2016 counting experiments for selected lifetime hypotheses.Under different lifetime hypotheses, the observed number indicated the events included in the corresponding time window, while the background depends also on the time window. The trigger livetime increases and then remains at its peak value as the size of time window increases with the lifetime. The effective luminosity increases at first, due to the increase of the time window, but then drops since decay might take too long so it happens after the last run of our search sample data-taking period. The information of lifetime hypotheses between 100 μs and 10^3 s are not listed since they are in the middle of the lifetime plateau.

Lifetime	$L_{eff}(fb^{-1})$	Livetime (s)	Expected bkg	Observed
50 ns	0.27	6.2×10^4	$0.4^{+0.3}_{-0.1}$	0
75 ns	0.65	12.3×10^4	$0.8^{+0.6}_{-0.2}$	0
100 ns	1.27	2.4×10^5	$1.4^{+1.2}_{-0.4}$	0
1 μs	9.98	1.5×10^6	$8.4^{+7.5}_{-2.3}$	8
10 μs	13.37	2.1×10^6	$11.3^{+10.2}_{-3.1}$	13
100 μs	13.70	2.1×10^6	$11.4^{+10.3}_{-3.1}$	13
10^3 s	13.57	2.1×10^6	$11.4^{+10.3}_{-3.1}$	13
10^4 s	11.78	2.1×10^6	$11.4^{+10.3}_{-3.1}$	13
10^5 s	8.27	2.1×10^6	$11.4^{+10.3}_{-3.1}$	13
10^6 s	5.61	2.1×10^6	$11.4^{+10.3}_{-3.1}$	13

We calculate the limits on the signal production cross section by using a hybird CLs method. These limits are shown in Fig. 4.24, assuming $E_{\tilde{g}} > 130$ GeV ($m_{\tilde{g}} - m_{\tilde{\chi}^0} \gtrapprox 160$ GeV or $E_t > 170$ GeV).

In Fig. 4.25, limits on the $\sigma \times B$ are converted to mass limits, assuming the decay branching fraction to be 100%. Also assuming $E_{\tilde{g}} > 130$ GeV ($m_{\tilde{g}} - m_{\tilde{\chi}^0} \gtrapprox 160$ GeV or $E_t > 170$ GeV and an interaction of "cloud" model, we are able to exclude gluinos with mass less 1385 GeV (1393 GeV) that decay though $\tilde{g} \to g\tilde{\chi}^0$ ($\tilde{g} \to q\bar{q}\tilde{\chi}^0$), and top squarks with mass less than 744 GeV at 95% CL for lifetimes 10 $\mu s < \tau < 1000$ s.

Figure 4.26 shows the gluino-neutralino mass region we are able to exclude in this search.

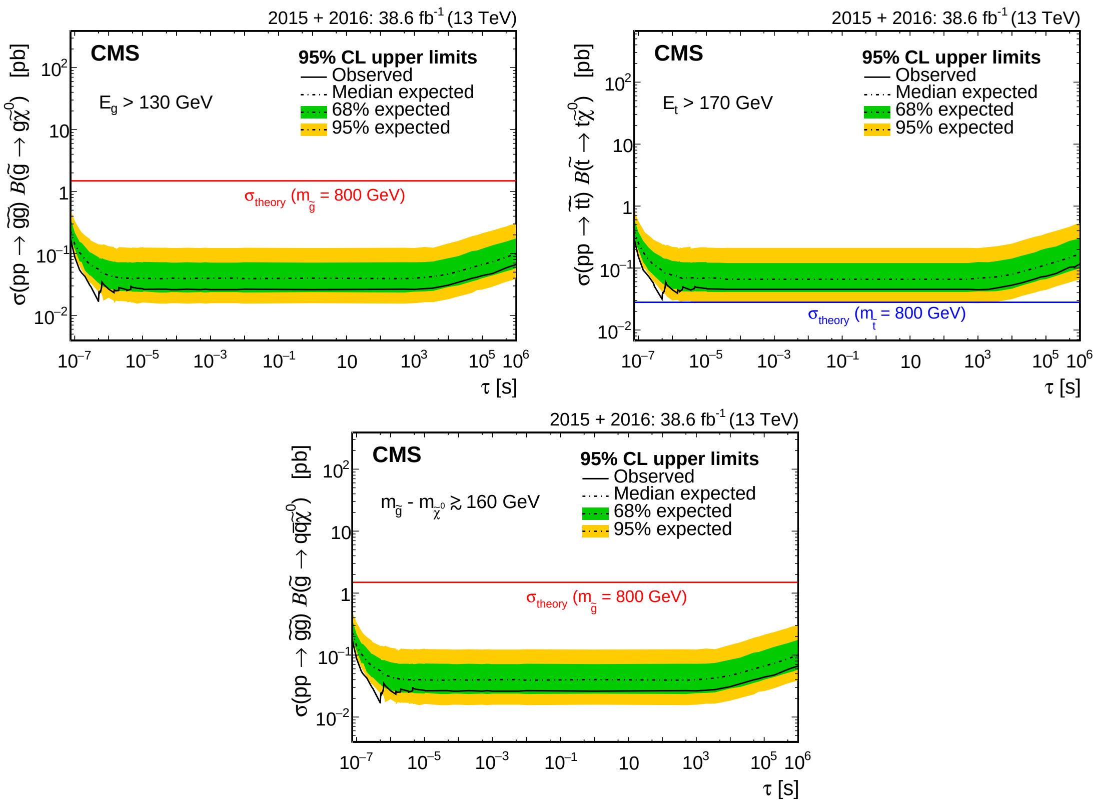

Figure 4.24: The 95% CL upper limits on $B\sigma$ for gluino and top squark pair production as a function of lifetime, assuming the cloud model of R-hadron interactions, for combined 2015 and 2016 data for the calorimeter search. We show gluinos that undergo a two-body decay (upper left), top squarks that undergo a two-body decay (upper right), and gluinos that undergo a three-body decay (lower). The discontinuous structure observed between 10^{-7} and 10^{-5} s is due to the increase in the number of observed events in the search window as the lifetime increases. The theory lines assume $B = 100\%$.

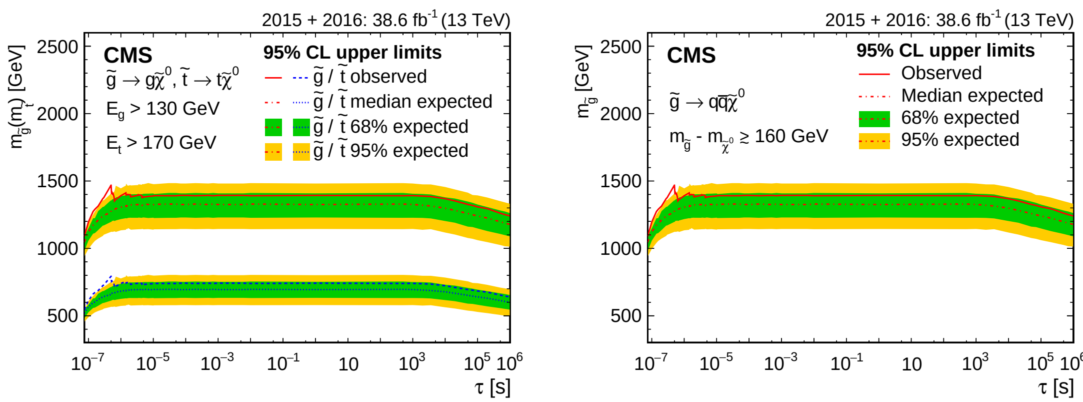

Figure 4.25: The 95% CL upper limits on the gluino and top squark mass, as a function of lifetime, assuming the cloud model of R-hadron interactions, for combined 2015 and 2016 data for the calorimeter search. We show gluinos and top squarks that undergo a two-body decay (left) and gluinos that undergo a three-body decay (right). The discontinuous structure observed between 10^{-7} and 10^{-5} s is due to the increase in the number of observed events in the search window as the lifetime increases.

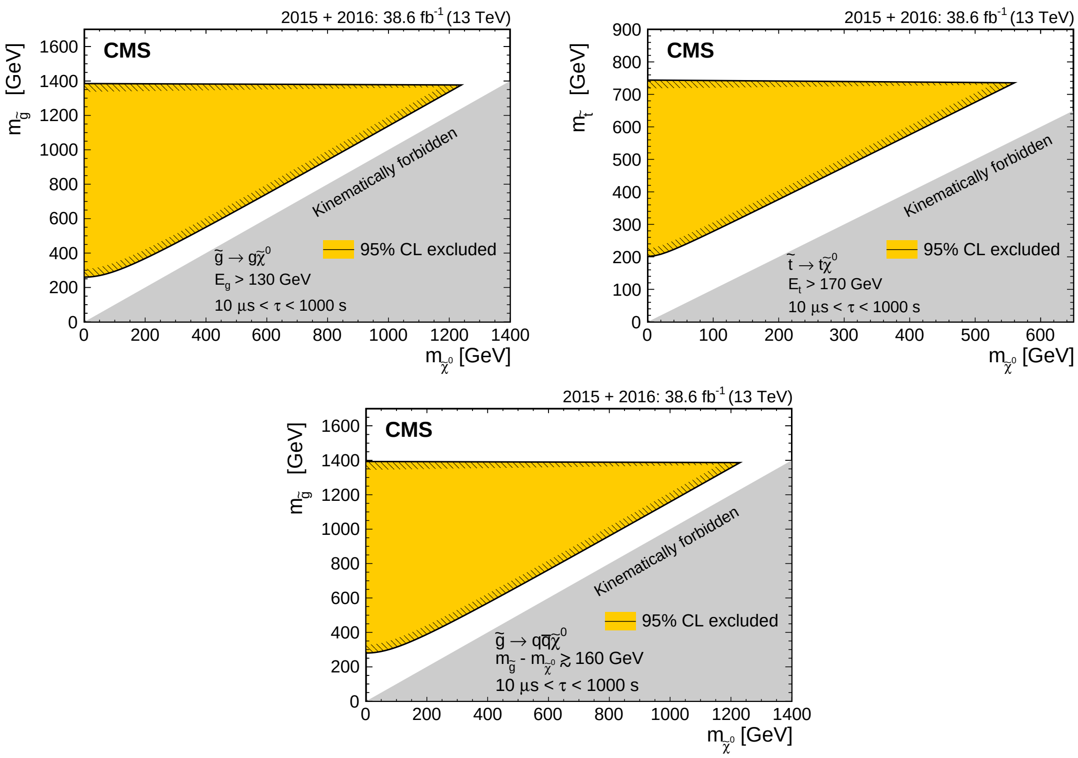

Figure 4.26: The 95% CL upper limits in the gluino (top squark) mass vs. neutralino mass plane, for lifetimes between $10\mu s$ and 1000 s, for combined 2015 and 2016 data for the calorimeter search. The excluded region is indicated by the yellow shaded area. We show gluinos that undergo a two-body decay (upper left), top squarks that undergo a two-body decay (upper right), and gluinos that undergo a three-body decay (lower).

Chapter 5: Search for Stopped Particles Decaying to Muons

The iron yokes interleaving the DT stations are other places where massive long-lived particles are very likely to come to rest, due to the density of their material. However, in case of hadronic decays, which we explored in Chapter 4, these hadrons are unable to penetrate multiple layers of iron yoke to leave a track in the muon chamber. Thus we do not have an adequate object that we can trigger on.

To fully exploit the decay signature of stopped massive long-lived particles, in this chapter, we are looking for a stopped signal decaying leptonically to a pair of muons out-of-time with respect to any collisions. Since the muons are not strongly interacting, they can be observed as long as the BSM particle decay is in the CMS detector. The observation of such a signal would imply the existence of MCHAMPs in some BSM theories, or the existence of second LSP decaying to a pair of muons and the LSP [20].

5.1 Trigger and Datasets

Similar to the trigger used in the calorimeter search described in Chapter 4, in this search, events are required to be away from any collisions by at least 2BXs. Besides that, the event should have at least one reconstructed muon with transverse momentum greater than 40 GeV.

The search is performed on the data collected via the dedicated trigger by the CMS detector during the 2015 and 2016 collisions data taking periods, which corresponds to 2.8 fb^{-1} and 36.2 fb^{-1} of 13 TeV data. The trigger livetimes are 155 hours in 2015 and 589 hours in 2016.

5.2 Monte Carlo Simulation

Two benchmark models are considered in this search: a gluino three-body decay process via NLSP, and exotic multiply charged massive particles (MCHAMPs) with charge $|Q| = 2e$ decaying to a pair of muons. In the case of the gluino decay, the mass of the NLSP neutralino is set to be 2.5 times the LSP neutralino mass.

The signal generation process is almost the same as described in Section 4.4, yet in the stage2 we simulate the decay of particles that are not only in the barrel calorimeter but in the whole CMS detector.

5.3 Event Selection

We select events that pass our high level trigger and, similar to the calorimeter search, have no reconstructed collision vertices.

Traditional algorithms reconstruct standalone muon tracks using only hits in the muon system but requiring the tracks originate from the IP. The reconstruction efficiency of these algorithms will drop significantly as the tracks are more displaced. A new algorithm is implemented to deal with this by removing the IP constraint thus giving a new track collection called displaced standalone (DSA) muon tracks, which is the type of track we use in this search.

To reduce the impact of cosmic muon showers, the events are required to have exactly one good DSA track in the upper hemisphere and exactly one DSA track in the lower hemisphere. A good DSA track is a muon track with p_T greater than 50 GeV that 1) has at least three DT chambers with valid hits, 2) has at least three valid RPC hits and 3) has no CSC hits so that beam halo background events are rejected.

The background from cosmic ray muons is now the only non-negligible background we need to worry about. Although both signal events and cosmic ray muons can leave exactly one DSA track in the upper hemisphere and exactly one track in the lower hemisphere, the upper track is outgoing in the case of the signal decay and incoming otherwise. Timing information in the muon system can help us to decide the moving direction of the muons.

To ensure the good timing quality of the measurement, we require that the muon track has at least eight independent time measurements for the calculation of the TOF. Also, the DSA track should have less than 5.0 ns in the uncertainty of the time measured at the IP.

Typically one would assume that the cosmic ray muon will first reach the upper hemisphere and then the lower hemisphere. While this could happen in case of the signal as well, it's more likely that in that case, the two muons reach the muon chambers at a similar time. We therefore define the discriminating variable $\mathrm{t_{DT}}$, which is the timing measurement of the DT in the track that is closest to the IP. We expect $\mathrm{t_{DT}}$ (upper) $-$ $\mathrm{t_{DT}}$ (lower) around 40 ns for the cosmic ray backgrounds and approximately 0 for the signal decays. Events are thus required to have $\Delta\mathrm{t_{DT}}$, which is defined as $\mathrm{t_{DT}}$ (upper) $-$ $\mathrm{t_{DT}}$ (lower), greater than -20 ns so that cosmic ray muon events are mostly rejected. We also fit the timing measurement in each DT layer in the lower hemisphere to get the moving direction, which is required to be pointing downward.

Similarly, we can use timing information of the RPCs in the muon chambers. The RPC hits are given BX assignments, which are usually 0 for the muons coming from prompt decays of collision products, as well as the outgoing muons in our signal events. However, for the cosmic muons, the RPC hits of the outgoing muons are assigned BX numbers as large as 2. We then calculated the average BX assignment in a track and then multiply it by 25 ns, and define this value as t_{RPC}. Thus a typical signal will have a t_{RPC} of 0 ns in both muon tracks but typical cosmic muons will have an upper track with a t_{RPC} of 0 ns and a lower track with t_{RPC} around 50 ns. We define the discriminating variable $\Delta t_{RPC} = t_{RPC}$ (upper) $- t_{RPC}$ (lower), and require the events to have $\Delta t_{RPC} > 7.5$ ns to select signal events.

Figure 5.1 shows the distribution of some representative discriminating variables for simulations and data.

5.4 Signal Efficiency

Table 5.1 and Table 5.2 show the $\varepsilon_{\text{stopping}}$ and $\varepsilon_{\text{reco}}$ in the muon search, and the $\varepsilon_{\text{signal}}$ is the product of these two efficiencies. Unlike the calorimeter based search, $\varepsilon_{\text{stopping}}$ in this search is defined as the probability of LLPs to come to stop in the detector, not just in the barrel calorimeter. The $\varepsilon_{\text{reco}}$ is defined in the same way as described in Section 4.6. The $\varepsilon_{\text{stopping}}$ for MCHAMPs is overall larger than that of gluinos because MCHAMPs are all doubly charged yet only a portion of gluinos are.

The signal efficiency is negatively impacted by the level 1 muon trigger, which is designed to tag the muons from the collision point, and thus have limited efficiency to

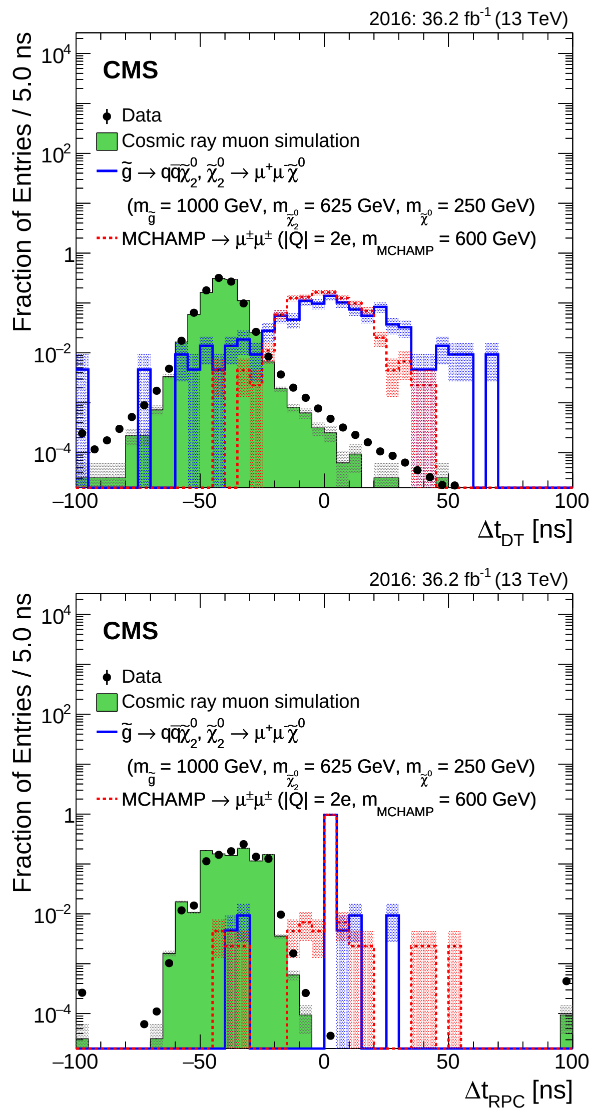

Figure 5.1: The Δt_{DT} (left) and Δt_{RPC} (right) distributions for 2016 data, MC simulated cosmic ray muon, 1000 GeV gluino signal, and 600 GeV MCHAMP signal events, for the muon search. The events plotted pass a subset of the full analysis selection that is designed to select good-quality DSA muon tracks but does not reject the cosmic ray muon background. The number of cosmic ray muon background events is greatly reduced when the full selection is applied, as we require $\Delta t_{\mathrm{DT}} > -20$ ns and $\Delta t_{\mathrm{RPC}} > -7.5$ ns. The gray bands indicate the statistical uncertainty in the simulation. The histograms are normalized to unit area.

accept the displaced muons. Moreover, as we require that the event has exactly one upper hemisphere muon track and exactly one lower hemisphere muon track, $\varepsilon_{\text{signal}}$ decreases accordingly. The gluino signal is affected more since the muon pairs from the gluino decay, unlike from the MCHAMP decay, is not back-to-back.

Table 5.1: Gluino $\varepsilon_{\text{stopping}}$ and $\varepsilon_{\text{reco}}$, as well as the number of expected gluino events with lifetimes between 10 μs and 1000 s, assuming $B(\tilde{g} \to q\bar{q}\tilde{\chi}_2^0)B(\tilde{\chi}_2^0 \to \mu^+\mu^-\tilde{\chi}^0) = 100\%$, for each mass point considered for the 2016 muon search. The efficiencies are constant for this range of lifetimes.

$m_{\tilde{g}}$ [GeV]	$\varepsilon_{\text{stopping}}$	$\varepsilon_{\text{reco}}$	Expected events
400	0.19	0.0015	400
600	0.17	0.0024	50
800	0.17	0.0037	10
1000	0.17	0.0029	2
1200	0.18	0.0025	0.5
1400	0.20	0.0031	0.2
1600	0.21	0.0029	0.1

Table 5.2: MCHAMP $\varepsilon_{\text{stopping}}$ and $\varepsilon_{\text{reco}}$, as well as the number of expected MCHAMP events with lifetimes between 10 μs and 1000 s, assuming $B(\text{MCHAMP} \to \mu^{\pm}\mu^{\pm}) = 100\%$, for each mass point considered for the 2016 muon search. The efficiencies are constant for this range of lifetimes.

m_{MCHAMP} [GeV]	$\varepsilon_{\text{stopping}}$	$\varepsilon_{\text{reco}}$	Expected events
100	0.33	0.0059	100
200	0.29	0.041	50
400	0.28	0.045	4
600	0.25	0.042	0.5
800	0.30	0.038	0.1

5.5 Backgrounds

To estimate the only remaining background, which is the cosmic ray muon background, we use a data-driven method to extrapolate the cosmic ray background estimate from the control region where the cosmic ray muons dominate to the signal region. We apply first all the preselection criteria, which is all the selection criteria except the two on Δt_{DT} and Δt_{RPC}. We then apply an inverted Δt_{RPC} on the events. We then fit the distribution of those remaining events that have Δt_{DT} less than -20 ns, using the sum of two Gaussian distributions and a Crystal Ball function. We then integrate this fitted distribution over the signal region, which is $\Delta t_{\mathrm{DT}} > -20$ ns, giving the estimate in different Δt_{RPC} cut region. We have done this in several different Δt_{RPC} selection regions, which are $-50 < \Delta t_{\mathrm{RPC}} < -7.5$ ns, $-45 < \Delta t_{\mathrm{RPC}} < -7.5$ ns until $-10 < \Delta t_{\mathrm{RPC}} < -7.5$ ns, in steps of 5 ns. We then plot these integrals as a function of the lower Δt_{RPC} threshold, which we then fit using an error function, as shown in Fig. 5.2. We then integrate the distribution over the region $\Delta t_{\mathrm{RPC}} > -7.5$ ns, giving the final central estimate.

We repeat the same steps as above, but using two Gaussian distributions and a Landau function to fit the Δt_{DT} distribution. The systematic uncertainty is defined as the difference in the central estimates given by these two cases. The background is 0.04 ± 0.03 (syst.) in 2015 and 0.50 ± 0.02 (stat.) ± 0.40 (syst.) in 2016.

5.6 Systematic Uncertainties

There are several sources of systematic uncertainties in the signal yield, and the results are shown in Table 5.3.

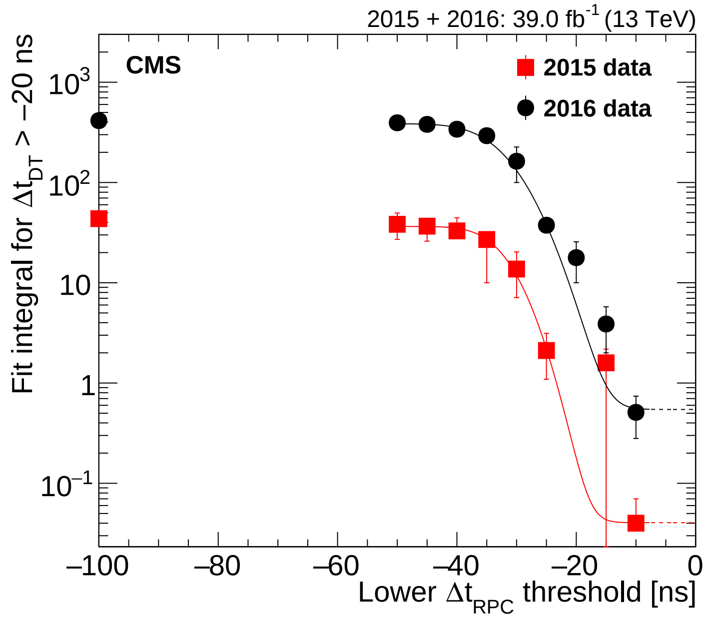

Figure 5.2: The background extrapolation for the muon search. The integral of the fit function to Δt_{DT} with the sum of two Gaussian distributions and a Crystal Ball function, for $\Delta t_{\mathrm{DT}} > -20$ ns, is plotted as a function of the lower Δt_{RPC} selection, for 2015 (red squares) and 2016 (black circles) data. The points are fitted with an error function and used to extrapolate to the signal region, which is defined as $\Delta t_{\mathrm{RPC}} > -7.5$ ns.

Table 5.3: Systematic uncertainties in the signal efficiency for the 2015 and 2016 muon searches.

Systematic uncertainty	2015	2016
Q/p_T resolution mismodeling	13%	7.0%
Trigger acceptance	13%	2.8%
Integrated luminosity	2.3%	2.5%

There is an uncertainty in the p_T measurement , given by the discrepancy between data and MC simulation. To quantify this discrepancy, we compare the resolution of the charge divided by the p_T in both cases, which is defined as:

$$R(Q/p_T) = \frac{(Q/p_T)^{\text{upper}} - (Q/p_T)^{\text{lower}}}{\sqrt{2}(Q/p_Tt)^{\text{lower}}}. \tag{5.1}$$

The resolution is calculated by taking the standard deviation of the Gaussian fitting in Eq 5.1. This resolution as a function of p_T of the muon track in the lower hemisphere is estimated to be 9.0 (5.3)% between the 2015 (2016) analysis for muon tracks with $p_T > 50$ GeV. We can propagate this uncertainty to the uncertainty in the signal efficiency by smearing the momenta of muon tracks and counting the relative variation in the signal yield, which is 13 (7.0)% in the 2015 (2016) analysis.

The uncertainty associated with the trigger acceptance is estimated by comparing the trigger turn-on between data and simulation. The largest difference between data and simulation is 13 (2.8)% in the 2015 (2016) analysis.

The total systematic uncertainty in the signal efficiency is 19 (7.9)% in the 2015 (2016) search.

5.7 Results

As described in Chapter 4.9, we performed a Toy Monte Carlo simulation, followed by a counting experiment to calculate the number of events observed and the background in each lifetime hypotheses. The result is shown in Table 5.4.

For the muon search, Fig. 5.3 shows the 95% CL upper limits on $B\sigma$ as a function of lifetime for 1000 GeV gluinos and 400 GeV MCHAMPs. Fig. 5.4 shows the 95% CL upper limits on the gluino and MCHAMPs of different masses. Assuming $B(\tilde{g} \to q\bar{q}\tilde{\chi}_2^0)B(\tilde{\chi}_2^0 \to \mu^+\mu^-\tilde{\chi}^0) = 100\%$, $m_{\tilde{\chi}^0} = 0.25m_{\tilde{g}}$ and $m_{\tilde{\chi}_2^0} = 2.5m_{\tilde{\chi}^0}$, gluinos with

Table 5.4: Counting experiment results for different lifetimes in the muon search with 2016 data.

Lifetime [s]	Effective integrated luminosity [fb^{-1}]	Trigger livetime [hrs]	Expected background	Observed events
10^{-7}	1.27	68	0.06 ± 0.05	0
10^{-6}	9.95	422	0.36 ± 0.29	0
10^{-5}	13.34	581	0.49 ± 0.39	0
10^{-4}	13.67	589	0.50 ± 0.40	0
1	13.67	589	0.50 ± 0.40	0
10^{3}	13.55	589	0.50 ± 0.40	0
10^{4}	11.75	589	0.50 ± 0.40	0
10^{5}	8.26	589	0.50 ± 0.40	0
10^{6}	5.61	589	0.50 ± 0.40	0

masses between 400 GeV and 980 GeV are excluded for lifetimes between 10 μs and 1000 s. Assuming $B(\text{MCHAMP} \rightarrow \mu^{\pm}\mu^{\pm}) = 100\%$, MCHAMPs with masses between 100 GeV and 440 GeV and $|Q| = 2e$ are excluded for lifetimes between $10\mu s$ and $1000\mu s$.

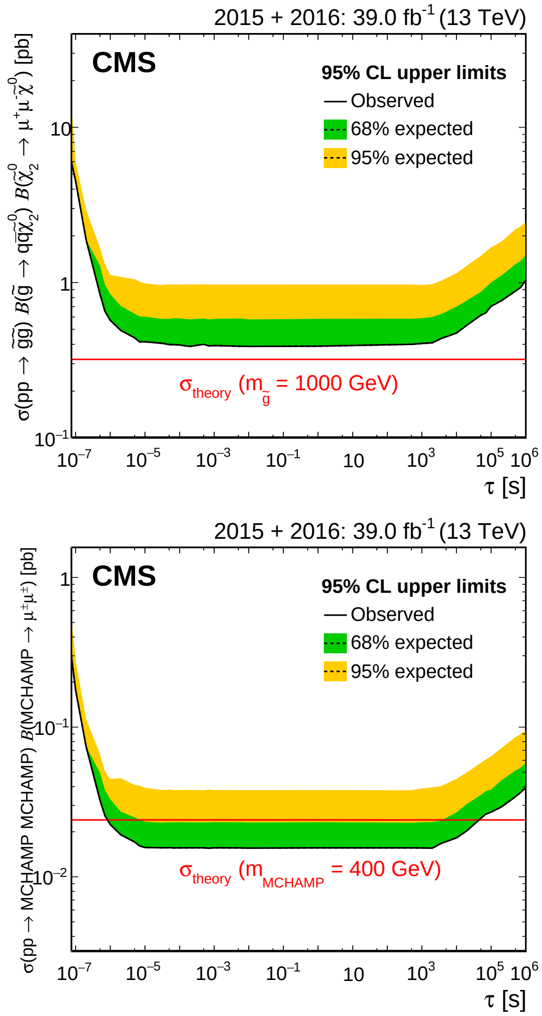

Figure 5.3: The 95% CL upper limits on $B\sigma$ for 1000 GeV gluino (left) and 400 GeV MCHAMP (right) pair production as a function of lifetime, for combined 2015 and 2016 data for the muon search. The theory lines assume $B = 100\%$.

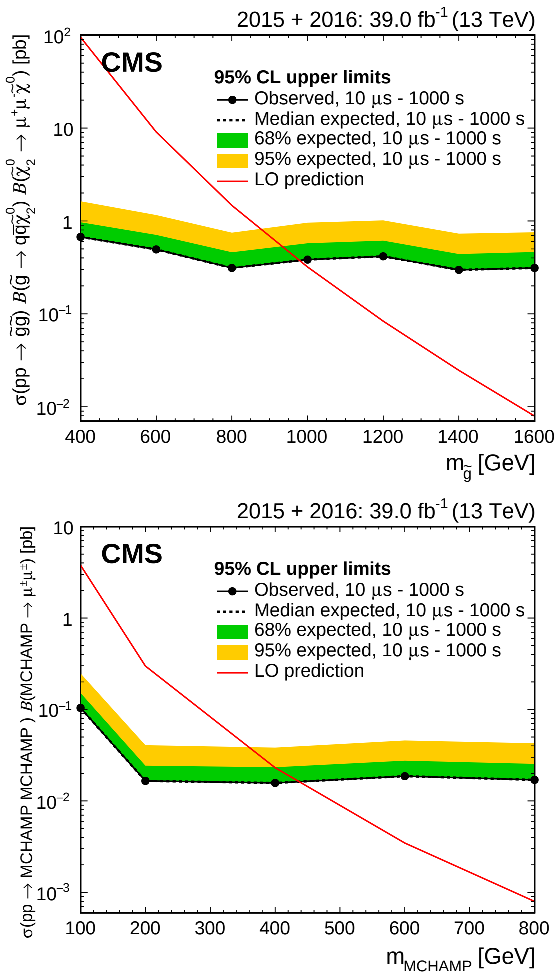

Figure 5.4: 95% CL upper limits on $B\sigma$ for gluino (left) and MCHAMP (right) pair production as a function of mass, for lifetimes between 10 μs and 1000 s, for combined 2015 and 2016 data for the muon search. The theory curves assume $B = 100\%$.

Chapter 6: Conclusion

6.1 Analysis Conclusions

Two searches are performed to look for particles whose lifetime are long enough to come to rest in the detector and decay afterwards. Our trigger only accepts events that are at least 2 BXs away from any collisions, since the decays of the stopped exotic LLPs are most likely to be observed when there are no collisions.

The calorimeter based search looks for hadronic or semi-leptonic decays in the barrel calorimeter, which results in high energy reconstructed barrel jets. No excess is observed in either 2015 or 2016 data. Assuming the corresponding decaying branching fraction to be 100%, $E_{\tilde{g}} > 130$ GeV ($m_{\tilde{g}} - m_{\tilde{\chi}^0} \gtrapprox 160$ GeV) or $E_t > 170$ GeV and an R-hadron interaction "cloud" model, we are able to exclude gluinos with mass less 1385 GeV(1393 GeV) that decay though $\tilde{g} \to g\tilde{\chi}^0(\tilde{g} \to q\bar{q}\tilde{\chi}^0)$, and top squarks with mass less than 744 GeV at 95% CL for lifetimes $10\mu s < \tau < 1000s$.

The muon search, on the other hand , targets LLPs that decay leptonically or semi-leptonically to a pair of muons, which are reconstructed as displaced muon tracks. No excess is observed in either 2015 or 2016 data. Assuming $B(\tilde{g} \to q\bar{q}\tilde{\chi}_2^0)B(\tilde{\chi}_2^0 \to \mu^+\mu^-\tilde{\chi}^0) = 100\%$, $m_{\tilde{\chi}^0} = 0.25m_{\tilde{g}}$ and $m_{\tilde{\chi}_2^0} = 2.5m_{\tilde{\chi}^0}$, gluinos with masses between 400 GeV and 980 GeV are excluded for lifetimes between $10\mu s$ and $1000s$. Assuming

$B(\text{MCHAMP} \rightarrow \mu^{\pm}\mu^{\pm}) = 100\%$, MCHAMPs with masses between 100 GeV and 440 GeV and $|Q| = 2e$ are excluded for lifetimes between 10 μs and 1000 μs.

These limits are the most stringent limits on the stopped LLPs so far, and the muon search is the first one that targets stopped particles decaying to a pair of muons.

6.2 Future Plan

The above limits conclude the stopped particles searches we've performed in 2015 and 2016. The limits are higher compared to that of the 8 TeV search, as a result of the increase of center-of-mass energy and the higher integrated luminosity of the data taken by CMS. We also get a more precise measurement by considering the impact of slow neutrons on the signal efficiency.

Now in 2017, we decided not to repeat the same searches with 2017 data, based mainly on the consideration of the bigger picture as well as the manpower in our research group. The two searches are mostly motivated by split-SUSY, which predicts a long-lived gluino at the TeV scale. Since our searches only analyze events that are at least 2 BXs away from any collision, they are more sensitive to particles with lifetime greater than $\sim$ 100 ns. Meanwhile the measurement of the mass of the Higgs boson suggests that the lifetime of the gluino in split-SUSY is most likely to be less than several nanoseconds [64], since the Higgs mass suggests that the upper bound of the split-SUSY scale is less than 10^8 GeV, which is not large enough to produce a quasi-stable gluino. As a result, people are interested in searches that are sensitive to gluinos with shorter lifetimes, such as displaced jets searches.

The disfavoring of a gluino with lifetime less than nanoseconds in the split-SUSY does not mean that quasi-stable BSM particles do not exist. If they exist, they can still be observed by the HSCP search, which is sensitive to particles with lifetimes from nanoseconds up to infinity.

There are many interesting searches ongoing in our research group. And since I'm graduating and the stopped particles search is not among the top priorities based on the consideration of bigger picture, there is not enough manpower that can take care of the stopped particle searches. However, we are continuing to maintain the triggers of the searches and storing the 2017 NoBPTX data. If in the future there is some evidence of quasi-stable charged particles in the HSCP searches or someone becomes interested in our searches, people can always retrieve the most recent NoBPTX data and perform the stopped particle analyses again on these data.

Bibliography

[1] Serguei Chatrchyan et al. Observation of a new boson at a mass of 125 GeV with the CMS experiment at the LHC. *Phys. Lett.*, B716:30–61, 2012.

[2] Georges Aad et al. Observation of a new particle in the search for the Standard Model Higgs boson with the ATLAS detector at the LHC. *Phys. Lett.*, B716:1–29, 2012.

[3] Stephen P. Martin. A Supersymmetry primer. 1997. [Adv. Ser. Direct. High Energy Phys.18,1(1998)].

[4] James D. Wells. Implications of supersymmetry breaking with a little hierarchy between gauginos and scalars. In *11th International Conference on Supersymmetry and the Unification of Fundamental Interactions (SUSY 2003) Tucson, Arizona, June 5-10, 2003*, 2003.

[5] Nima Arkani-Hamed and Savas Dimopoulos. Supersymmetric unification without low energy supersymmetry and signatures for fine-tuning at the LHC. *JHEP*, 06:073, 2005.

[6] G. F. Giudice and A. Romanino. Split supersymmetry. *Nucl. Phys.*, B699:65–89, 2004. [Erratum: Nucl. Phys.B706,487(2005)].

[7] S. L. Glashow. Partial Symmetries of Weak Interactions. *Nucl. Phys.*, 22:579–588, 1961.

[8] G. Arnison et al. Experimental Observation of Isolated Large Transverse Energy Electrons with Associated Missing Energy at s**(1/2) = 540-GeV. *Phys. Lett.*, 122B:103–116, 1983. [,611(1983)].

[9] M. Banner et al. Observation of Single Isolated Electrons of High Transverse Momentum in Events with Missing Transverse Energy at the CERN anti-p p Collider. *Phys. Lett.*, 122B:476–485, 1983.

[10] F. Englert and R. Brout. Broken Symmetry and the Mass of Gauge Vector Mesons. *Phys. Rev. Lett.*, 13:321–323, 1964.

[11] Peter W. Higgs. Broken Symmetries and the Masses of Gauge Bosons. *Phys. Rev. Lett.*, 13:508–509, 1964.

[12] G. S. Guralnik, C. R. Hagen, and T. W. B. Kibble. Global Conservation Laws and Massless Particles. *Phys. Rev. Lett.*, 13:585–587, 1964.

[13] Nima Arkani-Hamed, Savas Dimopoulos, and G. R. Dvali. The Hierarchy problem and new dimensions at a millimeter. *Phys. Lett.*, B429:263–272, 1998.

[14] Nima Arkani-Hamed, Savas Dimopoulos, and G. R. Dvali. Phenomenology, astrophysics and cosmology of theories with submillimeter dimensions and TeV scale quantum gravity. *Phys. Rev.*, D59:086004, 1999.

[15] Pierre Fayet. Spontaneously Broken Supersymmetric Theories of Weak, Electromagnetic and Strong Interactions. *Phys. Lett.*, 69B:489, 1977.

[16] Savas Dimopoulos and Howard Georgi. Softly Broken Supersymmetry and SU(5). *Nucl. Phys.*, B193:150–162, 1981.

[17] Asimina Arvanitaki, Chad Davis, Peter W. Graham, Aaron Pierce, and Jay G. Wacker. Limits on split supersymmetry from gluino cosmology. *Phys. Rev.*, D72:075011, 2005.

[18] Georges Aad et al. Search for metastable heavy charged particles with large ionisation energy loss in pp collisions at $\sqrt{s} = 8$ TeV using the ATLAS experiment. *Eur. Phys. J.*, C75(9):407, 2015.

[19] Vardan Khachatryan et al. Search for long-lived charged particles in proton-proton collisions at $\sqrt{s} = 13$TeV. *Phys. Rev.*, D94(11):112004, 2016.

[20] A. Arvanitaki, S. Dimopoulos, A. Pierce, S. Rajendran, and Jay G. Wacker. Stopping gluinos. *Phys. Rev.*, D76:055007, 2007.

[21] Savas Dimopoulos, Michael Dine, Stuart Raby, and Scott D. Thomas. Experimental signatures of low-energy gauge mediated supersymmetry breaking. *Phys. Rev. Lett.*, 76:3494–3497, 1996.

[22] R Bailey and Paul Collier. Standard Filling Schemes for Various LHC Operation Modes. Technical Report LHC-PROJECT-NOTE-323, CERN, Geneva, Sep 2003.

[23] S. Chatrchyan et al. The CMS Experiment at the CERN LHC. *JINST*, 3:S08004, 2008.

[24] M. Lipinski. The Phase-1 upgrade of the CMS pixel detector. *JINST*, 12(07):C07009, 2017.

[25] S Chatrchyan et al. Identification and Filtering of Uncharacteristic Noise in the CMS Hadron Calorimeter. *JINST*, 5:T03014, 2010.

[26] Howard Baer, King-man Cheung, and John F. Gunion. A Heavy gluino as the lightest supersymmetric particle. *Phys. Rev.*, D59:075002, 1999.

[27] Toshifumi Jittoh, Joe Sato, Takashi Shimomura, and Masato Yamanaka. Long life stau in the minimal supersymmetric standard model. *Phys. Rev.*, D73:055009, 2006. [Erratum: Phys. Rev.D87,no.1,019901(2013)].

[28] M. Fairbairn, A. C. Kraan, D. A. Milstead, T. Sjostrand, Peter Z. Skands, and T. Sloan. Stable massive particles at colliders. *Phys. Rept.*, 438:1–63, 2007.

[29] Matthew J. Strassler and Kathryn M. Zurek. Echoes of a hidden valley at hadron colliders. *Phys. Lett.*, B651:374–379, 2007.

[30] Asimina Arvanitaki, Savas Dimopoulos, Sergei Dubovsky, Peter W. Graham, Roni Harnik, and Surjeet Rajendran. Astrophysical Probes of Unification. *Phys. Rev.*, D79:105022, 2009.

[31] Asimina Arvanitaki, Nathaniel Craig, Savas Dimopoulos, and Giovanni Villadoro. Mini-Split. *JHEP*, 02:126, 2013.

[32] Inclusive search for new particles decaying to displaced jets at $\sqrt{s} = 13$ TeV. Technical Report CMS-PAS-EXO-16-003, CERN, Geneva, 2017.

[33] Edward Moyse. Searches for displaced hadronic and lepton jets at ATLAS. *PoS*, ICHEP2016:165, 2016.

[34] Vardan Khachatryan et al. Search for Displaced Supersymmetry in events with an electron and a muon with large impact parameters. *Phys. Rev. Lett.*, 114(6):061801, 2015.

[35] Search for displaced leptons in the e-mu channel. Technical Report CMS-PAS-EXO-16-022, CERN, Geneva, 2016.

[36] Vardan Khachatryan et al. Search for R-parity violating supersymmetry with displaced vertices in proton-proton collisions at $\sqrt{s} = 8$ TeV. *Phys. Rev.*, D95(1):012009, 2017.

[37] Georges Aad et al. Search for massive, long-lived particles using multitrack displaced vertices or displaced lepton pairs in pp collisions at $\sqrt{s} = 8$ TeV with the ATLAS detector. *Phys. Rev.*, D92(7):072004, 2015.

[38] Morad Aaboud et al. Search for long-lived, massive particles in events with displaced vertices and missing transverse momentum in $\sqrt{s} = 13$ TeV pp collisions with the ATLAS detector. 2017.

[39] V. Khachatryan et al. Search for disappearing tracks in proton-proton collisions at $\sqrt{s} = 8$ TeV. *JHEP*, 01:096, 2015.

[40] Morad Aaboud et al. Search for long-lived charginos based on a disappearing-track signature in pp collisions at $\sqrt{s} = 13$ TeV with the ATLAS detector. 2017.

[41] G. Abbiendi et al. Searches for gauge-mediated supersymmetry breaking topologies in e+ e- collisions at LEP2. *Eur. Phys. J.*, C46:307–341, 2006.

[42] V. M. Abazov et al. Search for stopped gluinos from $p\bar{p}$ collisions at $\sqrt{s} =$ 1.96-TeV. *Phys. Rev. Lett.*, 99:131801, 2007.

[43] Vardan Khachatryan et al. Search for Stopped Gluinos in pp collisions at $\sqrt{s} = 7$ TeV. *Phys. Rev. Lett.*, 106:011801, 2011.

[44] Serguei Chatrchyan et al. Search for stopped long-lived particles produced in pp collisions at $\sqrt{s} = 7$ TeV. *JHEP*, 08:026, 2012.

[45] Vardan Khachatryan et al. Search for Decays of Stopped Long-Lived Particles Produced in ProtonProton Collisions at $\sqrt{s} = 8$ TeV. *Eur. Phys. J.*, C75(4):151, 2015.

[46] Georges Aad et al. Search for decays of stopped, long-lived particles from 7 TeV pp collisions with the ATLAS detector. *Eur. Phys. J.*, C72:1965, 2012.

[47] Georges Aad et al. Search for long-lived stopped R-hadrons decaying out-of-time with pp collisions using the ATLAS detector. *Phys. Rev.*, D88(11):112003, 2013.

[48] P. Fayet. Massive gluinos. *Physics Letters B*, 78(4):417 – 420, 1978.

[49] Glennys R. Farrar and Pierre Fayet. Phenomenology of the production, decay, and detection of new hadronic states associated with supersymmetry. *Physics Letters B*, 76(5):575 – 579, 1978.

[50] Torbjorn Sjostrand, Stephen Mrenna, and Peter Z. Skands. A Brief Introduction to PYTHIA 8.1. *Comput. Phys. Commun.*, 178:852–867, 2008.

[51] S. Agostinelli et al. GEANT4: A Simulation toolkit. *Nucl. Instrum. Meth.*, A506:250–303, 2003.

[52] John Allison et al. Geant4 developments and applications. *IEEE Trans. Nucl. Sci.*, 53:270, 2006.

[53] Aafke Christine Kraan. Interactions of heavy stable hadronizing particles. *Eur. Phys. J.*, C37:91–104, 2004.

[54] Rasmus Mackeprang and Andrea Rizzi. Interactions of Coloured Heavy Stable Particles in Matter. *Eur. Phys. J.*, C50:353–362, 2007.

[55] Torbjorn Sjostrand, Stephen Mrenna, and Peter Z. Skands. PYTHIA 6.4 Physics and Manual. *JHEP*, 05:026, 2006.

[56] Matteo Cacciari, Gavin P. Salam, and Gregory Soyez. The Anti-k(t) jet clustering algorithm. *JHEP*, 04:063, 2008.

[57] Matteo Cacciari, Gavin P. Salam, and Gregory Soyez. FastJet User Manual. *Eur. Phys. J.*, C72:1896, 2012.

[58] P. Biallass and T. Hebbeker. Parametrization of the Cosmic Muon Flux for the Generator CMSCGEN. *ArXiv e-prints*, July 2009.

[59] D. Heck, G. Schatz, T. Thouw, J. Knapp, and J. N. Capdevielle. CORSIKA: A Monte Carlo code to simulate extensive air showers. 1998.

[60] CMS Collaboration. CMS luminosity measurement for the 2015 data taking period. CMS Physics Analysis Summary CMS-PAS-LUM-15-001, 2016.

[61] CMS Collaboration. CMS luminosity measurements for the 2016 data taking period. CMS Physics Analysis Summary CMS-PAS-LUM-17-001, 2017.

[62] S Chatrchyan et al. Performance of the CMS Hadron Calorimeter with Cosmic Ray Muons and LHC Beam Data. *JINST*, 5:T03012, 2010.

[63] Henning Kirschenmann. Jet performance in CMS. *PoS*, EPS-HEP2013:433, 2013.

[64] Gian F. Giudice and Alessandro Strumia. Probing High-Scale and Split Supersymmetry with Higgs Mass Measurements. *Nucl. Phys.*, B858:63–83, 2012.